University of Alberta

Ductile Fracture of Steel

by

Heng Aik Khoo ©

A thesis submitted to the Faculty of Graduate Studies and Research in partial fulfillment of the requirement for the degree of Doctor of Philosophy

in

Structural Engineering

Department of Civil and Environmental Engineering

Edmonton

Fall 2000

National Library of Canada
Acquisitions and Bibliographic Services
395 Wellington Street
Ottawa ON K1A 0N4
Canada

Bibliothèque nationale du Canada
Acquisitions et services bibliographiques
395, rue Wellington
Ottawa ON K1A 0N4
Canada

Your file Votre référence

Our file Notre référence

The author has granted a non-exclusive licence allowing the National Library of Canada to reproduce, loan, distribute or sell copies of this thesis in microform, paper or electronic formats.

L'auteur a accordé une licence non exclusive permettant à la Bibliothèque nationale du Canada de reproduire, prêter, distribuer ou vendre des copies de cette thèse sous la forme de microfiche/film, de reproduction sur papier ou sur format électronique.

The author retains ownership of the copyright in this thesis. Neither the thesis nor substantial extracts from it may be printed or otherwise reproduced without the author's permission.

L'auteur conserve la propriété du droit d'auteur qui protège cette thèse. Ni la thèse ni des extraits substantiels de celle-ci ne doivent être imprimés ou autrement reproduits sans son autorisation.

0-612-59610-9

Canada

University of Alberta

Library Release Form

Name of Author: Heng Aik Khoo

Title of Thesis: Ductile Fracture of Steel

Degree: Doctor of Philosophy

Year this Degree Granted: 2000

Permission is hereby granted to the University of Alberta Library to reproduce single copies of this thesis and to lend or sell such copies for private, scholarly, or scientific research purposes only.

The author reserves all other publication and other rights in association with the copyright in the thesis, and except as hereinbefore provided, neither the thesis nor any substantial portion thereof may be printed or otherwise reproduced in any material form whatever without the author's prior written permission.

Sept. 06, 2000

8655 108A Street, Edmonton,
Alberta, Canada. T6E 4M7

University of Alberta

Faculty of Graduate Studies and Research

The undersigned certify that they have read, and recommend to the Faculty of Graduate Studies and Research for acceptance, a thesis entitled Ductile Fracture of Steel submitted by Heng Aik Khoo in partial fulfillment of the requirements for the degree of Doctor of Philosophy in Structural Engineering.

Chair: Prof. P. Steffler

Supervisor: Prof. J.J.R. Cheng

Supervisor: Prof. T.M. Hrudey

Prof. P-Y.B. Jar

Prof. D.W. Murray

Prof. K.W. Neale

SEPT. 6, 2000

Abstract

A constitutive model that incorporates material dilation and the concept of continuum damage mechanics is developed to predict ductile fracture of steel under monotonic quasi-static loading. In this model, damage is assumed to be isotropic and is a function of the state of stress and the plastic strain increment. Material dilation is assumed to vary with the state of damage. Fracture occurs when the damage limit is reached. The constitutive model is implemented in a finite element program. Parameters used in the analyses are calibrated using data obtained from tension coupon tests. The constitutive model and the process used to determine its parameters are described.

An experimental program with rounded steel coupons was conducted to acquire test data to verify the model. A total of sixteen specimens with three different heat treatments and different geometry were tested. Each specimen was tested until fracture with regular stoppages during the test for taking the static readings and the digital photographs of the deformed shape. All specimens were monotonically loaded with the exception of two specimens, which were unloaded and reloaded intermittently during the test. The ductility of the specimen decreases as the gage length or the transition radius or both are reduced. The model is able to give a good prediction of the specimen load-deformation behaviour, the deformed shape, and the instant fracture occurs. It also captures the decrease in ductility associated with a higher hydrostatic tension stress, as occurs in the case of a shorter gage length or a smaller transition radius.

To illustrate the application of the material model, numerical simulations are carried out for some practical cases such as predicting the capacity and the failure of a steel structure connection or a corroded pipe. Existing test data for slotted tubular tension members are used in comparison. The numerical solution closely matches the measured load-deformation response, the location of fracture and the moment fracture occurs.

Acknowledgement

I would like to thank Dr. J.J. Cheng and Dr. T.M. Hrudey, supervisors of this thesis, for their advice and guidance. I also wish to thank Dr. Gilbert Grondin for guiding the thesis through its last and major stage.

To the Richard Helfrich, Clark Bicknell and Larry Burden, your help in carrying out the test are greatly appreciated.

I am also grateful for the financial assistance provided by the University of Alberta, C.W. Carry Trust, Killam Trusts and Alberta Heritage Scholarship Fund.

This research project is funded by the National Science and Engineering Research Council of Canada through Dr. J.J.R. Cheng and Dr. T.M. Hrudey.

Table of Contents

Chapter		Page
1.	Introduction	1
1.1	Objective of the Thesis and Methodology Used in the Research	2
1.2	Organization of the Thesis	3
2.	Literature Review	5
2.1	Introduction to Fracture Mechanics	5
2.2	Classical Fracture Mechanics	6
2.3	Recent Developments	8
2.3.1	Brittle Fracture	9
2.3.1.1	S-Criterion: Total Strain Energy Density Criterion	9
2.3.1.2	T-Criterion: Dilational Strain Energy Density Criterion	11
2.3.1.3	Distortional Strain Energy Density Criterion	13
2.3.1.4	Maximum Tangential Strain Energy Density Criterion	14
2.3.2	Ductile Fracture	15
2.3.2.1	Absorbed Strain Energy till Fracture	16
2.3.2.2	Continuum Damage Mechanics	16
2.3.2.3	Void Volume Fraction Criteria	19
2.3.2.4	Other Damage Limits	21
3.	Proposed Model	26
3.1	Basis of the Model	26
3.2	Physical Interpretation and Assumptions	28
3.3	Mathematical Formulation and Assumptions	28
3.4	Summary of the Assumptions and Limitations for the Proposed Model	32
3.5	Numerical Implementation in ABAQUS	33
3.5.1	Assumptions in the Numerical Implementation	34
3.5.2	Formulation to Solve for $\Delta\tilde{\sigma}$ in a Time Step	35
3.5.3	Jacobian Matrix of the Constitutive Model	38
3.5.4	Special Considerations	40
3.5.4.1	Procedure to Safeguard against Damage Growth with Hydrostatic Compression	41

3.5.4.2 Three-Dimensional Stress-Strain Problems 43
4. Testing Program 47
4.1 Objective 47
4.2 Test Specimens 47
4.3 Test Set-up and Instrumentation 48
4.4 Test Procedure 50
5. Analyses and Test Results 54
5.1 Test Results and Discussions 54
5.2 Assessing the Measurement from Digital Camera 55
5.3 Procedure for Obtaining Parameters for the Model 56
5.4 Numerical Analyses of Test Specimens 59
5.4.1 AS Heat Treatment 60
5.4.2 AN Heat Treatment 63
5.4.3 NM Heat Treatment 64
5.4.4 Overall Results of Numerical Analyses 65
5.5 Sensitivity of the Axial Deformation to Geometric Imperfection 66
5.6 Comparison to Models by Matic et al. and Lemaitre 67
5.7 Obtaining Parameters and Material Properties in Practical Application 68
6. Application of the Damage Model 124
6.1 Numerical Simulation 124
6.2 Slotted Tubular Tension Member 126
6.3 Machined Corrosion Pipe 128
7. Summary, Conclusions and Recommendations 152
7.1 Summary 152
7.2 Conclusions 154
7.3 Recommendations 156
References 157
Appendix A - Mesh Study 162
Appendix B - Measured Stress versus Extensometer Strain Curves 165

List of Tables

Table		Page
5.1	Measured peak stress and diameter D4 at fracture	70
5.2	Comparison of camera and caliper data	70
5.3	Engineering stress versus engineering strain used for NM heat treatment	71
5.4	Engineering stress versus engineering strain used for AN heat treatment	72
5.5	Engineering stress versus engineering strain used for AS heat treatment	73
5.6	Material properties and parameters used in the analyses for AS heat treatment	74
5.7	Calculated err for AS heat treatment	75
5.8	Measured and predicted diameter D4 at fracture for AS heat treatment with $D_o = 1.078 \times 10^5$ (MPa)^2 and the corresponding calculated D_c	75
5.9	Measured and predicted diameter D4 at fracture for AS heat treatment with constant $D_c = 0.278$	75
5.10	Measured and predicted peak stress for AS heat treatment	76
5.11	Material properties and parameters used in the analyses for AN heat treatment	76
5.12	Calculated err for AN heat treatment	77
5.13	Measured and predicted diameter D4 at fracture for AN heat treatment with $D_o = 7.78 \times 10^4$ (MPa)^2 and the corresponding calculated D_c	77
5.14	Measured and predicted diameter D4 at fracture for AN heat treatment with constant $D_c = 0.216$	77
5.15	Measured and predicted peak stress for AN heat treatment	77
5.16	Material properties and parameters used in the analyses for NM heat treatment	78
5.17	Calculated err for NM heat treatment	78
5.18	Measured and predicted diameter D4 at fracture for NM heat treatment with $D_o = 5.34 \times 10^4$ (MPa)^2 and the corresponding calculated D_c	79
5.19	Measured and predicted diameter D4 at fracture for NM heat treatment with constant $D_c = 0.166$	79

5.20 Measured and predicted peak stress for NM heat treatment 79
5.21 Calculated D_c at fracture for specimens with 5 mm transition radius..... 80
5.22 Material properties and parameters used in the analyses for models by Lemaitre and Matic et al..... 80
5.23 Err values for different material models 81
5.24 Predicted diameter D4 at fracture for various material models 81
6.1 Material properties and parameters used in the analyses for the slotted tubular tension member tests..... 132
6.2 Ultimate tensile strength of the materials for slotted tubular tension member tests..... 133
6.3 Test and predicted fracture location..... 133
6.4 Test and predicted results of the slotted tubular tension member tests..... 133
6.5 Pipe dimensions 134
6.6 Ultimate tensile strength of the pipe 134
6.7 Material properties and parameters used in the analyses for the machined corrosion pipe..... 135

List of Figures

Figure		Page
2.1	Mechanism of ductile fracture in metal	23
2.2	Typical relationship of the loading rate, temperature and level of energy absorption until fracture	24
2.3	Through-thickness crack in an infinitely wide plate subjected to a remote tensile stress	24
2.4	Sih's criterion, total strain energy density along the path at a distance r away from the crack tip	25
2.5	Nominal and effective stresses in continuum damage mechanics	25
3.1	Cross-section surface of a damaged body in the $\hat{n}_i$ direction	45
3.2	The assumed relationship of the void and the material matrix in a damaged body	45
3.3	Flow chart for the subroutine	46
4.1	Dimensions of test specimens	51
4.2	Measurements taken in testing	51
4.3	Test set-up	52
4.4	Attachment assembly for digital camera	52
4.5	Positioning of digital camera	53
4.6	Typical loading sequence of monotonic, and load and unload test	53
5.1	Measured stress versus change in diameter D4 for AS heat treatment	82
5.2	Measured stress versus change in diameter D4 for NM heat treatment	82
5.3	Measured stress versus change in diameter D4 for AN heat treatment	83
5.4	Measured stress versus change in diameter D4 for monotonic, and load and unload tests	83
5.5	Measured apparent elastic modulus versus change in diameter D4 for load and unload specimens	84
5.6	Fracture of AN heat treatment specimens	85
5.7	Fracture of NM heat treatment specimens	86
5.8	Fracture of AS heat treatment specimens	87
5.9	Fracture of AS heat treatment specimens	88

5.10 G2 and G3 extensions from caliper and camera for AS1g6r5 89
5.11 G2 and G3 extensions from caliper and camera for AS1g12r5 89
5.12 D4 diameter measurement from caliper and camera..... 90
5.13 Finite element mesh for AS1g2r15 91
5.14 Finite element mesh for AS1g2r5, NM1g2r5 and AN1g2r5..... 92
5.15 Finite element mesh for AS1g6r5, NM1g6r5 and AN1g6r5..... 93
5.16 Finite element mesh for AS1g12r5, NM1g12r5 and AN1g12r5..... 94
5.17 Finite element mesh for AS1g50r5, NM1g50r5 and AN1g50r5..... 95
5.18 Finite element mesh for AS1g50r7 96
5.19 Measured and analytical stress versus change in diameter D4 for AS1g50r5 . 97
5.20 Measured and analytical stress versus change in diameter D4 for AS1g50r7 . 97
5.21 Measured and analytical stress versus change in diameter D4 for AS1g12r5 . 98
5.22 Measured and analytical stress versus change in diameter D4 for AS1g6r5 ... 98
5.23 Measured and analytical stress versus change in diameter D4 for AS1g2r5 ... 99
5.24 Measured and analytical stress versus change in diameter D4 for AS1g2r15 . 99
5.25 Measured and analytical stress versus extensometer displacement for AS1g12r5 100
5.26 Measured and analytical stress versus extensometer displacement for AS1g6r5 100
5.27 Measured and analytical stress versus extensometer displacement for AS1g2r5 101
5.28 Measured and analytical stress versus extensometer displacement for AS1g2r15 101
5.29 Measured and analytical extensometer displacement versus change in diameter D4 for AS1g12r5..... 102
5.30 Measured and analytical extensometer displacement versus change in diameter D4 for AS1g6r5..... 102
5.31 Measured and analytical extensometer displacement versus change in diameter D4 for AS1g2r5..... 103
5.32 Measured and analytical extensometer displacement versus change in diameter D4 for AS1g2r15..... 103

5.33 Measured and analytical extensometer displacement versus change in diameter D4 for AS specimens with gage length less than 12 mm and n = 0.5 104
5.34 Measured and analytical extensometer displacement versus change in diameter D4 for AS specimens with gage length less than 12 mm and n = 1.0 104
5.35 Measured and analytical stress versus change in diameter D4 for AS specimens with gage length less than 12 mm and n = 0.5 105
5.36 Measured and analytical stress versus change in diameter D4 for AS specimens with gage length equal to 50 mm and n = 0.5 105
5.37 Measured and predicted apparent elastic modulus versus change in diameter D4 for load and unload specimens 106
5.38 Measured and analytical stress versus change in diameter D4 for AN1g50r5. 106
5.39 Measured and analytical extensometer displacement versus change in diameter D4 for AN1g2r5 107
5.40 Measured and analytical extensometer displacement versus change in diameter D4 for AN specimens with gage length less than 12 mm and n = 0.5 107
5.41 Measured and analytical extensometer displacement versus change in diameter D4 for AN specimens with gage length less than 12 mm and n = 1.0 108
5.42 Measured and analytical stress versus change in diameter D4 for AN specimens with n = 0.5 108
5.43 Measured and analytical stress versus change in diameter D4 for NM1g50r5 109
5.44 Measured and analytical extensometer displacement versus change in diameter D4 for NM1g12r5 109
5.45 Measured and analytical extensometer displacement versus change in diameter D4 for NM specimens with gage length less than 12 mm and n = 1.5 110

5.46 Measured and analytical extensometer displacement versus change in diameter D4 for NM specimens with gage length less than 12 mm and n = 1.0 110
5.47 Measured and analytical stress versus change in diameter D4 for NM specimens with n = 1.5 111
5.48 Superposition of the deformed mesh on the 50 mm gage length specimen at close to fracture 111
5.49 Superposition of the deformed mesh on the 12 mm gage length specimen at close to fracture 112
5.50 Superposition of the deformed mesh on the 2 mm gage length specimen at close to fracture 112
5.51 Superposition of the undeformed mesh on AS1g12r5 before any application of load 113
5.52 Contour plot of the damage state D at close to fracture for AS1g2r5 114
5.53 Contour plot of the negative hydrostatic pressure ($-\sigma_h$) at close to fracture for AS1g2r5 114
5.54 Contour plot of the damage state D at close to fracture for AS1g12r5 115
5.55 Contour plot of the negative hydrostatic pressure ($-\sigma_h$) at close to fracture for AS1g12r5 115
5.56 Contour plot of the damage state D at close to fracture for NM1g2r5 116
5.57 Contour plot of the negative hydrostatic pressure ($-\sigma_h$) at close to fracture for NM1g2r5 116
5.58 Analytical effective hydrostatic tension stress versus change in diameter D4 for AN heat treatment at the mid-length along the axis of the specimen 117
5.59 Analytical effective hydrostatic tension stress versus change in diameter D4 for NM heat treatment at the mid-length along the axis of the specimen 117
5.60 Patterns of imperfection 118
5.61 Stress versus change in diameter D4 for various imperfection patterns 119
5.62 Stress versus change in end displacement for various imperfection patterns .. 119
5.63 Deformed mesh for various imperfection patterns 120

5.64 Measured and analytical stress versus change in diameter D4 with different material models for AN1g50r5 121
5.65 Measured and analytical stress versus change in diameter D4 with different material models for AS1g6r5 121
5.66 Measured and analytical extensometer displacement versus change in diameter D4 with different material models for AS1g2r5 122
5.67 Measured and analytical extensometer displacement versus change in diameter D4 with different material models for AS1g6r5 122
5.68 Choice of n based on final cross-section area of tension coupon test 123
6.1 Dimensions for the slotted tubular tension member test 136
6.2 Idealized stress versus change in cross-section for the HSS section tension material test 137
6.3 Idealized stress versus change in cross-section for the gusset plate tension material test 137
6.4 Typical finite element mesh for modeling slotted tubular tension member tests 138
6.5 Specimen SPEC1, the typical test and predicted deformed shape for fracture at the mid-length of the specimen 138
6.6 Contour plot of the hoop stress on the HSS section for PWC1 139
6.7 Contour plot of the longitudinal stress on the HSS section for PWC1 139
6.8 Stress contour plot on the HSS section for SPEC2 140
6.9 Test and predicted load versus deformation curve for PWC1 140
6.10 Test and predicted load versus deformation curve for PWC2 and PWC6 141
6.11 Test and predicted load versus deformation curve for SPEC1 141
6.12 Test and predicted load versus deformation curve for SPEC2 142
6.13 Loading in the machined corroded pipe test 143
6.14 Pipe II with the circumferential groove machined corrosion 144
6.15 Pipe III with the square patch machined corrosion 144
6.16 Finite element mesh for IB 145
6.17 Finite element mesh for IIB and the close-up of the machined corrosion 145
6.18 Finite element mesh for IIIB and the close-up of the machined corrosion 146

6.19 Idealized stress versus change in cross-section for the pipe tension material test 146
6.20 Predicted deformed shape 147
6.21 Predicted moment versus global curvature for pipe I 147
6.22 Contour plot of the outer surface damage state D for IB corresponding to the load point 1 148
6.23 Contour plot of the outer surface von Misés stress (σ_{eq}) for IB corresponding to the load point 1 148
6.24 Predicted moment versus global curvature for pipe II 149
6.25 Predicted moment versus global curvature for pipe III 149
6.26 Contour plot of the outer surface damage state D at the machined corrosion for IIA corresponding to the load loading stage where the critical damage limit D_c, calculated using (6.4), is first exceeded 150
6.27 Contour plot of the outer surface von Misés stress (σ_{eq}) at the machined corrosion for IIA corresponding to the loading stage where the critical damage limit D_c, calculated using (6.4), is first exceeded. 150
6.28 Contour plot of the outer surface damage state D at the machined corrosion for IIIA corresponding to the loading stage where the critical damage limit D_c, calculated using (6.4), is first exceeded. 151
6.29 Contour plot of the shell thickness at the machined corrosion for IIIA corresponding to the loading stage where the critical damage limit D_c, calculated using (6.4), is first exceeded. 151
A.1 Finite element mesh scheme-1 at the mid-length of AS1g50r5. 163
A.2 Finite element mesh scheme-2 at the mid-length of AS1g50r5. 163
A.3 Analytical stress versus change in diameter D4 for AS1g50r5 with different mesh schemes. 164
A.4 Analytical damage state versus change in diameter D4 for different mesh schemes at the mid-length along the axis of AS1g50r5. 164
B.1 Measured stress versus extensometer strain for monotonically loaded g50r5 specimens. 165

List of Symbols

a	-	the linear dimension of the cube.
A	-	the current transverse cross-section area.
A_o	-	the undeformed cross-section area.
A_f	-	the cross-section area at fracture.
b	-	one-half crack length, or the linear dimension of the cube.
B	-	a parameter in Tvergaard's model, or a parameter used in the numerical implementation of the proposed damage model (B = 2 for 2-D, B = 3 for 3-D).
c	-	a parameter in the model by Norris et al
C	-	the tangential strain energy factor, or the material constant in the model by Tai and Yang.
C_{cr}	-	the critical tangential strain energy factor limit.
CTOD	-	crack tip opening displacement.
CST1	-	an equation in the numerical implementation.
d	-	the current transverse cross-section diameter.
d_o	-	the undeformed cross-section diameter.
d_f	-	the diameter at fracture.
D	-	the state of damage, or a parameter in Tvergaard model.
D_c	-	the critical damage limit.
D_i	-	the damage variable on a surface with a unit normal $\hat{n}_i$.
D_o	-	the initial damage at a very small strain, or the material constant for calculating D_c.
err	-	a calculated term used for checking the match of predicted and measured extensometer-radial deformations.
e_{ij}^p	-	the Lagrangian strain.
$(dW/dV)_c$	-	the critical strain energy density.
$(dW/dV)_T$	-	the total strain energy density.

$(dW/dV)_d$	-	the distortional strain energy density.
$(dW/dV)_v$	-	the dilational strain energy density.
E	-	the modulus of elasticity.
E_t	-	the tangent modulus.
f	-	the void volume fraction.
f_c	-	the critical void volume fraction.
f_F	-	the void volume fraction at fracture.
f^*	-	a parameter in Tvergaard's model.
G	-	the energy release rate, or the modulus of rigidity.
G_I, G_I, G_{III}	-	energy release rates in tension, shear and tearing respectively.
HLD	-	an equation in the numerical implementation.
i	-	superscript i denotes the beginning of time step i.
i+1	-	superscript i+1 denotes the beginning of time step i+1.
J	-	the energy release rate according to J-integral.
J_c	-	the J-integral at the crack initiation at the crack tip.
J_{Ic}	-	the energy release rate according to J-integral corresponds to K_{Ic}.
K	-	the stress intensity factor, or the material coefficient in Ramberg-Osgood model, or a parameter in Tvergaard's model.
K_I	-	the stress intensity factor in mode I.
K_{Ic}	-	the plane strain fracture toughness for mode I.
M, N	-	the material coefficient in Ramberg-Osgood model.
m	-	an exponent in the function to calculate D_c.
n	-	the material coefficient in Ramberg-Osgood model, or an exponent that governs the damage rate.
$\hat{n}_i$	-	the unit normal to the surface.
p	-	the equivalent accumulated plastic strain.
p_c	-	the p associated with D_c.
p_D	-	the plane strain threshold below which no damage occurs.

p_o - the p associated with D_o.

q - the heat flux.

q_1, q_2, q_3 - adjustable parameters for Tvergaard's model.

r - the distance from the point of crack initiation, or the radius of a sphere.

r_o, r_c - the radius of the core region, or the critical dimension when fracture occurs.

R - the average radius of void.

R_o - the initial void size.

$(R/R_o)_c$ - the critical void growth rate.

s - a parameter that governs the damage rate.

S - the strain energy density factor or the gross area.

S_c - the critical strain energy density factor limit.

S_d - the distortional strain energy density factor.

S_e - the effective area.

S_g - the gross cross-section area.

S_{ij} - the deviatoric strain tensor.

S_o - the area of cracks and cavities.

t - time.

T - temperature, or the total strain energy density.

T_d - the distortional strain energy density.

$T_{d,el}$ - the elastic distortional strain energy density.

$T_{d,pl}$ - the elastic distortional strain energy density.

T_v - the dilational strain energy density.

$T_{v,el}$ - the elastic dilational strain energy density.

V - volume.

V_{DC} - the damage limit according to the model by Tai and Yang.

W - the strain energy.

W_{DC} - the fracture limit according to the model by Wang.

W_e - the elastic strain energy density.

W_θ - the tangential strain energy density.

y - the damage strain energy release rate.

α - a constant that depends on stress state and material properties in CTOD, or a damage coefficient in the model by Wang, or an increasing function of inclusion volume fraction.

δ - the crack tip opening displacement.

δ_{ij} - Kronecker delta.

Δ - denotes changes that occur in a time step or an iteration.

$\Delta\varepsilon^{tv}$ - the sum of the initial elastic volumetric strain and the volumetric component of strain increment.

$\Delta\varepsilon^{nt}$ - the net strain increment after subtracting the initial elastic volumetric strain and the volumetric component of strain increments.

ε - the strain.

$\varepsilon^e, \varepsilon^e_{ij}$ - the elastic strain.

ε_{eq} - the equivalent von Misés strain.

ε^f_{eq} - the strain at fracture.

ε^d_{eq} - the strain at nucleation.

ε^p_{eq} - the strain at nucleation, or the equivalent plastic strain.

$\varepsilon^p_{eq_c}$ - the damage initiation equivalent plastic strain.

$\varepsilon^p_{eq_f}$ - the equivalent plastic strain at fracture.

ε_{ij} - the strain tensor.

ε^p_M - the effective plastic strain.

$\varepsilon^p, \varepsilon^p_{ij}$ - the plastic strain.

$\varepsilon^v, \varepsilon_{ij}^v$ - the plastic volumetric strain.

ε_θ - the circumferential strain.

ϕ - the plastic potential.

γ_p - the plastic deformation energy.

γ_s - the specific surface energy.

φ^* - the potential for dissipation.

Λ - a parameter determined from consistency equation.

σ - the stress.

σ_{ij} - the stress tensor or the Cauchy stress tensor.

σ_{eq} - the von Misés stress.

σ_h - the hydrostatic stress.

σ_u - the ultimate tensile strength.

σ_y - the yield stress.

σ_m - the hydrostatic stress.

σ_M - the stress related to ε_M^p.

σ_θ - the circumferential stress.

θ - angle.

θ^* - the angle of crack propagation.

ν - Poisson's ratio.

$\sim$ - superposed ~ denotes the effective stresses or effective resisting area.

$\dot{}$ - superposed dot denotes the time rate of change.

1 Introduction

In civil engineering application, steel is used extensively as one of the major construction materials for structures and as pipes for sewage, oil and gas lines. It is essential that the material behaviour be understood so that structures and pipelines can be designed economically and safely.

In general, the strength of a particular type of steel is determined by testing a simple steel rod or strip. The maximum load achieved from such a test is used to establish the ultimate strength of the steel. However, the steel specimen tested does not break and rupture at the instant the maximum load is reached, and instead, will undergo further extension beyond the maximum load before breakage and rupture occur. In most situations, such as the connections in a steel structure or a corroded pipe, the loading is uneven across the structure. Thus, the material at different points in the structure does not reach the ultimate strength simultaneously. In view of this, it is essential that the actual behaviour up to the point of breakage and rupture be known so that the capacity of the steel structure can be analyzed accurately.

Ductile fracture is the predominant mode of fracture experienced in structural engineering applications. This mode of fracture is characterized by microvoid coalescence, which involves material dilation due to void growth. Thus a constitutive model for ductile fracture of steel should take into account the effect of void growth on the material. However at present, there is no simple constitutive model that takes into account the material dilation due to void growth. Furthermore, most existing constitutive models for predicting ductile fracture have not been extensively verified with test data. Thus there is a need to have a simple constitutive model that is able to predict ductile fracture and is easily calibrated with data from a tension coupon test.

Currently, the only way to evaluate accurately the capacity of a complicated steel structural component is through direct testing of the component. A simple material model that is easily calibrated will provide a useful alternative, as it would allow a numerical testing of the complicated structural components thus avoiding costly physical tests. It provides an economical and flexible way to analyze steel structures for different loading situations and facilitates the development of new recommendations for design codes.

1.1 Objective of the Thesis and Methodology Used in the Research

The objective of the thesis is to develop a material model that can closely represent the behaviour of steel until fracture. A constitutive model with an isotropic hardening that incorporates material dilation and the concept of continuum damage mechanics is developed to predict ductile fracture for a monotonic quasi-static loading. It is modified from the model by Lemaitre (1984) to include material dilation. In the proposed model, damage is assumed to be isotropic and is a function of the state of stress and the plastic strain increment. Material dilation is assumed to vary with the state of damage. Fracture occurs when the damage limit is reached. The critical damage limit is assumed to be proportional to the inverse square of the hydrostatic tension stress. The constitutive model is then implemented in an existing commercial finite element program ABAQUS through a user-defined material subroutine. Numerical analyses using the constitutive model are performed using the updated Lagrangian formulation to better represent the considerable change in shape that occurs before fracture. All numerical analyses are carried out with ABAQUS.

In order to validate the material model, test results from a number of round tension coupons are compared to solutions predicted by the proposed material model. Parameters used in the numerical analyses are calibrated by trial and error through the numerical simulation to match the test result. A total of sixteen specimens with three different heat treatments were tested: as supplied A516 grade steel without any additional heat treatment, the same heat of A516 steel heated to 900°C then annealed, and another batch heated to 1250°C then normalized. These coupons have different diameters, transition radii and gage lengths. Specimens with different heat treatments and dimensions were used in order to obtain data from materials with inherently different ductility and from specimens experiencing different levels of hydrostatic tension stress. Thus, these data would provide a good basis for studying the proposed constitutive model. Digital photos of the coupons taken at different stages of loading were also used to compare the predicted and actual deformed shape.

To illustrate the application of the material model, numerical simulations are carried out for two practical cases: predicting the capacity and the failure of a slotted tube

structural connection and a corroded pipe. Existing test data for slotted tubular tension members are used in comparison. In a tubular tension member test, end connections are created by cutting a longitudinal slot in the tube and inserting a gusset plate, which is then welded to the tube using a parallel longitudinal fillet weld. A stress concentration occurs at the slotted end for this type of connection. Depending on the stress concentration level, premature fracture at the slotted end may reduce the capacity and the ductility of the tension member. In corroded pipes, regions of the pipe are machined so as to reduce the wall thickness, and thereby simulate the effects of corrosion. This creates a weakened region in the pipe, thus inducing a stress concentration and a reduction in the overall ductility.

1.2 Organization of the Thesis

Chapter 2 consists of a literature review on the fracture of metals. The review includes a brief discussion of fracture mechanics. In addition, various constitutive and failure models by other researchers for predicting fracture are presented.

In Chapter 3 the proposed continuum damage model is discussed. The chapter is divided into two parts. The first deals with the development of the model. In this part the assumptions, the bases for and the limitations of the model are listed. The second part contains a description of how the model is implemented into the finite element program.

Chapter 4 contains a description of the experimental program of round tension coupons carried out to acquire data for studying the material model.

In Chapter 5 the analytical and test results are discussed. Results from the test program are reviewed and compared to the numerical solutions using the proposed model. The procedure for calibrating the material properties and parameters for carrying out the analyses are also presented. Using the calibrated parameters, numerical simulations for all monotonically loaded specimens are performed and studied. Solutions from fracture models by two other researchers are also included in the investigation.

In Chapter 6 the application of the proposed model is illustrated. Numerical simulations of actual slotted tubular tension member tests and fictitious machined corrosion pipe tests are carried out. Comparisons are made between the test and analytical results of slotted tubular tension member tests.

Chapter 7 consists of a summary and conclusions.

2 Literature Review

In structural engineering, the ultimate limit states of a structural component are generally determined by its maximum load carrying capacity. This capacity is normally governed by either the yield strength or the tensile fracture. However, the stress distribution is seldom uniform across a structural component. Fracture may occur before the overall cross section reaches general yielding or tensile strength. In this situation, the ability to predict the initiation and progression of cracks is critical in evaluating the capacity of the component.

2.1 Introduction to Fracture Mechanics

Fracture mechanics deals with the fracture of solids. There are three basic mechanisms of fracture for metals: microvoid coalescence, cleavage, and intergranular fracture. Microvoid coalescence is a ductile process, whereas cleavage and intergranular fracture are both brittle processes. These processes are greatly influenced by the temperature, strain-rate, and triaxial stresses. A complete fracture of a structural component normally involves the combination of ductile and brittle processes.

Cleavage is a transgranular fracture. It occurs along specific crystal planes. Fissures for the intergranular fracture follow the grain surfaces. Both of these failure modes involve little ductility, and thus they are not desirable in structural engineering applications. Microvoid coalescence is also a transgranular fracture. However, this mode of failure possesses greater ductility, and is the mode of failure preferred in structural engineering applications. For ductile steel, microvoids form as the deformation increases. The formation of microvoids is a result of either particle cracking, or the separation of an inclusion, or a precipitate particle from the surrounding matrix. These microvoids grow in size and coalesce, and eventually lead to rupture. The mechanism of this process, as illustrated by Anderson (1991), is shown in Figure 2.1.

Toughness is a term used for describing the fracture property of a solid. It indicates the resistance of the material to crack extension. High toughness means that a large amount of energy is required to split the material. Conversely, low toughness implies little energy is needed to bring about fracture. Low toughness is normally associated with brittle materials. However, the ability of a material to absorb energy until

fracture depends on the state of stress, the loading rate, and the temperature at which it operates. Figure 2.2 shows the relationship of the loading rate, the temperature and the level of energy absorption until fracture for steel. The level of energy absorption increases with higher temperature and slower loading rate.

2.2 Classical Fracture Mechanics

Griffith (1921) was first to introduce a quantitative relation for the fracture of cracked solids. For the configuration shown in Figure 2.3, Griffith deduced that the equilibrium condition at which the energy released by the crack growth is equal to the energy required to create the new surfaces for a plane strain state is given by

$$\sigma = \sqrt{\frac{2E\gamma_s}{\pi b}}. \tag{2.1}$$

E = modulus of elasticity,

σ = applied stress,

γ_s = specific surface energy and

b = one-half crack width.

The elastic energy release rate per crack tip is

$$G = \frac{\sigma^2 \pi b}{E}. \tag{2.2}$$

G is per unit plate thickness and per unit crack extension. In the formulation for the critical stress at the equilibrium state, the crack is assumed to be very sharp. Griffith's findings are based on test results using glass. However unlike glass, which is very brittle, most engineering materials experience considerable plastic deformation in conjunction with crack growth. Irwin (1947) extended Griffith's equation to include plasticity at the crack tip. The modified equation introduces an additional term γ_p to (2.1), and yields

$$\sigma = \sqrt{\frac{2E(\gamma_s + \gamma_p)}{\pi b}} \tag{2.3}$$

and γ_p is the plastic deformation energy. The energy release rate G is the driving force for the crack growth. Unstable crack growth occurs when the energy release rate exceeds the energy consumed to create a longer crack. Subsequent advances in fracture

mechanics utilize the energy release rate approach as a basis in quantifying the fracture relations of cracked solids for engineering applications.

Currently, there are three established approaches in dealing with fracture of cracked solids: linear elastic fracture mechanics (LEFM), which uses the stress intensity factor K; elastic-plastic fracture mechanics (EPFM), which uses the J-integral; and the crack tip opening displacement (CTOD) method. In LEFM for plane strain conditions, the stress intensity factor K is related to the energy release rate through

$$G = \frac{(1-\nu^2)K^2}{E} \text{ with} \tag{2.4}$$

ν = Poisson's ratio.

As the name implies, this relationship only applies for the situation where there is little or essentially no crack tip plasticity. Mode I (tensile) fracture is the mode most often encountered in engineering applications. The stress intensity factor limit for Mode I, denoted as K_{Ic}, is determined through testing of each material. This limit provides a measure of the material fracture toughness, and is used in the design or the evaluation of a cracked solid. In order to obtain a valid K_{Ic} value, the test specimen must experience little crack tip plasticity and the region at the crack tip must be predominantly in a state of plane strain. For a tough material, however, there is considerable plasticity at the crack tip. Thus, there may be no practical way of obtaining a valid K_{Ic} directly from the test. Furthermore, the energy release rate G cannot be determined by the elastic stress field if there is significant plasticity. Rice (1968) applied the path independent J-integral to determine the energy release rate where the plasticity effect is appreciable. J is equivalent to the energy release rate G. Analogous to K_{Ic}, J_{Ic} can be used to characterize the fracture toughness of the material. The relationship between K_{Ic} and J_{Ic} can be expressed as

$$J_{Ic} = \frac{(1-\nu^2)K_{Ic}^2}{E}. \tag{2.5}$$

The size requirement for the test specimen to obtain a valid J_{Ic} value is much smaller than for K_{Ic}. The third approach is CTOD method. The CTOD method is valid for both elastic and elastic-plastic conditions. This method is more empirical compared to LEFM

and EPFM. Similar to K_{Ic} and J_{Ic}, there is also a corresponding CTOD limit. However unlike K_{Ic} and J_{Ic}, the CTOD limit only applies to each specific plate thickness tested. The relationship between J and CTOD is

$$J = \alpha \sigma_y \delta \text{ with} \tag{2.6}$$

α = constant that depends on stress state and material properties,

σ_y = yield stress and

δ = CTOD.

A more thorough treatment of LEFM, EPFM and CTOD can be found in Anderson (1991), Broek (1986) and Hertzberg (1989).

2.3 Recent Developments

In the Griffith-Irwin approach to linear elastic fracture mechanics, a crack is assumed to propagate if the energy release rate due to the crack advance is greater than the energy required to form new fractured surfaces. A crack is assumed to grow in a self-similar manner and its corresponding energy release rates are G_I, G_{II} and G_{III} for fractures in modes I, II and III (tension, shear and tearing), respectively. The assumption that the crack will grow in a self-similar manner is valid for the mode I fracture. However, for mode II and III, a crack does not grow along the crack plane. Thus, in order to use the energy release rate approach for mixed mode problems, the crack growth direction has to be known in advance. Furthermore, there is a need to have a better approach than the LEFM, EPFM and CTOD methods to deal with ductile fracture. Even in EPFM, the material behaviour is not truly elastic-plastic. In the formulation for the Hutchinson-Rice-Rosengren (HRR) stress field in EPFM by Rice and Rosengren (1968), and Hutchinson (1968), the material is assumed to follow the recoverable deformation theory of plasticity, which essentially is hyperelastic behaviour. Due to the limitation of the original Griffith-Irwin approach, various fracture criteria have been proposed to address the mixed mode fracture problems and to predict the direction of crack growth, for both brittle and ductile fractures.

2.3.1 Brittle Fracture

Most of the new criteria dealing with brittle fracture utilize the K-field (stress field from LEFM) and HRR field (stress field from EPFM) to predict the crack growth direction and initiation. Some of these criteria were further extended to include ductile fracture. However, the validity of these extensions is questionable since they were originally developed based on the K-field. There are limitations to the applications of these criteria. First, it is difficult to implement these criteria in a finite element analysis. Second, the calculation for the material damage to indicate the onset of crack growth is measured at a distance away from the crack tip. However, the crack initiation is triggered by the damage at the crack tip. A few examples of these criteria are presented below.

2.3.1.1 S-Criterion: Total Strain Energy Density Criterion

Sih (1973a, b) proposed a criterion using total strain energy density to predict the crack advance for brittle fracture. There are two basic assumptions in his criterion.

i) The crack will extend towards the point of minimum total strain energy density (the maximum potential energy density) along a circular path centered at the crack-tip.

ii) The onset of the crack propagation coincides with the minimum total strain energy density factor S attaining its critical value S_c. The strain energy density factor S is defined as

$$S = (dW/dV)/r. \tag{2.7}$$

W is the strain energy, V is the volume, (dW/dV) is the strain energy density and r is the distance from the point of crack initiation such as a crack tip. Assumption (i) can be satisfied by having $\frac{\partial S}{\partial \theta} = 0$ and $\frac{\partial^2 S}{\partial \theta^2} > 0$ at $\theta = \theta^*$, where S is evaluated along a path with constant r (circular), and θ^* is the angle of crack propagation. The distance r has to be outside a circular core region of radius r_o, but the value of r_o was not clearly defined. The critical strain energy factor S_c is defined as

$$S_c = \frac{(1+\nu)(1-2\nu)K_{Ic}^2}{2\pi E} \tag{2.8}$$

where ν is the Poisson's ratio, E is the Young's modulus and K_{Ic} is the fracture toughness.

The criterion was further modified by Sih and Madenci (1983), and Sih and Li (1993) to include elastic-plastic behaviour and subcritical crack growth. The S-Criterion in its new form involves three hypotheses:

i) Evaluating the total strain energy density (dW/dV) along the path of constant r, fracture is assumed to coincide with the location of the largest total strain energy density $(dW/dV)_{min}^{max}$ among all the local minimums, and yielding is assumed to coincide with the location of the maximum total strain energy density $(dW/dV)_{max}^{max}$. This hypothesis is illustrated in Figure 2.4.

ii) Crack growth occurs when $(dW/dV)_{min}^{max}$ reaches its critical value $(dW/dV)_c^*$ and yielding occurs when $(dW/dV)_{max}^{max}$ reaches its critical value $(dW/dV)_y$.

iii) Stable crack growth or yielding growth will proceed until the incremental growth r exceeds a critical value r_c or r_y at which point the growth becomes unstable. The amount of incremental growth $r_1, r_2, r_3, \ldots\ldots r_c$ or r_y is governed by

$$\left(\frac{dW}{dV}\right)_c^* \text{ or } \left(\frac{dW}{dV}\right)_y = \frac{S_1}{r_1} = \frac{S_2}{r_2} = \ldots\ldots = \frac{S_n}{r_n} = \ldots\ldots = \frac{S_c}{r_c} \text{ or } \frac{S_y}{r_y} = \text{constant.} \quad (2.09)$$

S_c is the same as before for the brittle fracture, r_c and r_y are the ligament lengths that identify with the onset of unstable growth for fracture and yielding respectively.

The total strain energy density dW/dV can be separated into the strain energy density due to the plastic deformation $(dW/dV)_p$ and the elastic strain energy density $(dW/dV)^*$ where $dW/dV = (dW/dV)_p + (dW/dV)^*$. The critical values $(dW/dV)_c^*$ and $(dW/dV)_c$ are defined as follows:

$$\left(\frac{dW}{dV}\right)_c = \left(\frac{dW}{dV}\right)_p + \left(\frac{dW}{dV}\right)_c^*. \quad (2.10)$$

$$\left(\frac{dW}{dV}\right)_c = \int_0^{\varepsilon_f} \sigma_{ij} d\varepsilon_{ij} . \tag{2.11}$$

$(dW/dV)_c$ is the strain energy absorbed until fracture and $(dW/dV)_c^*$ is the strain energy density prior to reaching the critical value. For a hyperelastic material, $(dW/dV)_c^* = (dW/dV)_c$.

2.3.1.2 T-Criterion: Dilational Strain Energy Density Criterion

Theocaris and Andrianopoulos (1982) proposed a fracture criterion based on the maximum dilational strain energy density as opposed to the minimum total strain energy density used in the S-Criterion. The total strain energy is divided into the distortional strain energy density T_d and the dilational strain energy density T_v where T_v is associated with the volume change. The criterion assumes that:

i) A crack starts to propagate when the maximum dilational strain energy density at the vicinity of the crack tip reaches a critical value, $T_{v,cr}$.

$$T_v\Big|_{\theta=\theta^*} \geq T_{v,cr} \tag{2.12}$$

where $T_v\Big|_{\theta=\theta^*}$ is the maximum dilational strain energy density and θ^* is the direction of the crack growth.

ii) The crack will propagate in the direction of the maximum dilational strain energy $T_v\Big|_{\theta=\theta^*}$ where T_v is evaluated along the contour of the elastic-plastic boundary (the path where distortional strain energy T_d is constant).

$$\left.\frac{\partial T_v}{\partial \theta}\right|_{\theta=\theta^*} = 0 . \tag{2.13}$$

$$\left.\frac{\partial^2 T_v}{\partial \theta^2}\right|_{\theta=\theta^*} < 0 . \tag{2.14}$$

Andrianopoulos and Theocaris (1988) outlined the procedure to calculate the crack initiation load using the T-Criterion. The direction of the crack growth is still determined

by the maximum T_v along the elastic-plastic boundary. However, to determine the crack growth load, the $T_v\big|_{\theta=\theta^*}$ from assumption (i) is calculated at a location other than the point on the elastic-plastic boundary. It is calculated at a point $r(\theta^*)_\beta$ and at the angle θ^* from the crack tip. The angle β is the included angle made by the far field uniaxial load and the crack plane. The distance $r(\theta^*)_\beta$ is defined as follows:

i) For a brittle material, after the initial creation of a small plastic zone, the plastic zone is assumed to retain its shape, which is independent of any further increase of the far field load. The radius of this zone is defined by

$$r(\theta^*)_\beta = r(0^\circ)_{\beta=90^\circ} = r_c = \text{constant} \tag{2.15}$$

where r_c is the radius of the core region. r_c is independent of angle β.

ii) For a ductile material, $r(\theta^*)_\beta$ is defined as the distance to the elastic-plastic boundary at some intermediate far field applied load $\sigma_{i,\beta}$, which is defined by

$$\sigma_{i,\beta} = \sigma_{i,\beta=90^\circ} = \text{constant}. \tag{2.16}$$

At this load, the local plasticity zone is assumed to cease expanding with further increase of far field load. The distance $r(\theta^*)_\beta$ is measured at an angle $(\theta^*)_\beta$ and is dependent on the angle β.

Theocaris and Philippinis (1987) further qualified that the formulation stated above is limited to small-scale yielding and proposed a modification to the T-criterion for large scale yielding using the HRR singularity field. For large scale yielding, the assumptions become:

i) Crack initiation occurs when the total strain energy density T equals or is greater than the critical value T_{cr} where T_{cr} is a material constant.

$$T = [(T_v + T_d)_{el} + (T_d)_{pl}]^\beta = [(T_v + T_d)_{el} + (T_d)_{pl}]^{\beta=\pi/2} \geq T_{cr}. \tag{2.17}$$

T is evaluated at a point r_o away and at an angle θ^* from the crack tip.

$$r_o = J_c/\sigma_y \tag{2.18}$$

where J_c is the value of the J integral at crack initiation for mode I fracture and σ_y is the yield stress under uniaxial conditions. $T_{v,el}$ is the elastic dilational strain energy density, $T_{d,el}$ is the elastic distortional strain energy density, $T_{d,pl}$ is the

plastic distortional strain energy density. The plastic dilational strain energy is zero due to the assumption that the plastic deformation is isochoric.

ii) The crack will propagate in the direction of the maximum elastic dilational strain energy density where $T_{v,el}$ is evaluated along a contour of constant effective stress σ_{eq} where $\sigma_{eq}^2 = \frac{3}{2} S_{ij} S_{ij}$ and S_{ij} is the deviatoric stress tensor.

2.3.1.3 Distortional Strain Energy Density Criterion

Two versions of distortional strain energy density criteria have been proposed by Jayatilaka et al. (1977) and Yehia (1991). Both criteria deal only with small-scale yielding and brittle fracture. Letting $(dW/dV)_T$ be the total strain energy density, $(dW/dV)_d$ the distortional strain energy, $(dW/dV)_v$ the dilational strain energy density and r the radius from the crack tip, these two criteria can be summarized as follows:

In the proposal by Jayatilaka et al.,

i) The direction of the crack growth coincides with the direction where $(dW/dV)_d$, which is evaluated along a contour with a constant r, is a minimum. A cut-off point for r is introduced because the strain energy density becomes singular as r tends to zero.

ii) Crack growth occurs when $(dW/dV)_T$, corresponding to the minimum $(dW/dV)_d$, is greater than or equal to a critical value.

Using the singular stress field (K-field), the above two conditions are shown to be equivalent to

i) $\frac{dS_d}{d\theta} = 0$ and $\frac{d^2S_d}{d\theta^2} > 0$ at $\theta = \theta^*$, and (2.19)

ii) $S \geq S_c$ at $\theta = \theta^*$ for crack growth to occur (2.20)

where $S = (dW/dV)_T / r$, S_c is the critical value of S and $S_d = (dW/dV)_d / r$. In Yehia's approach, for a crack in an infinite plane plate, the criterion postulates that the crack will grow in the direction where the distance from the crack tip to the elastic-plastic boundary is a minimum. The elastic-plastic boundary can be defined by a physically and mathematically sound yield criteria. Using the singular stress field (K-field), the criterion is expressed as follows:

i) $$\frac{d}{d\theta}\left(\frac{dW}{dV}\right)_d = 0 \text{ and } \frac{d^2}{d\theta^2}\left(\frac{dW}{dV}\right)_d > 0 \text{ at } \theta = \theta^*. \quad (2.21)$$

$(dW/dV)_d$ is evaluated along a constant distance r_o from the crack tip and θ^* is the angle that coincides with the minimum $(dW/dV)_d$.

ii) $(dW/dV)_d \geq (dW/dV)_{d,0}$ at $\theta = \theta^*$ is required for the crack growth to occur where r_o and $(dW/dV)_{d,0}$ are defined as

$$r_o = \frac{K_I^2}{2\pi\sigma_y^2} \text{ for plane stress,} \quad (2.22)$$

$$r_o = \frac{K_{Ic}^2}{2\pi\sigma_y^2}(1-2\nu)^2 \text{ for plane strain, and} \quad (2.23)$$

$$\left(\frac{dW}{dV}\right)_{d,0} = \frac{\sigma_y^2}{6G}, \quad (2.24)$$

where ν is the Poisson's ratio, G is the shear modulus, σ_y is the uniaxial yield strength, K_I and K_{Ic} are the fracture toughness.

2.3.1.4 Maximum Tangential Strain Energy Density Criterion

Koo and Choy (1991) proposed a criterion using the tangential strain energy density for brittle fracture. The only difference between this criterion and the S-Criterion for brittle fracture is the strain energy density component used as the governing parameter. This criterion assumes:

i) The crack growth occurs along the direction θ^* where the tangential strain energy density (C) is a maximum. The tangential strain energy factor is evaluated along a contour of equal radial distance from the crack tip. It can be shown as

$$\frac{\partial C}{\partial \theta} = 0 \text{ and } \frac{\partial^2 C}{\partial \theta^2} < 0 \text{ at } \theta = \theta^* \quad (2.25)$$

where $C = W_\theta/r$ and $W_\theta = \frac{1}{2}\sigma_\theta\varepsilon_\theta$. W_θ is the tangential strain energy density, r is the radial distance from the crack tip, σ_θ is the tangential (circumferential) stress and ε_θ is the tangential strain.

ii) Crack growth occurs when the tangential strain energy factor reaches a critical value C_{cr} where

$$C_{cr} = \frac{(1-2\nu)K_{Ic}^2}{8G}, \tag{2.26}$$

ν is the Poisson's ratio, G is the shear modulus and K_{Ic} is the fracture toughness.

2.3.2 Ductile Fracture

Ductile fracture is a result of microvoid coalescence (see Figure 2.1). Microvoids start to nucleate at a certain stage of deformation. These voids then grow and coalesce. Rupture occurs when the voids join together to create a macrocrack. Bluhm and Morissey (1965) investigated this phenomenon by testing cylindrical tensile specimens. Void sizes greater than 0.001 inch were not detected until significant necking had occurred. The density of the voids was observed to increase with deformation. While the voids grow and coalesce, there is not a significant drop in the load carrying capacity of the specimen. The sudden drop in the capacity only happens when the specimen ruptures around the neck region. McClintock (1968) calculated the growth of circular and elliptical cylindrical holes in a plastic material. Failure was assumed to occur when the holes touched each other. Rice and Tracey (1969) studied the rate of growth of an isolated spherical void in infinite media. Both McClintock, and Rice and Tracey found that hydrostatic tension has an inverse effect on the strain at fracture. Hancock and Mackenzie (1976) also determined that σ_m/σ_{eq} has an inverse effect on the plastic fracture strain of their notched circular rod specimens (σ_m is the hydrostatic stress, $\sigma_{eq}^2 = \frac{3}{2}S_{ij}S_{ij}$ and S_{ij} is the deviatoric stress).

Various approaches have been proposed to model ductile fracture based on the observed physical process. These approaches utilize different parameters as the measure for fracture and are normally termed as the local damage approach. These parameters are the critical damage state in a continuum damage mechanics model, the critical void volume fraction, the critical void growth rate, the absorbed energy till fracture or other parameters that are integrated over the plastic strain.

2.3.2.1 Absorbed Strain Energy till Fracture

Gillemot (1976), Czoboly et al. (1982) and Matic et al. (1987) used the absorbed (critical) strain energy density $(dW/dV)_c$ till fracture as a measure of the fracture toughness. The material is assumed to be able to absorb the strain energy density up to a critical value before fracture occurs. The absorbed strain energy density consists of the plastic and elastic strain energy density, which includes the strain energy density loss in hysteresis loops. In his testing, Gillemot found that $(dW/dV)_c$ is almost constant for different loading conditions (tension, compression→tension and cyclic→tension). However, Matic et al. found $(dW/dV)_c$ to be dependent on loading type (proportional and non-proportional loading). More detailed study is required to determine the load path dependency of $(dW/dV)_c$. Gillemot and Czoboly et al. associate the critical strain energy density $(dW/dV)_c$ with the critical energy release rate G_c. Using $(dW/dV)_c$ for a material similar to that of Matic et al. (1987), Degiorgi et al. (1989) closely predicted the CMOD (crack mouth opening displacement) versus the load up to crack initiation, and the crack initiation load of a compact tension specimen.

2.3.2.2 Continuum Damage Mechanics

Lemaitre (1984, 1985) proposed using continuum damage mechanics to model ductile fracture. In this model, the effect of void and crack formation is reflected in the parameter D, which is a measure of the damage state. A value of zero for D represents no damage and a value of unity signifies complete damage. Local rupture occurs when D attains a critical value D_c. This indicates the complete loss of the local load carrying capability. The parameter D is the ratio of the effective resisting area lost over the gross area. The damage increases the effective stress experienced by the material.

$$D=\frac{S-\tilde{S}}{S}, \tag{2.27}$$

where S is the gross area and $\tilde{S}$ is the effective resisting area.

$$\tilde{\sigma}=\frac{\sigma}{1-D}, \tag{2.28}$$

σ is the nominal stress and $\tilde{\sigma}$ is the effective stress. As shown in Figure 2.5, the nominal stress is the average stress over the gross area including voids. The effective stress is the actual stress experienced by the material matrix. In the case of the effective stress, the cross-section area under consideration excludes the area occupied by voids. The material response at the macro level is thus softened by the parameter D. For example, the constitutive equations for isotropic damage are modified as follows:

$$\varepsilon = \frac{\sigma}{(1-D)E} \tag{2.29}$$

where E is the Young's modulus and ε is the strain.

$$\varepsilon^p = \left(\frac{\sigma}{(1-D)K}\right)^M \tag{2.30}$$

is the Ramberg-Osgood model where K and M are the material coefficient and ε^p is the plastic strain. Lemaitre (1992) illustrated how damage is incorporated in the associated flow rule and discussed different methods of measuring the damage state. For isotropic damage, the evolution of D is described by the potential for dissipation φ^*. The potential φ^* is a scalar function

$$\varphi^*(\dot{\varepsilon}^p, \dot{p}, y, q; \varepsilon^e, T, p, D), \tag{2.31}$$

where ' ˙ ' indicates the time rate of change,

ε^p and ε^e are the plastic and elastic strains respectively,

p is the equivalent accumulated plastic strain,

T is the temperature and q is the heat flux,

$$\dot{p} = \left(\frac{2}{3}\dot{\varepsilon}^p_{ij}\dot{\varepsilon}^p_{ij}\right)^{\frac{1}{2}}, \tag{2.32}$$

$$y = \frac{1}{2}\frac{dW_e}{dD} \text{ at constant } \sigma \text{ and } T. \tag{2.33}$$

The differential function $\frac{1}{2}\frac{dW_e}{dD}$ is called the damage strain energy release rate. W_e is the elastic strain energy density. For ductile fracture, the rate of change in D is given by

$$\dot{D} = \frac{d\varphi^*}{dy} \text{ if } p > p_D \tag{2.34}$$

where p_D is the plastic strain threshold below which no damage occurs. One of the damage rate expressions suggested by Lemaitre (1984) is

$$\dot{D} = \frac{y}{s}\dot{p} \tag{2.35}$$

with $\varphi^* = \frac{s}{2}\left(\frac{y}{s}\right)^2 \dot{p}$ where s is a temperature dependent material coefficient. y can also be written in terms of the equivalent stress σ_{eq}, and the hydrostatic stress σ_m, as follows:

$$y = \frac{\sigma_{eq}^2}{2E(1-D)^2}\left[\frac{2}{3}(1+\nu) + 3(1-2\nu)\left(\frac{\sigma_m}{\sigma_{eq}}\right)^2\right] \text{ with} \tag{2.36}$$

$$\sigma_{eq} = \left(\frac{3}{2}\left(\sigma_{ij} - \delta_{ij}\sigma_m\right)\left(\sigma_{ij} - \delta_{ij}\sigma_m\right)\right)^{\frac{1}{2}}, \tag{2.37}$$

ν is the Poisson's ratio and δ_{ij} is the Kronecker delta. The rate of change of D proposed by Lemaitre depends on stress triaxiality. The critical damage state D_c is a material constant. Lemaitre also discussed how continuum damage mechanics can be used to model brittle fracture, fatigue fracture, and anisotropic damage. Chow and Wang (1987a, b and 1988) develop an anisotropic theory of damage continuum mechanics and compared their numerical solution, using the anisotropic model, with the results of a center crack tensile specimen. However, they calibrated the model with only a single test specimen.

Based on the continuum damage mechanics model by Lemaitre, for Ramberg-Osgood hardening model, Tai and Yang (1987) proposed a damage limit V_{DC} for V_D where

$$V_D = \int_0^p f\left(\frac{\sigma_m}{\sigma_{eq}}\right)dP \quad \text{and} \quad f\left(\frac{\sigma_m}{\sigma_{eq}}\right) = \frac{2}{3}(1+\nu) + 3(1-2\nu)\left(\frac{\sigma_m}{\sigma_{eq}}\right)^2. \tag{2.38}$$

$$\dot{D} = DCf\left(\frac{\sigma_m}{\sigma_{eq}}\right)\dot{p}p^{\frac{2}{n}} \tag{2.39}$$

where C is a material constant and n is the hardening coefficient.

$$\ln\left(\frac{D}{D_o}\right) = Cf\left(\frac{\sigma_m}{\sigma_{eq}}\right)p \tag{2.40}$$

and D_o is the initial damage at a very small strain. Tai and Yang state that V_{DC} can be taken as a material constant and they also demonstrate how J_{Ic} is associated to $\ln(D_c/D_o)$ and V_{DC}.

Wang (1992a, b) proposed another damage limit W_{DC} that is shown to be more loading independent than the criterion by Tai and Yang (1987). The analytical solutions from this model are compared to test results for different triaxial states of stress. This model differs slightly from Lemaitre continuum damage mechanics in the definition of $\dot{D}$ and the plastic strain p.

$$p = \left(\frac{2}{3}\varepsilon_{ij}^{p}\varepsilon_{ij}^{p}\right)^{\frac{1}{2}} \qquad \text{and} \qquad \dot{p} = \left(\frac{2}{3}\dot{\varepsilon}_{ij}^{p}\dot{\varepsilon}_{ij}^{p}\right)^{\frac{1}{2}}. \tag{2.41}$$

$$\dot{D} = \left(\frac{y}{S}\right)\frac{(p_c - p)^{\alpha-1}}{p^{2N}}\dot{p} \tag{2.42}$$

with the relationship $\dfrac{\sigma_{eq}}{(1-D)} = Kp^{N}$ based on the Ramberg-Osgood hardening law, where K and N are constant, S is a temperature dependent material constant, α is a damage coefficient and p_c is the value of p associated with D_c.

$$W_D = \int_{p_o}^{p} \alpha f\left(\frac{\sigma_m}{\sigma_{eq}}\right)(p_c - p)^{\alpha-1}dp \tag{2.43}$$

which gives W_{DC} when $p = p_c$ and p_o is the initial p that is associated with D_o. In the continuum damage mechanics approaches reviewed, none of the proposals considers the volume change associated with the void growth observed in ductile fracture.

2.3.2.3 Void Volume Fraction Criteria

Gurson (1977a, b) proposed a constitutive model that takes into account the nucleation and growth of voids in ductile fracture. The plastic potential function involves the void volume fraction, the deviatoric stress S_{ij}, and the hydrostatic stress σ_m. Thus, in this model, there is a volume change associated with plastic deformation as a result of the void growth. The void volume fraction also comes directly out of the model. The basic

form of the plastic potential, modified by Tvergaard (1982), Tvergaard and Needleman (1984), and Sun et al. (1989) can be generalized as

$$\Phi = \frac{3S_{ij}S_{ij}}{2\sigma_M^2} + 2f^* q_1 \cosh\left(\frac{q_2\sigma_{kk}}{2\sigma_M}\right) - \{1 + (q_3 f^*)^2\} = 0. \tag{2.44}$$

f^* is a function of void volume fraction f. q_1, q_2 and q_3 are adjustable parameters. σ_M is assumed to depend on the effective plastic strain ε_M^p through a uniaxial true stress-natural strain curve.

$$\dot{\varepsilon}_M^p = \left(\frac{1}{E_t} - \frac{1}{E}\right)\dot{\sigma}_M, \tag{2.45}$$

$$\sigma_{ij}\dot{e}_{ij}^p = (1-f)\dot{\varepsilon}_M^p\sigma_M \tag{2.46}$$

and e_{ij}^p is the Lagrangian strain. E is Young's Modulus and E_t is the current tangent modulus.

$$\dot{e}_{ij}^p = \Lambda\frac{\partial\Phi}{\partial\sigma_{ij}} \tag{2.47}$$

where Λ is determined from the consistency equation. For $q_2 = 0$ and $q_1 = q_3$, local fracture occurs when $f^* = 1/q_1$. f^* is defined as

$$f^* = \begin{cases} f & \text{for } f \le f_c \\ f_c + K(f - f_c) & \text{for } f \ge f_c \end{cases} \tag{2.48}$$

where f_c is a critical void volume fraction. K is a parameter related to q_3, f_c and the void volume fraction at fracture f_F. The growth rate of the void volume fraction is divided into void growth and void nucleation.

$$\dot{f} = \dot{f}_{growth} + \dot{f}_{nucleation} \text{ with} \tag{2.49}$$

$$\dot{f}_{growth} = (1-f)\dot{e}_{kk}^p \text{ , and} \tag{2.50}$$

$$\dot{f}_{nucleation} = B(\dot{\sigma}_M + \dot{\sigma}_m) + D\dot{\varepsilon}_M^p. \tag{2.51}$$

For void formation controlled only by the strain. D is a function of ε_M^p and $B = 0$. Using the modified Gurson model, Tvergaard (1982) studied ductile fracture by cavity nucleation between larger periodic distributed cylindrical voids. Tvergaard and Needleman (1984) further carried out numerical analyses of the cup-cone fracture of a

round tensile bar using the modified Gurson model. Sun et al. (1989) compared the numerical solution using the modified model with the results from tests on compact tension (CT) specimens and notched round rods, and found the result to be good. However, Shi et al. (1991) in their tests on cracked specimens, found that void volume fraction at the onset of crack growth is not a material constant. It depends on the geometry constraint and stress triaxiality.

2.3.2.4 Other Damage Limits

Other forms of damage limits have been proposed. Norris et al. (1978) proposed a limit based on D_c. Fracture starts when D reaches D_c over the critical dimension r_c. D is defined as

$$D(t) = \int_0^t \frac{\dot{\varepsilon}^p_{eq} dt'}{1 - c\sigma_m(t')} \tag{2.52}$$

where $\varepsilon^p_{eq} = \left(\frac{2}{3}\varepsilon^p_{ij}\varepsilon^p_{ij}\right)^{\frac{1}{2}}$, c is a constant and σ_m is the hydrostatic (mean) stress.

Another limit is based on the critical void growth rate $(R/R_o)_c$. R is the average radius of the void and the R_o is the initial void size, which can be considered the size of the inclusion. Rupture is considered to have occurred if R/R_o exceeds $(R/R_o)_c$. In their tests, Shi et al. (1991) and Marini et al. (1985) found that the critical void growth rate can be considered independent of stress triaxiality as a first approximation. Sun et al. (1989) and Marini et al. (1985) have also implemented the criterion into a finite element model based on the void growth function by Rice and Tracey (1969). Their analytical solutions seem to agree with the test results on notched circular bars. The void growth function used is

$$\frac{dR}{R} = \alpha \exp\left(\frac{3}{2}\frac{\sigma_m}{\sigma_{eq}}\right) d\varepsilon_{eq} \tag{2.53}$$

where α is an increasing function of inclusion volume fraction, σ_m is the hydrostatic stress, σ_{eq} is the equivalent von Misés stress and ε_{eq} is the equivalent von Misés strain.

$$\ln\left(\frac{R}{R_o}\right)_c = \int_{\varepsilon_{eq}^d}^{\varepsilon_{eq}^f} \alpha \exp\left(\frac{3}{2}\frac{\sigma_m}{\sigma_{eq}}\right) d\varepsilon_{eq} \,. \tag{2.54}$$

ε_{eq}^f is the strain at fracture and ε_{eq}^d is the strain at nucleation.

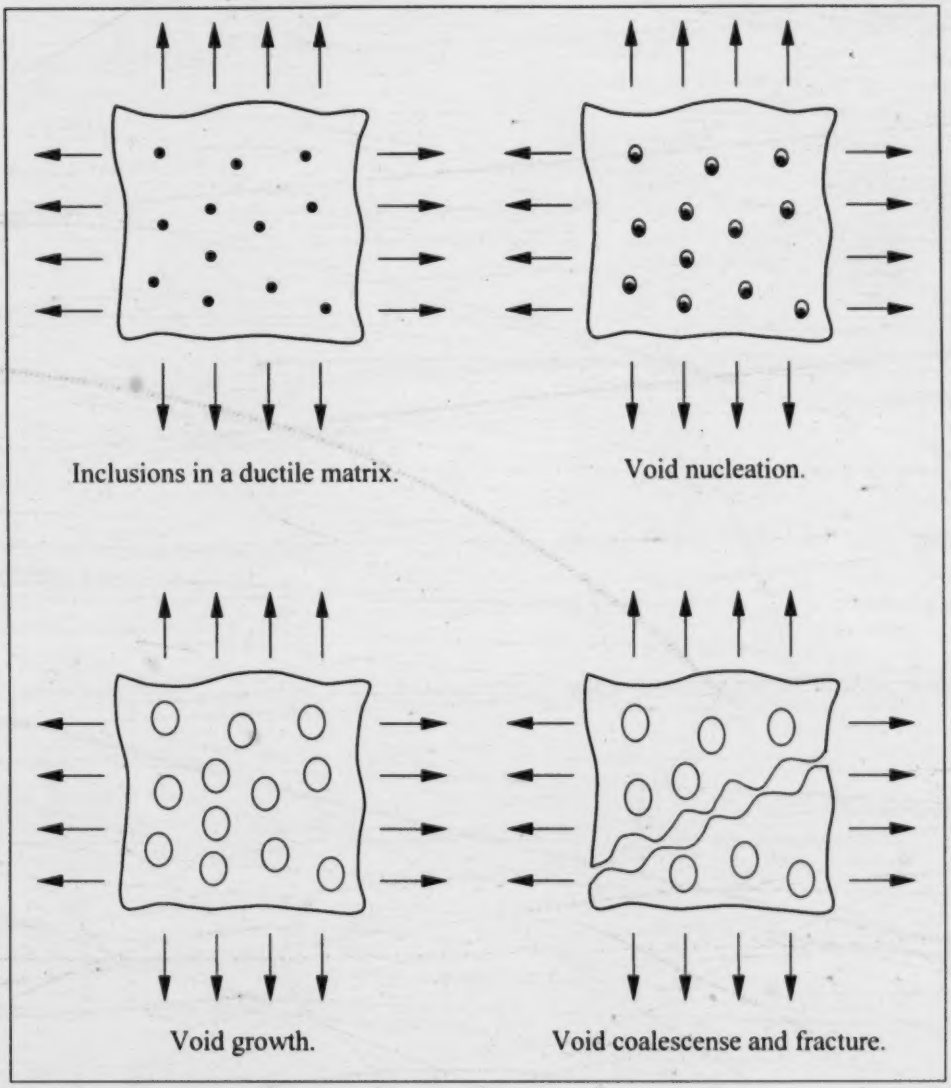

Figure 2.1 Mechanism of ductile fracture in metal.

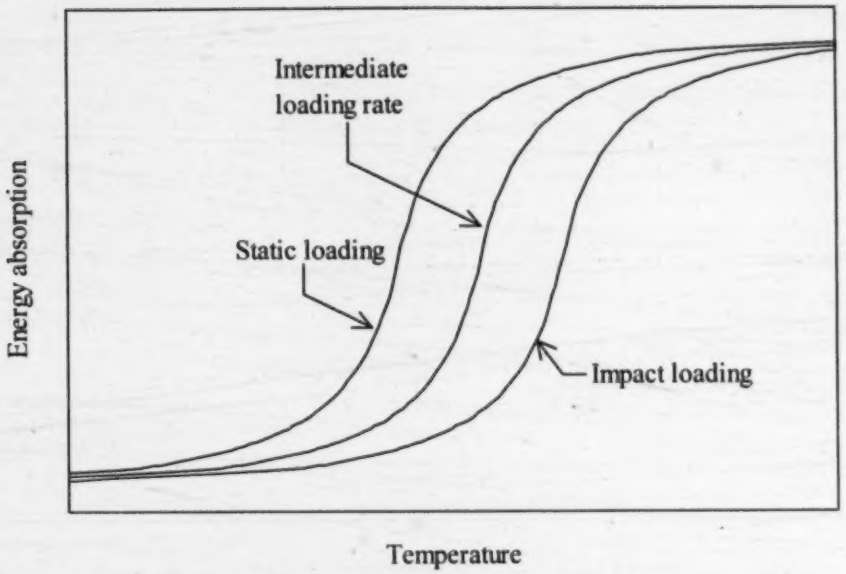

Figure 2.2 Typical relationship of the loading rate, temperature and level of energy absorption until fracture.

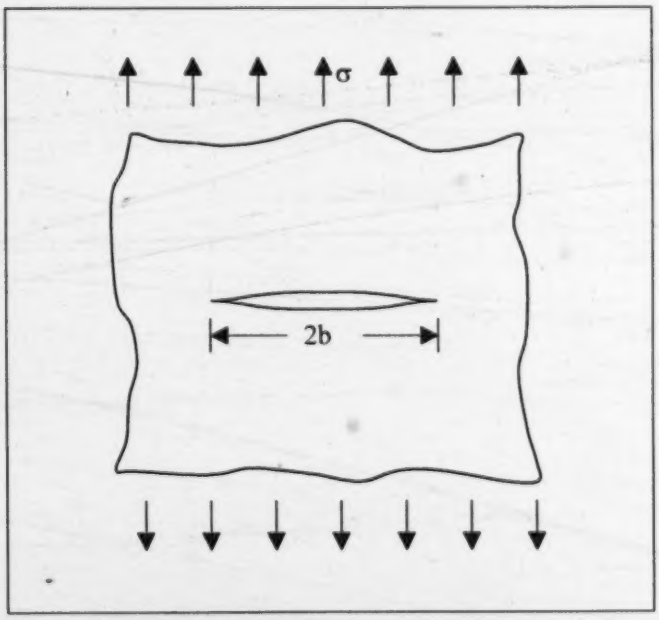

Figure 2.3 Through-thickness crack in an infinitely wide plate subjected to a remote tensile stress.

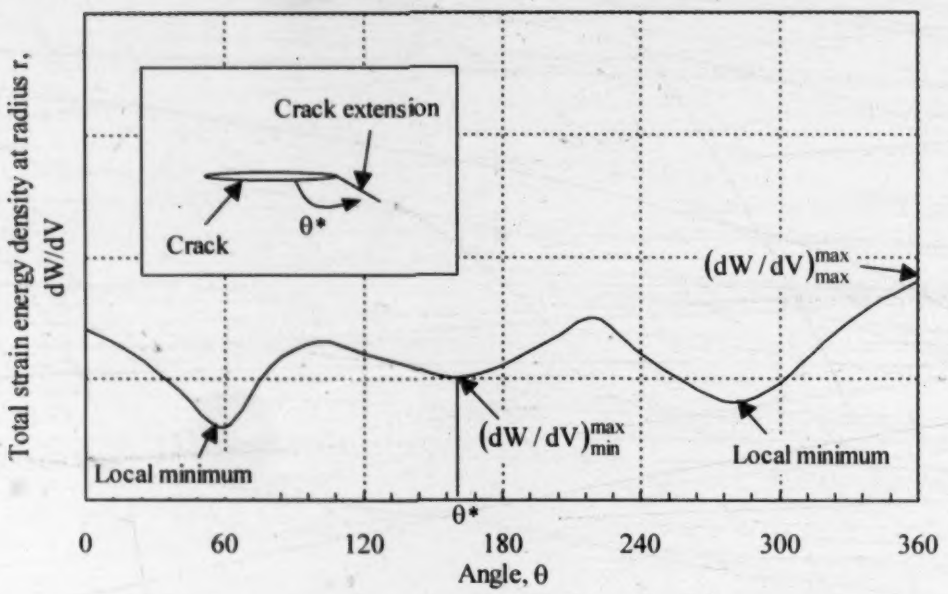

Figure 2.4 Sih's criterion, total strain energy density along the path at a distance r away from the crack tip.

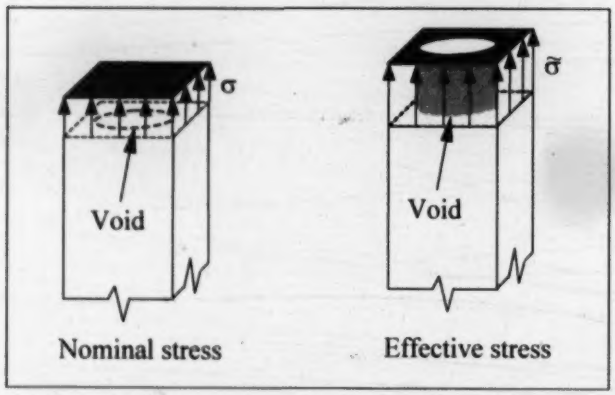

Figure 2.5 Nominal and effective stresses in continuum damage mechanics.

3 Proposed Model

The type of the fracture experienced by a steel specimen is affected by factors such as the hydrostatic tension, loading rate and temperature. Depending on these factors, the process of fracture can either be ductile or brittle. A constitutive model should take into account the effects these factors have on the material. As ductile fracture is the predominant mode of fracture experienced in using steel in structural engineering applications, a constitutive model is developed hereinafter to predict this mode of failure in steel structures.

3.1 Basis of the Model

McClintock (1968), Rice and Tracey (1969), Hancock and Mackenzie (1976) observed that hydrostatic tension has an inverse effect on the plastic fracture strain. Furthermore, the microvoid coalescence mode ductile fracture involves material dilation due to void growth. Thus, a constitutive model for ductile fracture of steel should take into account the effects of these phenomena. The continuum damage mechanics model proposed by Lemaitre (1984, 1985) considers the influence of hydrostatic tension on the plastic fracture strain. However, the model has no provision for material dilation due to void growth. A new model, which incorporates the plastic volume change, is developed based on continuum damage mechanics using the isotropic damage parameter proposed by Lemaitre. The model does not differentiate between damage due to void nucleation and damage due to void growth. For ductile material, the overall damage at fracture is caused mainly by void growth. Thus, both damage components are assumed to involve material dilation even though void nucleation does not result in any change in volume. The effect of the loading rate on fracture is also discounted in the model. Thus, only quasi-static loading can be applied with the model. Following Lemaitre's proposal, parameters associated with the isotropic damage evolution are temperature dependent.

The final process of ductile fracture is the coalescence of voids. This process involves the formation of a continuous fracture surface interconnecting large voids. In tension coupon tests conducted by Le Roy et al. (1981), Bluhm and Morissey (1965), Hancock and Mackenzie (1976), and Cox and Low (1974), the final process was found to be closely associated with a sudden drop in the load. But no single large series of

connected voids was detected until close to or beyond the sudden drop of the load. Cox and Low noticed that voids coalescence started at around 80% of the fracture strain, and the initial phase of the coalescence process involves connecting voids into a collection of short cracks. However, the initiation of the uncontrolled crack growth that coincides with the sudden drop of load only occurred when the collection of cracks joined together to form a single crack that was about 5 to 10% the diameter of the test specimen. Since void coalescence mainly involves connecting voids through the crack propagation, it should be influenced by the state of stress and the state of damage similar to the classical fracture mechanics theory. The stability of crack propagation also depends on other factors such as the specimen size, the relative stiffness of the testing machine and the test specimen, the loading rate and the dynamic effect of crack propagation.

In the proposed model, only the effects of the damage and stress states will be considered in triggering void coalescence. A simple relationship is established between the state of stress and the critical damage limit at which point fracture occurs. The treatment can be viewed in the context of linear elastic fracture mechanics where flaws are now replaced by voids or the state of damage. In linear elastic fracture mechanics, the required flaw size for attaining the stress intensity factor K for unstable crack propagation varies inversely with the stress level. Analogous to the flaw size, the critical state of damage for crack initiation and propagation is assumed to vary inversely with some measure of the state of stress. In addition, it is assumed that once a crack is initiated and voids start to coalesce, complete local fracture occurs instantly without any stable local crack propagation. In Lemaitre's model, the critical damage limit is assumed to be a material constant.

Other than the criterion by Chow and Wang (1987a, b and 1988), all the ductile fracture criteria reviewed in Chapter 2 have constant fracture limits that are independent of the stress state at the time fracture occurs. Most of these constitutive models do not consider material dilation due to void growth. Only the material models by Gurson (1977a, b) and the modified version by Tvergaard (1982) include the volume change due to void growth. However parameters for Gurson's or Tvergaard's material model are difficult to calibrate from a tension coupon test.

3.2 Physical Interpretation and Assumptions

In a damaged body, cracks and cavities reduce the effective area carrying stress. Referring to Figure 3.1, let S_g be the gross cross-section area, S_o the area of cracks and cavities, and S_e the effective area. The damage variable on a surface with the unit normal $\hat{n}_i$ can be defined as

$$D_i = \frac{S_g - S_e}{S_g} \tag{3.1}$$

where $S_g = S_e + S_o$. The undamaged state is given by $D = 0$, and the complete damaged state by $D = 1$. Fracture occurs when the damage variable reaches a critical value D_c, and in all cases it is less than unity. Under isotropic damage, cracks and cavities are assumed to be distributed uniformly in all directions, and the damage variable is orientation independent. Since the proposed model deals only with isotropic damage, the isotropic damage variable from this point on will be referred to as D without any reference to the direction. To account for void growth, the plastic volume increase in this model is coupled to the state of damage. The assumed relationship between voids and the state of damage is shown in Figure 3.2. Voids in the damaged body are assumed to be spherical and uniformly distributed in regions of constant damage. The surfaces of the cube depicted in the figure represent midpoints between voids.

3.3 Mathematical Formulation and Assumptions

Using the traditional elastic-plastic material model as a basis for the formulation, the total strain for the proposed constitutive model can be written as

$$\varepsilon_{ij} = \varepsilon_{ij}^{e} + \varepsilon_{ij}^{p} + \varepsilon_{ij}^{v} \tag{3.2}$$

where ε_{ij}^{e} is the elastic strain, ε_{ij}^{p} is the non-dilational plastic strain and ε_{ij}^{v} is the plastic volumetric strain due to the damage and void growth. The elastic strain is given by

$$\varepsilon_{ij}^{e} = \frac{1}{E(1-D)}\left[(1+\nu)\sigma_{ij} - \nu\sigma_{kk}\delta_{ij}\right], \tag{3.3}$$

and E is the elastic modulus, ν is Poisson's ratio and σ_{ij} is the Cauchy stress tensor. Non-dilational plastic strains (referred to as plastic strain henceforth) are assumed to follow the incremental flow theory of plasticity and the small change of ε_{ij}^{p} is defined as

$$d\varepsilon_{ij}^{p} = \frac{3d\varepsilon_{eq}^{p}\tilde{S}_{ij}}{2\tilde{\sigma}_{eq}} = \frac{3d\varepsilon_{eq}^{p}S_{ij}}{2\sigma_{eq}} \tag{3.4}$$

where a superposed ~ denotes the effective stresses with $\tilde{\sigma}_{ij} = \sigma_{ij}/(1-D)$, $\tilde{S}_{ij} = S_{ij}/(1-D)$ and $\tilde{\sigma}_{eq} = \sigma_{eq}/(1-D)$.

$$\sigma_{eq} = \left(\frac{3}{2}S_{ij}S_{ij}\right)^{1/2} = \left(\frac{3}{2}\left[\sigma_{ij}\sigma_{ij} - \frac{1}{3}\sigma_{pp}\sigma_{qq}\right]\right)^{1/2}. \tag{3.5}$$

$$\dot{\varepsilon}_{eq}^{p} = \left(\frac{2}{3}\dot{\varepsilon}_{ij}^{p}\dot{\varepsilon}_{ij}^{p}\right)^{1/2}. \tag{3.6}$$

S_{ij} is the deviatoric stress tensor, ε_{ij}^{p} is the plastic strain tensor and a superposed dot denotes the time rate of change. The equivalent effective stress $\tilde{\sigma}_{eq}$ is assumed to be a function of the equivalent plastic strain ε_{eq}^{p}.

The plastic volumetric strain and its relationship to the damage variable can be illustrated by referring to Figure 3.2. The smallest solid area is given by the cross-section at the mid-length of the cube. Assuming the voids are spherical and uniformly distributed, and the side dimension of the cube represents the spacing between voids, the damage variable can be written as

$$D = \frac{\pi r^2}{a^2}. \tag{3.7}$$

In the model, the material matrix undergoes no plastic volume change. Thus, the volume of the matrix in the undamaged and damaged states is the same. By taking the undamaged dimension of the cube as unity, the volume of the cube in the damaged state is as follows:

$$a^3 - \frac{4}{3}\pi r^3 = 1. \tag{3.8}$$

Substituting for r from (3.7) and rearranging (3.8), the volume of the cube can be written as

$$a^3 = \left(1 - \frac{4}{3}\sqrt{\frac{D^3}{\pi}}\right)^{-1} \quad \text{and} \tag{3.9}$$

$$\varepsilon^v_{kk} = \ln\left(a^3\right) \tag{3.10}$$

because the assumed undamaged volume is unity. Since the voids are assumed to spherical and uniformly distributed, the normal plastic volumetric strains are equal in all directions ($\varepsilon^v_{11} = \varepsilon^v_{22} = \varepsilon^v_{33}$) and the shear components are zero. Therefore, plastic volumetric strains can be written as $\varepsilon^v_{ij} = \varepsilon^v_{kk}\delta_{ij}/3$. Thus, the plastic volume change is related to the damage variable through

$$\varepsilon^v_{ij} = -\frac{1}{3}\ln\left(1 - \frac{4}{3}\sqrt{\frac{D^3}{\pi}}\right)\delta_{ij}. \tag{3.11}$$

The isotropic damage evolution for the proposed model is assumed to follow the form proposed by Lemaitre (1984, 1985). The change in the damage variable D is defined as

$$\dot{D} = \left(\frac{y}{s}\right)^n \dot{\varepsilon}^p_{eq} \tag{3.12}$$

where s and n are material and temperature dependent coefficients, y is the damage strain energy release rate

$$y = \frac{\sigma^2_{eq}}{2E(1-D)^2}\left[\frac{2}{3}(1+\nu) + 3(1-2\nu)\left(\frac{\sigma_h}{\sigma_{eq}}\right)^2\right], \tag{3.13}$$

σ_h is the hydrostatic stress

$$\sigma_h = \frac{1}{3}\sigma_{ii}. \tag{3.14}$$

Bridgman (1947) observed that the ductility of a steel specimen increases with the hydrostatic pressure. The steel specimen in Bridgman's test was able to neck almost to a point when sufficiently large hydrostatic pressure was applied. For this reason, it is assumed that there is no increase in the state of damage when the hydrostatic stress is negative. Similar to Lemaitre's proposal, damage is only initiated when the equivalent

plastic strain ε_{eq}^{p} exceeds a certain value. The change in the damage variable D is defined as

$$dD = \left(\frac{y}{s}\right)^{n} d\varepsilon_{eq}^{p} \text{ when } \varepsilon_{eq}^{p} > \varepsilon_{eq_c}^{p} \text{ and } \tilde{\sigma}_{ii} \geq 0, \text{ and} \tag{3.15}$$

$$dD = 0 \text{ when } \varepsilon_{eq}^{p} \leq \varepsilon_{eq_c}^{p} \text{ or } \tilde{\sigma}_{ii} < 0. \tag{3.16}$$

$\varepsilon_{eq_c}^{p}$ is the damage initiation equivalent plastic strain value below which no damage occurs, and it is a function of σ_h / σ_{eq}. Following Lemaitre, it is assumed that

$$\frac{\varepsilon_{eq_c}^{p}}{\varepsilon_{eq_f}^{p}} = \text{constant.} \tag{3.17}$$

In (3.17), the loading is such that σ_h / σ_{eq} is constant. The parameter $\varepsilon_{eq_f}^{p}$ is the equivalent plastic strain at fracture corresponding to D_c and constant σ_h / σ_{eq} loading.

In linear elastic fracture mechanics, the plane strain fracture toughness is significantly lower than the plane stress fracture toughness. The reduction in the fracture toughness (K_c) for plane strain conditions is attributed to the higher hydrostatic tension developed at the crack tip due to the plane strain constraint. As stated before, the steel specimen in Bridgman's test was able to neck almost to a point when sufficiently large hydrostatic pressure was applied. Thus, it is generally agreed that the hydrostatic tension stress has a great influence on the crack initiation and unstable crack propagation. With this in mind and together with the assumptions made in Section 3.1, a simple relationship is developed for the critical damage limit where

$$D_c = \frac{D_o}{(\sigma_h)^m} \leq 0.7854 \text{ when } \sigma_h > 0 \text{ and} \tag{3.18}$$

$$D_c = 0.7854 \text{ when } \sigma_h \leq 0. \tag{3.19}$$

D_o is a material constant that needs to be calibrated from the numerical simulation of the material test, the value of 0.7854 is the damage level at which two adjacent voids touch each other and m is a constant. For an infinitely wide plate with a single through crack subjected to a uniform tension stress, the mode I stress intensity factor is given by

$$K_I = \sigma\sqrt{\pi b} \tag{3.20}$$

where b is the flaw size and σ is the uniform stress. Rearranging (3.20) gives

$$b = \frac{K_I^2}{\pi(\sigma)^2} \text{ or } b_c = \frac{K_{Ic}^2}{\pi(\sigma)^2} \tag{3.21}$$

where b_c is the critical flaw size. Based on (3.21), the exponent m in (3.18) is assumed to be equal to 2. As a result, the relationship between the critical damage limit and the hydrostatic tension stress in (3.18) becomes

$$D_c = \frac{D_o}{(\sigma_h)^2}. \tag{3.22}$$

Compared to (3.21), D_c can be considered as the limit when fracture occurs analogous to the critical flaw size b_c, and D_o as an equivalent to the fracture toughness similar to K_{Ic}^2.

3.4 Summary of the Assumptions and Limitations for the Proposed Model

The assumptions and the limitations for the proposed model are listed below.

i) The effect of loading rate is not considered, thus the model is limited to quasi-static loading.

ii) Plastic strains are assumed to follow the incremental flow theory of plasticity and isotropic hardening. This works fine with monotonic loading. However, isotropic hardening does not capture the behaviour of steel very well in cyclic loading when the stress reversal is large.

iii) Damage is assumed to be isotropic and is a function of the state of stress and the plastic strain increment. Additional damage only occurs if the hydrostatic stress is positive and the damage initiation equivalent plastic strain $\varepsilon_{eq_c}^p$ is exceeded.

iv) The damage initiation equivalent plastic strain $\varepsilon_{eq_c}^p$ is function of σ_h / σ_{eq}.

v) Material dilation is assumed to vary with the state of damage. Voids due to damage are assumed to be spherical and uniformly distributed.

vi) Fracture is assumed to occur locally when the critical damage limit is reached. The damage limit is assumed to vary inversely to the square of the hydrostatic tension stress.

3.5 Numerical Implementation in ABAQUS

The finite element program ABAQUS (1997) was employed to evaluate and apply the proposed constitutive model. This computer program allows users to introduce their own material models in subroutines that are incorporated into the program. The program will call the subroutine for each material calculation point. At each iteration, the program passes to the subroutine, the information regarding the state of the material at the beginning of a time step including the strain increment for that step. In return, the subroutine passes back the information on the state of the material at the end of a time step. In addition, the subroutine must also supply the Jacobian matrix, $\partial\Delta\sigma/\partial\Delta\varepsilon$, for the constitutive model at the end of a time step, where $\Delta\sigma$ are the stress increments and $\Delta\varepsilon$ are the strain increments. In short, the program passes in σ^i, D^i, ε^i, $(\varepsilon^p_{eq})^i$, $(\varepsilon^p)^i$, $\Delta\varepsilon^i$, to the subroutine, and it passes back σ^{i+1}, D^{i+1}, ε^{i+1}, $(\varepsilon^p_{eq})^{i+1}$, $(\varepsilon^p)^{i+1}$, and $(\partial\Delta\sigma/\partial\Delta\varepsilon)^{i+1}$, where the superscripts i and i+1 denote the state of the material at the beginning of time steps i and i+1 respectively. Essentially, the subroutine is required to solve for either $\Delta\sigma$ in the form of (3.23) or $\Delta\tilde{\sigma}$ in (3.24).

$$\Delta\varepsilon^i = \left(\frac{\partial\varepsilon^e}{\partial\sigma} + \frac{\partial\varepsilon^p}{\partial\sigma} + \frac{\partial\varepsilon^v}{\partial\sigma}\right)\Delta\sigma^i \text{ or} \tag{3.23}$$

$$\Delta\varepsilon^i = \left(\frac{\partial\varepsilon^e}{\partial\tilde{\sigma}} + \frac{\partial\varepsilon^p}{\partial\tilde{\sigma}} + \frac{\partial\varepsilon^v}{\partial\tilde{\sigma}}\right)\Delta\tilde{\sigma}^i \tag{3.24}$$

where $\sigma^{i+1} = \sigma^i + \Delta\sigma^i$, $\tilde{\sigma}^{i+1} = \tilde{\sigma}^i + \Delta\tilde{\sigma}^i$ and $\tilde{\sigma}^{i+1} = \sigma^{i+1}/(1 - D^{i+1})$. Equations (3.23) and (3.24) are equivalent to $\Delta\varepsilon^i = (\Delta\varepsilon^e)^i + (\Delta\varepsilon^p)^i + (\Delta\varepsilon^v)^i$.

In the subroutine, the effective stress approach that utilizes (3.24) is used to search for the equilibrium condition at the end of a time step. This approach is simpler than one that solves for the Cauchy stress increments in the form of (3.23). The difference between the two approaches can be illustrated by rewriting (3.3) and (3.13) in terms of the effective stress. Rewritten, (3.3) and (3.13) respectively become

$$\varepsilon^e_{ij} = \frac{1}{E}\left[(1+\nu)\tilde{\sigma}_{ij} - \nu\tilde{\sigma}_{kk}\delta_{ij}\right] \text{ and} \tag{3.25}$$

$$y = \frac{\tilde{\sigma}_{eq}^2}{2E}\left[\frac{2}{3}(1+\nu) + 3(1-2\nu)\left(\frac{\tilde{\sigma}_h}{\tilde{\sigma}_{eq}}\right)^2\right]. \qquad (3.26)$$

Compared to (3.3) and (3.13), (3.25) and (3.26) are more compact, and are independent of the damage state D. The flow chart of the subroutine is shown on Figure 3.3.

3.5.1 Assumptions in the Numerical Implementation

In order to implement the model in the subroutine, some assumptions are made regarding the calculation process for certain parameters over a time step. These assumptions are as follows:

i) As defined in (3.15), the damage parameter increment is

$$dD = \left(\frac{y}{s}\right)^n d\varepsilon_{eq}^p .$$

Within a time step, y is assumed to vary linearly with ε_{eq}^p. It follows that

$$\Delta D^i = (s)^{-n} \int_0^{(\Delta\varepsilon_{eq}^p)^i} \left[y^i + (y^{i+1} - y^i)\frac{\varepsilon_{eq}^p}{(\Delta\varepsilon_{eq}^p)^i}\right]^n d\varepsilon_{eq}^p . \qquad (3.27)$$

Integrating (3.27) gives

$$\Delta D^i = \frac{1}{(n+1)s^n}\left[\frac{(y^{i+1})^{n+1} - (y^i)^{n+1}}{(y^{i+1} - y^i)}\right](\Delta\varepsilon_{eq}^p)^i . \qquad (3.28)$$

However, (3.28) exhibits a numerical singularity when y^{i+1} approaches y^i. The numerical singularity can be avoided by evaluating ΔD^i with a modified function of (3.28). The modified function is derived from (3.28) by taking the limit $y^{i+1} \to y^i$. It can be expressed as

$$\Delta D^i = \left(\frac{y^i}{s}\right)^n (\Delta\varepsilon_{eq}^p)^i = \left(\frac{y^{i+1} + y^i}{2s}\right)^n (\Delta\varepsilon_{eq}^p)^i . \qquad (3.29)$$

The changes in D and ε_{eq}^p within the time step i are denoted by ΔD^i and $(\Delta\varepsilon_{eq}^p)^i$ respectively. Thus, the change in the damage parameter D is calculated by either (3.28) or (3.29) depending on the difference between y^{i+1} and y^i. The value of y^i

is evaluated using the state of stress when the yield surface is first reached within a time step. The expressions (3.28) and (3.29) assume that the damage parameter D increases throughout the plastic deformation in a time step. This is true if the initial equivalent plastic strain $(\varepsilon_{eq}^{p})^{i}$ is greater than or equal to the damage initiation equivalent plastic strain $\varepsilon_{eq_c}^{p}$. In addition, the effective hydrostatic stress $\tilde{\sigma}_h$ is greater than or equal to zero throughout the plastic deformation. However, in some instances, $(\varepsilon_{eq}^{p})^{i}$ is less than $\varepsilon_{eq_c}^{p}$, but the final $(\varepsilon_{eq}^{p})^{i+1}$ is greater than $\varepsilon_{eq_c}^{p}$. For these situations, the variables y^{i} and $(\Delta\varepsilon_{eq}^{p})^{i}$ in (3.28) and (3.29) are scaled accordingly using the assumption that y varies linearly with ε_{eq}^{p}.

ii) In the constitutive model, the value of the damage initiation equivalent plastic strain $\varepsilon_{eq_c}^{p}$ is assumed to vary with the ratio σ_h/σ_{eq} according to (3.17). However the actual σ_h/σ_{eq} varies within a time step. Thus for the purpose of calculating $\varepsilon_{eq_c}^{p}$, σ_h/σ_{eq} is assumed to be constant within a time step. The value of σ_h/σ_{eq} used is based on the state of stress when the yield surface is first reached within a time step.

iii) Once damage is initiated, the damage parameter D is assumed to increase throughout the plastic deformation regardless of the relationship between $(\varepsilon_{eq}^{p})^{i}$ and $\varepsilon_{eq_c}^{p}$. However, the requirement for the effective hydrostatic stress $\tilde{\sigma}_h$ to be greater than or equal to zero still applies.

iv) Both assumptions (ii) and (iii) are redundant if $\varepsilon_{eq_c}^{p}$ is zero.

3.5.2 Formulation to Solve for $\Delta\tilde{\sigma}$ in a Time Step

Solving for $\Delta\tilde{\sigma}$ in a time step requires an iterative process except when the state of stress is in the elastic regime. Thus, Newton's method is used in the subroutine to find the new equilibrium state at the end of the time step. The rates of change of strain increments $\Delta\varepsilon$ with respect to the effective stress increments consist of three strain

increment components. As shown in (3.24), they are $\partial\Delta\varepsilon^e/\partial\Delta\tilde{\sigma}$, $\partial\Delta\varepsilon^p/\partial\Delta\tilde{\sigma}$ and $\partial\Delta\varepsilon^v/\partial\Delta\tilde{\sigma}$. With Newton's method, the tangent slope of the strain-stress curve is needed at each iterative cycle. The formulation for calculating the tangent slope for each strain component is listed below.

For the elastic strain component, rewriting (3.25) in terms of strain increments and effective stress increments gives

$$\Delta\varepsilon_{ij}^e = \frac{1}{E}\left[(1+\nu)(\tilde{\sigma}_{ij} + \Delta\tilde{\sigma}_{ij}) - \nu(\tilde{\sigma}_{kk} + \Delta\tilde{\sigma}_{kk})\delta_{ij}\right]. \tag{3.30}$$

Thus,

$$\frac{\partial\Delta\varepsilon_{ij}^e}{\partial\Delta\tilde{\sigma}_{mn}} = \frac{1}{E}\left[(1+\nu)\delta_{im}\delta_{jn} - \nu\delta_{mn}\delta_{ij}\right]. \tag{3.31}$$

Rewriting (3.4) in terms of plastic strain increments and effective stress increments gives

$$\Delta\varepsilon_{ij}^p = \frac{3\Delta\varepsilon_{eq}^p(\tilde{S}_{ij} + \Delta\tilde{S}_{ij})}{2(\tilde{\sigma}_{eq} + \Delta\tilde{\sigma}_{eq})}. \tag{3.32}$$

The rate of change of plastic strain increments with respect to effective stress increments can be written as

$$\frac{\partial\Delta\varepsilon_{ij}^p}{\partial\Delta\tilde{\sigma}_{mn}} = \frac{3(\tilde{S}_{ij} + \Delta\tilde{S}_{ij})}{2(\tilde{\sigma}_{eq} + \Delta\tilde{\sigma}_{eq})}\frac{d\Delta\varepsilon_{eq}^p}{d\Delta\tilde{\sigma}_{eq}}\frac{\partial\Delta\tilde{\sigma}_{eq}}{\partial\Delta\tilde{\sigma}_{mn}} - \frac{3\Delta\varepsilon_{eq}^p(\tilde{S}_{ij} + \Delta\tilde{S}_{ij})}{2(\tilde{\sigma}_{eq} + \Delta\tilde{\sigma}_{eq})^2}\frac{\partial\Delta\tilde{\sigma}_{eq}}{\partial\Delta\tilde{\sigma}_{mn}}$$

$$+ \frac{3\Delta\varepsilon_{eq}^p}{2(\tilde{\sigma}_{eq} + \Delta\tilde{\sigma}_{eq})}\frac{\partial\Delta\tilde{S}_{ij}}{\partial\Delta\tilde{\sigma}_{mn}}. \tag{3.33}$$

$\frac{d\Delta\varepsilon_{eq}^p}{d\Delta\tilde{\sigma}_{eq}}$ is the slope of the equivalent plastic strain versus the effective equivalent stress curve.

$$\frac{\partial\Delta\tilde{\sigma}_{eq}}{\partial\Delta\tilde{\sigma}_{mn}} = \frac{3(\tilde{S}_{mn} + \Delta\tilde{S}_{mn})}{2(\tilde{\sigma}_{eq} + \Delta\tilde{\sigma}_{eq})}. \tag{3.34}$$

$$\frac{\partial\Delta\tilde{S}_{ij}}{\partial\Delta\tilde{\sigma}_{mn}} = \delta_{im}\delta_{jn} - \frac{1}{3}\delta_{mn}\delta_{ij}. \tag{3.35}$$

The third and final component in (3.24) is the tangent slope for the plastic volumetric strain. Writing (3.11) in terms of the plastic volumetric strain increments and the change in damage parameter increment gives

$$\Delta\varepsilon_{ij}^{v} = \frac{1}{3}\left[\ln\left(1-\frac{4D^{3/2}}{3\pi^{1/2}}\right)-\ln\left(1-\frac{4(D+\Delta D)^{3/2}}{3\pi^{1/2}}\right)\right]\delta_{ij}. \tag{3.36}$$

The plastic volumetric strain rates are

$$\frac{\partial\Delta\varepsilon_{ij}^{v}}{\partial\Delta\tilde{\sigma}_{mn}} = \frac{2(D+\Delta D)^{1/2}}{3\pi^{1/2}-4(D+\Delta D)^{3/2}}\frac{\partial\Delta D}{\partial\Delta\tilde{\sigma}_{mn}}\delta_{ij}. \tag{3.37}$$

Depending on the difference between y^{i+1} and y^{i}, ΔD is evaluated using (3.28) or (3.29). In these two equations, only y^{i+1} changes with $\Delta\tilde{\sigma}$ whereas y^{i} is constant. Equations (3.28) and (3.29) can be summarized as

$$\Delta D^{i} = CST1 * HLD * (\Delta\varepsilon_{eq}^{p})^{i} \tag{3.38}$$

where $CST1 = \dfrac{1}{(n+1)s^{n}}$ for (3.28) and $\left(\dfrac{1}{2s}\right)^{n}$ for (3.29), and

$$HLD = \frac{(y^{i+1})^{n+1}-(y^{i})^{n+1}}{(y^{i+1}-y^{i})} \text{ for (3.28) and } (y^{i+1}+y^{i})^{n} \text{ for (3.29).}$$

Differentiating (3.38) with respect to $\Delta\tilde{\sigma}$ gives

$$\frac{\partial\Delta D^{i}}{\partial\Delta\tilde{\sigma}_{mn}} = CST1\left[(\Delta\varepsilon_{eq}^{p})^{i}\frac{\partial HLD}{\partial y^{i+1}}\frac{\partial y^{i+1}}{\partial\Delta\tilde{\sigma}_{mn}} + HLD\frac{\partial(\Delta\varepsilon_{eq}^{p})^{i}}{\partial\Delta\tilde{\sigma}_{mn}}\right] \tag{3.39}$$

$$\text{where } \frac{\partial HLD}{\partial y^{i+1}} = \frac{n(y^{i+1})^{n+1}+(y^{i})^{n+1}-(n+1)y^{i}(y^{i+1})^{n}}{(y^{i+1}-y^{i})^{2}} \text{ for (3.28), and} \tag{3.40}$$

$$= n(y^{i+1}+y^{i})^{n-1} \text{ for (3.29).} \tag{3.41}$$

From (3.26),

$$y^{i+1} = \frac{(\tilde{\sigma}_{eq}+\Delta\tilde{\sigma}_{eq})^{2}}{2E}\left[\frac{2}{3}(1+\nu)+3(1-2\nu)\left(\frac{\tilde{\sigma}_{h}+\Delta\tilde{\sigma}_{h}}{\tilde{\sigma}_{eq}+\Delta\tilde{\sigma}_{eq}}\right)^{2}\right]. \tag{3.42}$$

Thus,

$$\frac{\partial y^{i+1}}{\partial \Delta\tilde{\sigma}_{mn}} = \frac{1}{2E}\left[\frac{4}{3}(1+\nu)(\tilde{\sigma}_{eq} + \Delta\tilde{\sigma}_{eq})\frac{\partial \Delta\tilde{\sigma}_{eq}}{\partial \Delta\tilde{\sigma}_{mn}}\right.$$

$$\left. + 6(1-2\nu)(\tilde{\sigma}_{h} + \Delta\tilde{\sigma}_{h})\frac{\partial \Delta\tilde{\sigma}_{h}}{\partial \Delta\tilde{\sigma}_{mn}}\right] \text{ with} \tag{3.43}$$

$$\frac{\partial \Delta\tilde{\sigma}_{h}}{\partial \Delta\tilde{\sigma}_{mn}} = \frac{1}{3}\frac{\partial \Delta\tilde{\sigma}_{ii}}{\partial \Delta\tilde{\sigma}_{mn}} = \frac{1}{3}\delta_{mn}, \tag{3.44}$$

and $\frac{\partial \Delta\tilde{\sigma}_{eq}}{\partial \Delta\tilde{\sigma}_{mn}}$ is defined by (3.34). The other differential term in (3.39) can be expressed as

$$\frac{\partial \Delta\varepsilon^{p}_{eq}}{\partial \Delta\tilde{\sigma}_{mn}} = \frac{d\Delta\varepsilon^{p}_{eq}}{d\Delta\tilde{\sigma}_{eq}}\frac{\partial \Delta\tilde{\sigma}_{eq}}{\partial \Delta\tilde{\sigma}_{mn}} \tag{3.45}$$

where $\frac{d\Delta\varepsilon^{p}_{eq}}{d\Delta\tilde{\sigma}_{eq}}$ and $\frac{\partial \Delta\tilde{\sigma}_{eq}}{\partial \Delta\tilde{\sigma}_{mn}}$ are previously defined in (3.33).

3.5.3 Jacobian Matrix of the Constitutive Model

In addition to the state of material at the end of the time step, the subroutine is also required to pass back the Jacobian matrix of the constitutive model $(\partial\Delta\sigma/\partial\Delta\varepsilon)^{i+1}$. The Jacobian matrix is based on the Cauchy stress rather than the effective stress. To simplify the formulation, the Jacobian matrix is expanded from the tangent slope derivation for the strain increments with respect to the effective stress increments developed in Section 3.5.2. The formulation of the Jacobian matrix, $(\partial\Delta\sigma/\partial\Delta\varepsilon)^{i+1}$, is described below. In Section 3.5.2, the rate of change of strain increments with respect to the effective stress increments are shown to be

$$\frac{\partial \Delta\varepsilon}{\partial \Delta\tilde{\sigma}} = \frac{\partial \Delta\varepsilon^{e}}{\partial \Delta\tilde{\sigma}} + \frac{\partial \Delta\varepsilon^{p}}{\partial \Delta\tilde{\sigma}} + \frac{\partial \Delta\varepsilon^{v}}{\partial \Delta\tilde{\sigma}}. \tag{3.46}$$

Therefore in Cauchy stress form, (3.46) becomes

$$\frac{\partial \Delta\varepsilon}{\partial \Delta\sigma} = \left(\frac{\partial \Delta\varepsilon^{e}}{\partial \Delta\tilde{\sigma}} + \frac{\partial \Delta\varepsilon^{p}}{\partial \Delta\tilde{\sigma}} + \frac{\partial \Delta\varepsilon^{v}}{\partial \Delta\tilde{\sigma}}\right)\frac{\partial \Delta\tilde{\sigma}}{\partial \Delta\sigma} \text{ with} \tag{3.47}$$

$$\tilde{\sigma} + \Delta\tilde{\sigma} = \frac{\sigma + \Delta\sigma}{1 - D - \Delta D} \text{ and} \tag{3.48}$$

$$\frac{\partial \Delta\tilde{\sigma}}{\partial \Delta\sigma} = \frac{1}{1 - D - \Delta D} + \frac{(\sigma + \Delta\sigma)}{(1 - D - \Delta D)^2} \frac{\partial \Delta D}{\partial \Delta\sigma}. \tag{3.49}$$

The required Jacobian matrix is the inverse of (3.47), $(\partial\Delta\varepsilon/\partial\Delta\sigma)^{-1}$. In tensor form, (3.47) to (3.49) are

$$\frac{\partial \Delta\varepsilon_{ij}}{\partial \Delta\sigma_{kl}} = \left(\frac{\partial \Delta\varepsilon_{ij}^{e}}{\partial \Delta\tilde{\sigma}_{mn}} + \frac{\partial \Delta\varepsilon_{ij}^{p}}{\partial \Delta\tilde{\sigma}_{mn}} + \frac{\partial \Delta\varepsilon_{ij}^{v}}{\partial \Delta\tilde{\sigma}_{mn}} \right) \frac{\partial \Delta\tilde{\sigma}_{mn}}{\partial \Delta\sigma_{kl}}, \tag{3.50}$$

$$\tilde{\sigma}_{mn} + \Delta\tilde{\sigma}_{mn} = \frac{\sigma_{mn} + \Delta\sigma_{mn}}{1 - D - \Delta D}, \text{ and} \tag{3.51}$$

$$\frac{\partial \Delta\tilde{\sigma}_{mn}}{\partial \Delta\sigma_{kl}} = \frac{\delta_{mk}\delta_{nl}}{1 - D - \Delta D} + \frac{(\sigma_{mn} + \Delta\sigma_{mn})}{(1 - D - \Delta D)^2} \frac{\partial \Delta D}{\partial \Delta\sigma_{kl}} \tag{3.52}$$

$$= \frac{1}{1 - D - \Delta D} \left[\delta_{mk}\delta_{nl} + (\tilde{\sigma}_{mn} + \Delta\tilde{\sigma}_{mn}) \frac{\partial \Delta D}{\partial \Delta\sigma_{kl}} \right]. \tag{3.53}$$

Combining the first term of (3.50) with (3.53) and (3.31) gives the slope of elastic strain term as

$$\frac{\partial \Delta\varepsilon_{ij}^{e}}{\partial \Delta\sigma_{kl}} = \frac{1}{E(1 - D - \Delta D)} \Bigg((1 + \nu)\delta_{ik}\delta_{jl} - \nu\delta_{kl}\delta_{ij} + \left[(1 + \nu)(\tilde{\sigma}_{ij} + \Delta\tilde{\sigma}_{ij}) - \nu(\tilde{\sigma}_{pp} + \Delta\tilde{\sigma}_{pp})\delta_{ij} \right] \frac{\partial \Delta D}{\partial \Delta\sigma_{kl}} \Bigg). \tag{3.54}$$

For the plastic strain component, substituting (3.33), (3.34), (3.35) and (3.53) into the second term of (3.50) produces

$$\frac{\partial \Delta\varepsilon_{ij}^{p}}{\partial \Delta\sigma_{kl}} = \frac{1}{1 - D - \Delta D} \Bigg[\frac{9(\tilde{S}_{ij} + \Delta\tilde{S}_{ij})(\tilde{S}_{kl} + \Delta\tilde{S}_{kl})}{4(\tilde{\sigma}_{eq} + \Delta\tilde{\sigma}_{eq})^2} \left(\frac{d\Delta\varepsilon_{eq}^{p}}{d\Delta\tilde{\sigma}_{eq}} - \frac{\Delta\varepsilon_{eq}^{p}}{(\tilde{\sigma}_{eq} + \Delta\tilde{\sigma}_{eq})} \right) + \frac{3\Delta\varepsilon_{eq}^{p}}{2(\tilde{\sigma}_{eq} + \Delta\tilde{\sigma}_{eq})} \left(\delta_{ik}\delta_{jl} - \frac{1}{3}\delta_{kl}\delta_{ij} \right) + \frac{3}{2}(\tilde{S}_{ij} + \Delta\tilde{S}_{ij}) \frac{d\Delta\varepsilon_{eq}^{p}}{d\Delta\tilde{\sigma}_{eq}} \frac{\partial \Delta D}{\partial \Delta\sigma_{kl}} \Bigg]. \tag{3.55}$$

From (3.37) and (3.50), the plastic volumetric strain rate with respect to Cauchy stress can be expressed as

$$\frac{\partial \Delta \varepsilon_{ij}^{v}}{\partial \Delta \sigma_{kl}} = \frac{\partial \Delta \varepsilon_{ij}^{v}}{\partial \Delta \tilde{\sigma}_{mn}} \frac{\partial \Delta \tilde{\sigma}_{mn}}{\partial \Delta \sigma_{kl}} = \frac{2(D+\Delta D)^{1/2}}{3\pi^{1/2} - 4(D+\Delta D)^{3/2}} \frac{\partial \Delta D}{\partial \Delta \sigma_{kl}} \delta_{ij} \text{ with} \tag{3.56}$$

$$\frac{\partial \Delta D}{\partial \Delta \sigma_{kl}} = \frac{\partial \Delta D}{\partial \Delta \tilde{\sigma}_{mn}} \frac{\partial \Delta \tilde{\sigma}_{mn}}{\partial \Delta \sigma_{kl}}. \tag{3.57}$$

Substituting (3.53) into (3.57) gives

$$\frac{\partial \Delta D}{\partial \Delta \sigma_{kl}} = \frac{1}{1 - D - \Delta D} \frac{\partial \Delta D}{\partial \Delta \tilde{\sigma}_{mn}} \left[\delta_{mk} \delta_{nl} + (\tilde{\sigma}_{mn} + \Delta \tilde{\sigma}_{mn}) \frac{\partial \Delta D}{\partial \Delta \sigma_{kl}} \right]. \tag{3.58}$$

Rearranging (3.58), it becomes

$$\frac{\partial \Delta D}{\partial \Delta \sigma_{kl}} \left(1 - \frac{(\tilde{\sigma}_{mn} + \Delta \tilde{\sigma}_{mn})}{(1 - D - \Delta D)} \frac{\partial \Delta D}{\partial \Delta \tilde{\sigma}_{mn}} \right) = \frac{1}{(1 - D - \Delta D)} \frac{\partial \Delta D}{\partial \Delta \tilde{\sigma}_{mn}} \delta_{mk} \delta_{nl}. \tag{3.59}$$

Thus,

$$\frac{\partial \Delta D}{\partial \Delta \sigma_{kl}} = \frac{\dfrac{1}{(1 - D - \Delta D)} \dfrac{\partial \Delta D}{\partial \Delta \tilde{\sigma}_{kl}}}{1 - \dfrac{(\tilde{\sigma}_{mn} + \Delta \tilde{\sigma}_{mn})}{(1 - D - \Delta D)} \dfrac{\partial \Delta D}{\partial \Delta \tilde{\sigma}_{mn}}} \tag{3.60}$$

$$= \frac{\dfrac{\partial \Delta D}{\partial \Delta \tilde{\sigma}_{kl}}}{(1 - D - \Delta D) - (\tilde{\sigma}_{mn} + \Delta \tilde{\sigma}_{mn}) \dfrac{\partial \Delta D}{\partial \Delta \tilde{\sigma}_{mn}}}. \tag{3.61}$$

Substituting (3.60) into (3.56), gives the slope of plastic volumetric strain term as

$$\frac{\partial \Delta \varepsilon_{ij}^{v}}{\partial \Delta \sigma_{kl}} = \frac{\dfrac{2(D+\Delta D)^{1/2}}{3\pi^{1/2} - 4(D+\Delta D)^{3/2}} \dfrac{\partial \Delta D}{\partial \Delta \tilde{\sigma}_{kl}}}{(1 - D - \Delta D) - (\tilde{\sigma}_{mn} + \Delta \tilde{\sigma}_{mn}) \dfrac{\partial \Delta D}{\partial \Delta \tilde{\sigma}_{mn}}} \delta_{ij}. \tag{3.62}$$

The term $\partial \Delta D / \partial \Delta \tilde{\sigma}_{mn}$ is defined in (3.39).

3.5.4 Special Considerations

If damage grows within the time step, the hydrostatic stress at the end of the step has to be greater than or equal to zero by virtue of the assumption (3.15). Since

ABAQUS passes in the strain increments for a time step, this may result in a situation where there is no equilibrium state at the end of the time step that is able to simultaneously satisfy both (3.15) and either (3.28) or (3.29). If this situation occurs, and at some point within the time step the hydrostatic stress is greater than zero, the change in the damage parameter is limited to the amount that will not cause the hydrostatic stress to be negative at the end of a time step. This condition can occur in analyses that involve two-dimensional or three-dimensional stress-strain problems.

In order to safeguard against the situation described above, the initial elastic volumetric strain and the volumetric component of strain increment are first removed from the total strain. With the removal, the equilibrium hydrostatic stress for this new state of strain will always be zero at the end of this time step. The Newton's method using the tangent slope described in Section 3.5.2 is used to calculate the equilibrium state at the end of a time step for this new state of strain. However, the plastic volumetric strain contribution is excluded from the tangent slope. The total plastic volumetric strain increment is then calculated based on either (3.28) or (3.29), together with (3.36). If the total plastic volumetric strain increment is greater than the volumetric strain taken away, then the damage parameter increment is limited to the amount that corresponds to the volumetric strain removed. Otherwise, the calculation proceeds according to Section 3.5.2. However, for a three-dimensional stress-strain problem, a more efficient alternative for solving $\Delta\tilde{\sigma}^i$ is employed.

3.5.4.1 Procedure to Safeguard against Damage Growth with Hydrostatic Compression

The procedure to safeguard against the possibility of having damage growth under a hydrostatic compression state of stress is explained in this section. The total initial elastic volumetric strain and the volumetric component of strain increment is calculated as follows:

$$(\Delta\varepsilon^{tv})^i = \Delta\varepsilon^i_{pp} + (\varepsilon^e_{pp})^i \text{ with} \qquad (3.63)$$

p = 1, 2 for 2-D and

p = 1, 2, 3 for 3-D.

In the following formulation, the indices go from 1 to 2 for two-dimensional and 1 to 3 for three-dimensional stress-strain problems. The net strain increment after subtracting the initial elastic volumetric strain and the volumetric component of strain increments are

$$(\Delta\varepsilon_{ij}^{nt})^i = \Delta\varepsilon_{ij}^i - \frac{1}{B}(\Delta\varepsilon^{tv})^i \delta ij \text{ where} \tag{3.64}$$

B is 2 for 2-D and 3 for 3-D.

Removing the plastic volumetric strain component, (3.24) is reduced to

$$(\Delta\varepsilon^{nt})^i = \left(\frac{\partial\varepsilon^e}{\partial\tilde{\sigma}} + \frac{\partial\varepsilon^p}{\partial\tilde{\sigma}}\right)\Delta\tilde{\sigma}^i. \tag{3.65}$$

Solving (3.65) for $\Delta\tilde{\sigma}^i$ using Newton's method gives the state of stress at the end of the time step that has zero hydrostatic stress. Based on the new state of stress, the change in the damage parameter $(\Delta D^{tv})^i$ is calculated according to either (3.28) or (3.29). Using (3.36), $(\Delta D^{tv})^i$ translates into plastic volumetric strain increments of

$$(\Delta\varepsilon_{ij}^{ntv})^i = \frac{1}{3}\left[\ln\left(1 - \frac{4(D^i)^{3/2}}{3\pi^{1/2}}\right) - \ln\left(1 - \frac{4\left(D^i + (\Delta D^{tv})^i\right)^{3/2}}{3\pi^{1/2}}\right)\right]\delta_{ij}. \tag{3.66}$$

However if $(\Delta\varepsilon_{ij}^{ntv})^i$ is greater than $(\Delta\varepsilon^{tv})^i$, it implies that the change in damage of $(\Delta D^{tv})^i$ will result in negative hydrostatic stress at the end of the time step. Therefore, the change in plastic volumetric strain increments are limited by

$$(\Delta\varepsilon_{ij}^{v})^i \le \frac{1}{B}(\Delta\varepsilon^{tv})^i \delta ij. \tag{3.67}$$

Thus,

$$(\Delta\varepsilon_{ij}^{v})^i = \frac{1}{B}(\Delta\varepsilon^{tv})^i \delta ij \text{ when } (\Delta\varepsilon_{ij}^{ntv})^i > \frac{1}{B}(\Delta\varepsilon^{tv})^i. \tag{3.68}$$

Consequently, ΔD^i is calculated using $(\Delta\varepsilon_{ij}^{v})^i$ from (3.68). But if $(\Delta\varepsilon_{ij}^{ntv})^i$ is less than $(\Delta\varepsilon^{tv})^i$, it implies that a hydrostatic stress at the end of the time step that has to be greater than zero in order to achieve the change in damage of $(\Delta D^{tv})^i$. For this case, the solution scheme as described in Section 3.5.2 is used to solve for $\Delta\tilde{\sigma}^i$ in the form of (3.24):

$$\Delta\varepsilon^{i} = \left(\frac{\partial \varepsilon^{e}}{\partial \tilde{\sigma}} + \frac{\partial \varepsilon^{p}}{\partial \tilde{\sigma}} + \frac{\partial \varepsilon^{v}}{\partial \tilde{\sigma}} \right) \Delta\tilde{\sigma}^{i}.$$

3.5.4.2 Three-Dimensional Stress-Strain Problems

The alternate way for solving the effective stress increments in a three-dimensional stress-strain problem is discussed below. By applying (3.63) and (3.64) in three-dimensional stress-strain problems, the deviatoric strain and volumetric strain increments are completely uncoupled regardless of the actual hydrostatic stress. The deviatoric strain increments are represented by $(\Delta\varepsilon_{ij}^{nt})^{i}$ and the volumetric strain increments by $(\Delta\varepsilon^{tv})^{i}\delta_{ij}/3$.

For a three-dimensional stress-strain problem with hydrostatic tension at the end of the time step, the deviatoric and hydrostatic stress increments are solved independently. First, the procedure in Section 3.5.4.1 is used to calculate the change in deviatoric stresses. Once the effective deviatoric stresses are found, the change in hydrostatic stress, $\Delta\tilde{\sigma}_{h}^{i}$, is calculated to satisfy the conditions (3.69) and (3.70) as

$$(\Delta\varepsilon^{vt})^{i} = \left(\frac{\partial \varepsilon_{ij}^{e}}{\partial \tilde{\sigma}_{h}} + \frac{\partial \varepsilon_{ij}^{v}}{\partial \tilde{\sigma}_{h}} \right) \Delta\tilde{\sigma}_{h}^{i} \tag{3.69}$$

$$= (\Delta\varepsilon_{ii}^{e})^{i} + (\Delta\varepsilon_{ii}^{v})^{i}. \tag{3.70}$$

Newton's method is used to solve for $\Delta\tilde{\sigma}_{h}^{i}$. The following is the formulation of the tangent slope of the elastic and plastic volumetric strain increments with respect to the effective hydrostatic stress increment used in the iterative numerical scheme. By contracting the indices i and j, (3.3) becomes

$$\Delta\varepsilon_{ii}^{e} = \frac{(1-2\nu)}{E}(\tilde{\sigma}_{ii} + \Delta\tilde{\sigma}_{ii}) \text{ or} \tag{3.71}$$

$$= \frac{3(1-2\nu)}{E}(\tilde{\sigma}_{h} + \Delta\tilde{\sigma}_{h}). \tag{3.72}$$

Thus,

$$\frac{\partial \Delta\varepsilon_{ij}^{e}}{\partial \Delta\tilde{\sigma}_{h}} = \frac{3(1-2\nu)}{E}. \tag{3.73}$$

$(\Delta\varepsilon_{jj}^{v})$ is calculated according to (3.36) as

$$(\Delta\varepsilon_{jj}^{v}) = \ln\left(1-\frac{4D^{3/2}}{3\pi^{1/2}}\right) - \ln\left(1-\frac{4(D+\Delta D)^{3/2}}{3\pi^{1/2}}\right). \tag{3.74}$$

Differentiating (3.74) with respect to $\Delta\tilde{\sigma}_h$ gives

$$\frac{\partial(\Delta\varepsilon_{jj}^{v})}{\partial\Delta\tilde{\sigma}_h} = \frac{6(D+\Delta D)^{1/2}}{3\pi^{1/2}-4(D+\Delta D)^{3/2}}\frac{\partial\Delta D}{\partial\Delta\tilde{\sigma}_h}. \tag{3.75}$$

As a result, (3.39) can be written as

$$\frac{\partial\Delta D^{i}}{\partial\Delta\tilde{\sigma}_h} = CST1(\Delta\varepsilon_{eq}^{p})^{i}\frac{\partial HLD}{\partial y^{i+1}}\frac{\partial y^{i+1}}{\partial\Delta\tilde{\sigma}_h}. \tag{3.76}$$

From (3.42), y^{i+1} is defined as

$$y^{i+1} = \frac{(\tilde{\sigma}_{eq}+\Delta\tilde{\sigma}_{eq})^2}{2E}\left[\frac{2}{3}(1+\nu)+3(1-2\nu)\left(\frac{\tilde{\sigma}_h+\Delta\tilde{\sigma}_h}{\tilde{\sigma}_{eq}+\Delta\tilde{\sigma}_{eq}}\right)^2\right].$$

Differentiating y^{i+1} with respect to $\Delta\tilde{\sigma}_h$ gives

$$\frac{\partial y^{i+1}}{\partial\Delta\tilde{\sigma}_h} = \frac{3(1-2\nu)}{E}(\tilde{\sigma}_h+\Delta\tilde{\sigma}_h). \tag{3.77}$$

Consequently, (3.75) becomes

$$\frac{\partial\Delta D^{i}}{\partial\Delta\tilde{\sigma}_h} = CST1(\Delta\varepsilon_{eq}^{p})^{i}\frac{3(1-2\nu)}{E}\frac{\partial HLD}{\partial y^{i+1}}(\tilde{\sigma}_h+\Delta\tilde{\sigma}_h). \tag{3.78}$$

Finally, the effective stress increments are

$$\Delta\tilde{\sigma}_{ij} = \Delta\tilde{\sigma}_{ij}^{d} + \Delta\tilde{\sigma}_h\delta_{ij} \tag{3.79}$$

where $\Delta\tilde{\sigma}_{ij}^{d}$ is the deviatoric stress increment tensor.

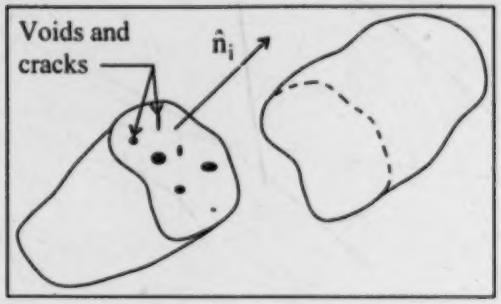

Figure 3.1 Cross-section surface of a damaged body in the $\hat{n}_i$ direction.

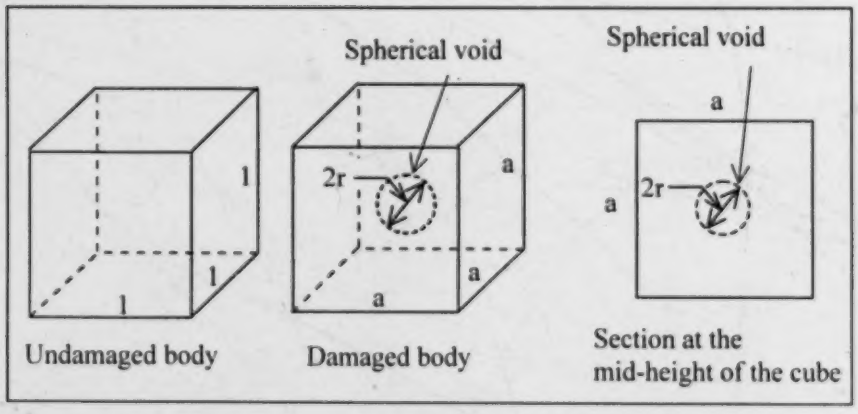

Figure 3.2 The assumed relationship of the void and the material matrix in a damaged body.

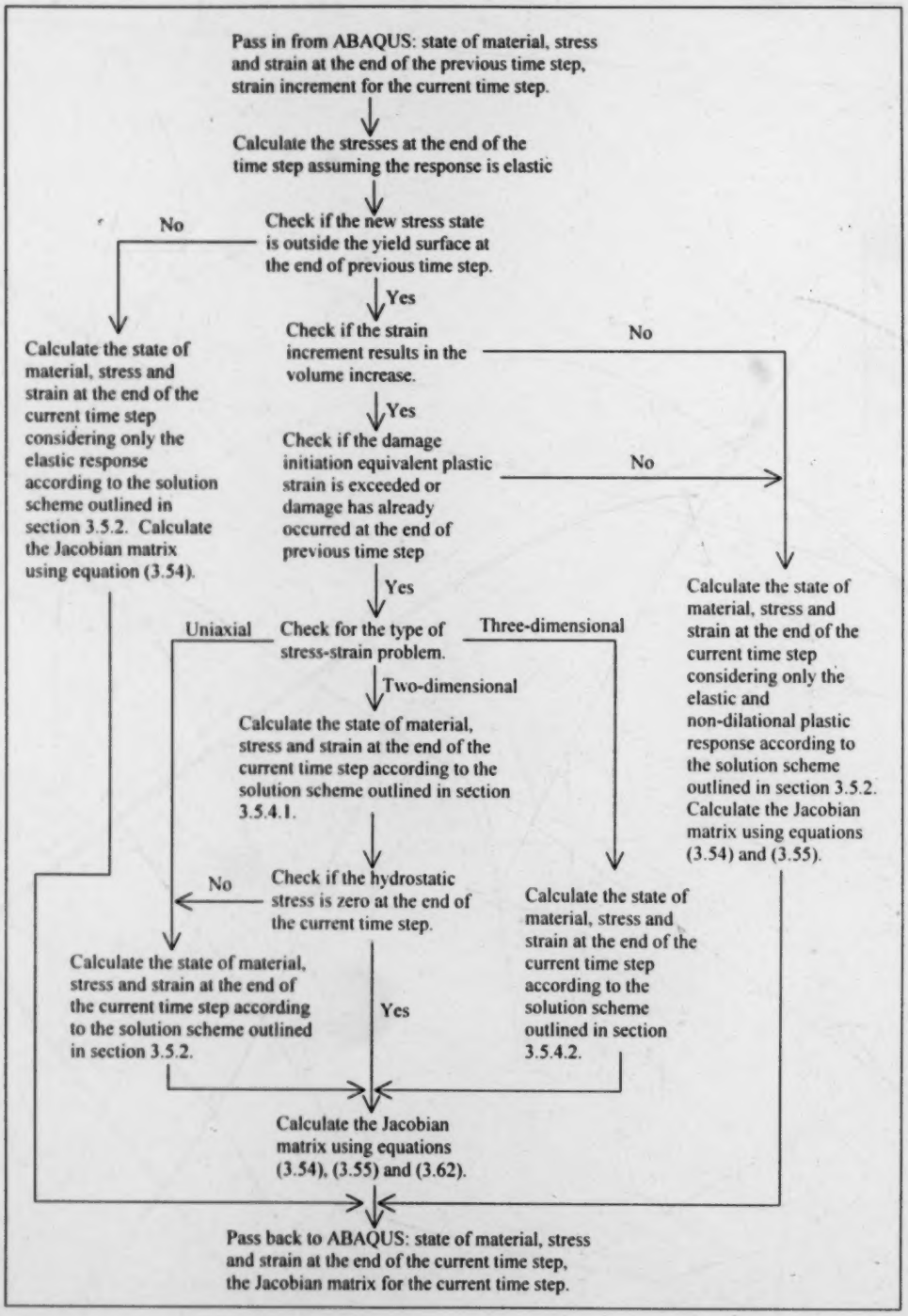
Pass in from ABAQUS: state of material, stress and strain at the end of the previous time step, strain increment for the current time step.
Calculate the stresses at the end of the time step assuming the response is elastic
Check if the new stress state is outside the yield surface at the end of previous time step.
No
Yes
Calculate the state of material, stress and strain at the end of the current time step considering only the elastic response according to the solution scheme outlined in section 3.5.2. Calculate the Jacobian matrix using equation (3.54).
Check if the strain increment results in the volume increase.
No
Yes
Check if the damage initiation equivalent plastic strain is exceeded or damage has already occurred at the end of previous time step
No
Yes
Calculate the state of material, stress and strain at the end of the current time step considering only the elastic and non-dilational plastic response according to the solution scheme outlined in section 3.5.2. Calculate the Jacobian matrix using equations (3.54) and (3.55).
Uniaxial
Check for the type of stress-strain problem.
Three-dimensional
Two-dimensional
Calculate the state of material, stress and strain at the end of the current time step according to the solution scheme outlined in section 3.5.4.1.
No
Check if the hydrostatic stress is zero at the end of the current time step.
Calculate the state of material, stress and strain at the end of the current time step according to the solution scheme outlined in section 3.5.2.
Yes
Calculate the state of material, stress and strain at the end of the current time step according to the solution scheme outlined in section 3.5.4.2.
Calculate the Jacobian matrix using equations (3.54), (3.55) and (3.62).
Pass back to ABAQUS: state of material, stress and strain at the end of the current time step, the Jacobian matrix for the current time step.

Figure 3.3 Flow chart for the subroutine.

4 Testing Program

In the previous chapter, a proposed constitutive model for ductile fracture of steel is presented. However, test data are required for the verification and study of the proposed model. For this reason, a test program was designed and carried out to acquire the necessary data. Specimens with different heat treatments and dimensions were used in order to obtain data from materials with inherently different ductility and from specimens experiencing different levels of hydrostatic tension stress. The testing program carried out is described in the following sections.

4.1 Objective

A test program involving a series of tension coupon specimens (see Figure 4.1) was conducted to obtain data for verifying the proposed constitutive model. Specimens with different heat treatments and dimensions were used in order to obtain test data from specimens with different ductility and levels of hydrostatic tension stresses. In order to study the constitutive model, numerical analyses were carried out to simulate and compare the load-deformation curves and the fracture of steel coupons. Data needed for the studies include the load, the longitudinal and radial deformations, and the deformed shape of the specimen. In addition, the constitutive model requires the effective true stress-true strain curve of the material in order to carry out the numerical analyses. In a tension coupon test, necking and strain localization start after the maximum load is reached. Thus, the effective true stress versus true plastic strain relationship can be calculated directly from the engineering stress versus engineering strain curve, up to the point of maximum load. The engineering stress versus engineering strain curve of a material can be measured using an extensometer during the test, up to the point of maximum load. Consequently, at least one of the test specimens for each heat treatment was designed to have a large enough gage length to accommodate an extensometer in the reduced section of the specimen.

4.2 Test Specimens

A total of sixteen specimens with three heat treatments were tested. All specimens were 22 mm in diameter with the diameter at the reduced section being either

10 mm or 14 mm. The transition radius of the specimen varies from 5 mm to 15 mm, and the gage length at the reduced section varies from 2 mm to 50 mm. The nominal dimensions of the test specimens are shown in Figure 4.1. However, the actual dimensions vary slightly from values listed in Figure 4.1. Although the transition from the 22 mm diameter section to the reduced section was specified to follow a circular arc, the actual profile of the machined specimen at the transition region turned out to be a spiral. Thus, in order to allow for an accurate numerical modeling of the specimen, the actual profile of the transition region was measured with a *Nikon Shadowgraph Model 6C*. This instrument measures the projected outline of the transition region in a two-dimensional plane, and it has an accuracy of one thousandth of an inch. For ease of numerical modeling and computing, cylindrical coupons were used instead of rectangular coupons, even though it is easier to machine a rectangular coupon from a rectangular strip.

Specimens were cut, heat-treated and machined from 457 x 457 x 25.4 mm thick ASTM A516 steel plates. Three heat treatments were used. Specimens made from the as supplied A516 steel without further heat treatment are grouped as one heat treatment and designated as "AS". The other two heat treatments involve either heating the same as supplied A516 steel to 900°C then annealing or heating to 1250°C and then normalizing. These are designated as "AN" and "NM" respectively. The steel plate was cut into 32 x 25.4 x 457 mm pieces for heat treatment. Using specimen AS1g6r5 as an example, the designation system is as follows: "AS" symbolizes the as supplied heat treatment, "1" denotes the specimen number for the same heat treatment and dimension, "g6" indicates the gage length is 6 mm and "r5" indicates the transition radius is 5 mm.

4.3 Test Set-up and Instrumentation

Measurements of load, deformation, and strain were made as the specimens were loaded. Strain gages were used to measure the initial elastic strain at the reduced section for specimens with the gage length G of 50 mm. Figure 4.2 shows measurements that were taken in the test. Due to interference of the loading head, deformations L1, L2 and L3 were measured with a divider. The divider opening was then measured with a caliper to obtain an indirect reading of the deformation. Diameters D1 through to D7 were

measured directly with a caliper. Diameter D4 is the measurement at the narrowest point on the specimen, in the necking region. In order to obtain the engineering stress versus engineering strain curve for each heat treatment, a 25 mm extensometer was used to measure the deformation at the reduced section for 50 mm gage length specimens. For other specimens, a 50 mm extensometer was placed outside the reduced section. Figure 4.3 shows the typical test set-up.

A digital camera (*Kodak DC120*) was positioned directly in front of the test specimen to photograph the deformed shape during the test. It was set on macro mode with manual focus, and was placed approximately 250 mm from the test specimen. The camera has a 1280 x 960 pixel resolution. From that distance, one pixel on the photo works out to 0.07 mm in actual dimension. In case there was a problem with the measured data, the photos would provide an alternate way of getting the data. As shown in Figure 4.4, the camera was placed on a swing arm so that it could be moved out of the way when the measurements were made. It was aligned and oriented so that the specimen was centered on the lens and in the same vertical line as the specimen. A plexiglas sheet with gridlines was attached to the specimen to assist in this endeavor. The gridlines were printed on a transparency, and then glued to the plexiglas. The spacing between the gridlines was measured with a *Leitz Wetzlar Large Universal Toolmakers Microscope Model UWM*, an apparatus that is accurate to one ten thousandth of an inch. Consequently, the gridlines can be used as reference dimensions if the desired deformation data are to be measured from the photos. The procedure used in positioning the camera is as follows.

1) First, the specimen was centered between the gridlines and on the same plane as the plexiglas attachment.
2) The camera was then positioned so that the gridlines were parallel to the edges of the photo; thus ensuring the focal plane of the camera is parallel to the plane of the plexiglas sheet.
3) Finally, the specimen was centered by moving the camera until the specimen showed up in the middle of the photo and vertical gridlines were approximately the same distance from both side edges.

Processes (2) and (3) were executed simultaneously. The final orientation and placement of the camera was achieved through trial and error. An example of the result of the positioning can be seen in Figure 4.5.

4.4 Test Procedure

Tests were carried out using an MTS 810 loading machine. All strain gage, stroke, extensometer, and load readings were routed through a data acquisition system. During the test, the load versus deformation response was constantly displayed on an x-y plotter. Stroke control was employed in all the tests. The specimen was tested until fracture with regular stoppages during the test, to take static readings and digital photographs of the deformed shape. All specimens were monotonically loaded with the exception of the AS2g50r5 and AS3g50r5 tests. During these tests, the specimens were unloaded and reloaded intermittently. Figure 4.6 shows the difference in the loading sequence for these tests. The magnitude of the unloading was about one-third the yield load. Together with the diameter D4 measurement, extensometer readings from the unloading and reloading provide a means to measure the change in the elastic modulus during the test.

Different loading rates were used depending on the gage length. A loading rate of 0.2 mm per minute was employed for specimens with gage length G less than 50 mm. For specimens with gage length equal to 50 mm, the loading rate was 0.5 mm per minute, and this rate was reduced to 0.25 mm per minute when the specimen was about to fracture. During the unloading and reloading of specimens AS2g50r5 and AS3g50r5, a loading rate of 0.25 mm per minute was used until the specimen had recovered the load level at the start of the unloading. The objective of the test program is to measure the static response of the specimens. Thus these rates were kept as low as possible to minimize the influence of the loading rate on the result, but not too low as to slow down the testing greatly. Furthermore, regular stoppages during the test for taking static readings also help in reducing the effect of the loading rate.

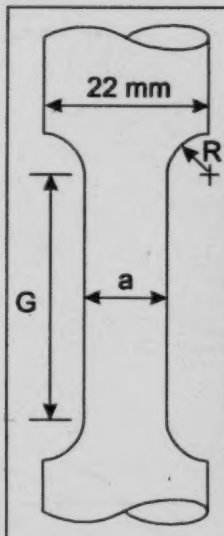

Specimen designation	Heat treatment Number of specimen			Nominal dimension (mm)		
	AS	AN	NM	a	G	R
xxng2r15	1	-	-	14	2	15
xxng2r5	1	1	1	14	2	5
xxng6r5	1	1	1	14	6	5
xxng12r5	1	1	1	14	12	5
xxng50r5	3	1	1	14	50	5
xxng50r7	1	-	-	10	50	7

Note: xxn - xx denotes the heat treatment and n denotes the specimen number for the same heat treatment and dimension.

Figure 4.1 Dimensions of test specimens.

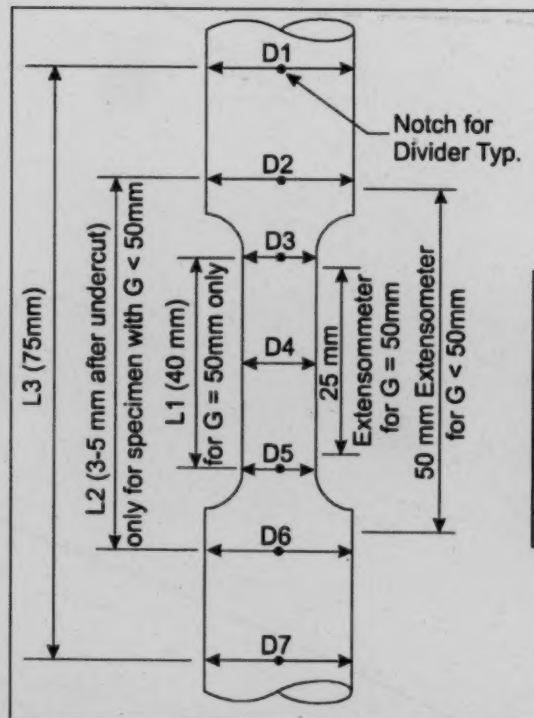

Specimen designation	Applicable measurement
xxng2r15	D1,D2,D4,D6,D7,L2,L3
xxng2r5	D1,D2,D4,D6,D7,L2,L3
xxng6r5	D1,D2,D4,D6,D7,L2,L3
xxng12r5	D1,D2,D4,D6,D7,L2,L3
xxng50r5	D1,D3,D4,D5,D7,L1,L3
xxng50r7	D1,D3,D4,D5,D7,L1,L3

Figure 4.2 Measurements taken in testing.

Figure 4.3 Test set-up.

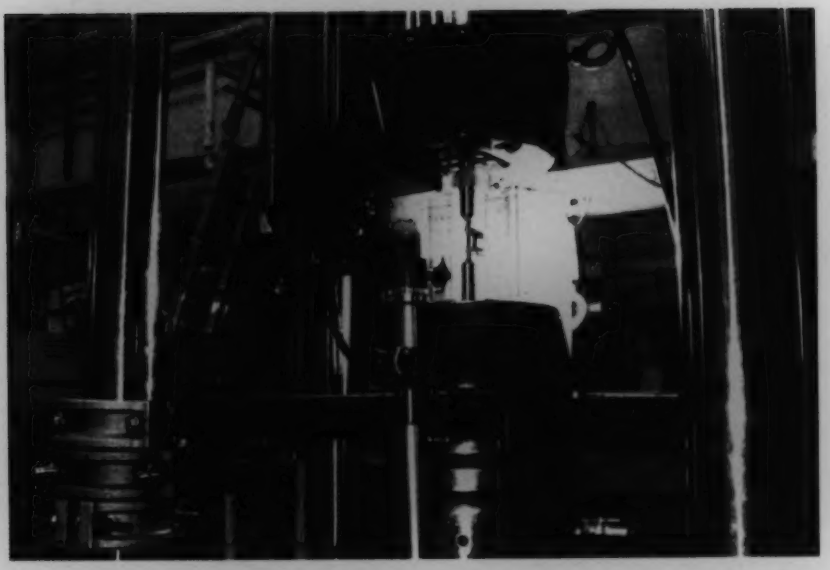

Figure 4.4 Attachment assembly for digital camera.

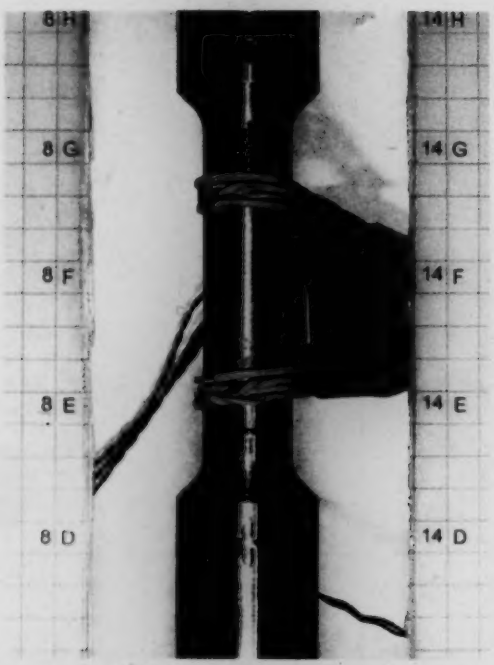

Figure 4.5 Positioning of digital camera.

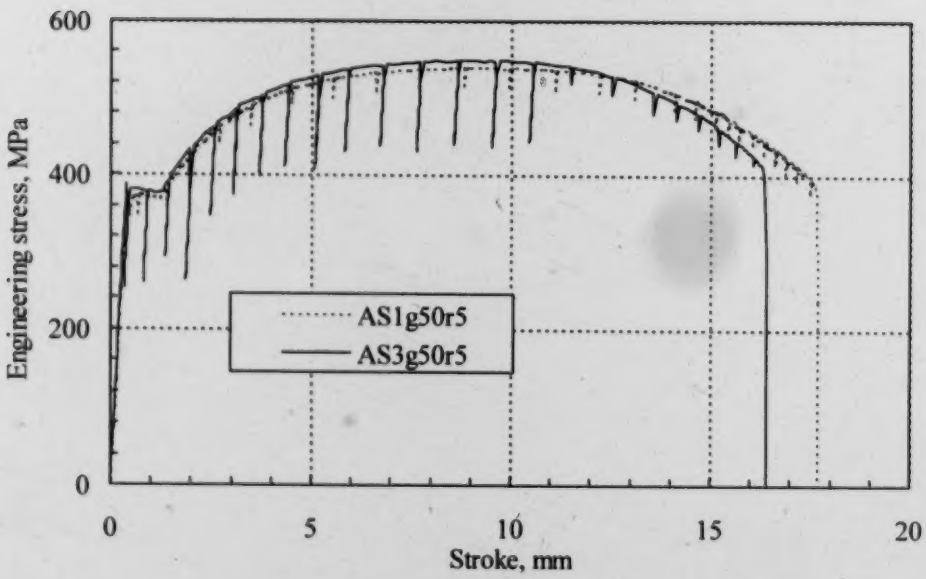

Figure 4.6 Typical loading sequence of monotonic, and load and unload test.

5 Analyses and Test Results

The proposed model is verified and studied using the test results. In this chapter, the test results are discussed and procedures for obtaining parameters to carry out the numerical analyses are described. Numerical solutions using the calibrated parameters are then compared to the measured results, and solutions from other material models.

5.1 Test Results and Discussions

The ductility of the specimen decreases as the gage length at the neck region or the transition radius, or both, are reduced. This is illustrated by the ratio of diameter D4 at fracture over the undeformed diameter, as shown in Table 5.1. The specimen with a greater ductility has a smaller ratio since the specimen is able to undergo greater deformation before fracture occurs. In the test, the peak stress also varies with the gage length and the transition radius. The value of the peak stress is an indirect indicator of the relative level of hydrostatic tension stress experienced by the specimen. A specimen experiencing a higher level of hydrostatic tension stress is able to attain a higher peak stress. Comparing the test results, it can be seen that the ductility varies inversely with the peak stress and the hydrostatic tension stress. Values in Table 5.1 and Figures 5.1 to 5.3 illustrate that the test program has achieved its objective of providing test data from materials with inherently different ductility and from specimens experiencing different levels of hydrostatic tension stress.

All specimens in the test program exhibited cup-cone type fracture surface except for NM1g2r5. For NM1g2r5, 95% of the fracture surface area is flat and shiny with the remaining 5% surface area being fibrous and dull. The portion of surface area that is fibrous and dull is at the centre of specimen. This indicates that there was not much void nucleation and growth taking place in NM1g2r5 before fracture occurred. For some specimens, fracture occurred while the crosshead displacement was on hold during the test when manual readings were taken. This illustrates the time dependent nature of the crack propagation. However as stated in Chapter 3, the dynamic effect is not considered in the proposed model.

Compared to specimens AS2g50r5 and AS3g50r5, which have undergone an unloading and reloading process, AS1g50r5 has a lower peak stress and a higher

ductility, although the difference is not big. This shows that frequent unloading and reloading has some effect on the ductility of a specimen even though the unloading is only one-third the yield load. This effect can also be seen in Figure 5.4.

Figure 5.5 shows that the apparent modulus of elasticity decreases as the deformation increases. This reduction may be due to the damage that occurred in the specimen. The apparent modulus of elasticity is obtained using the measured unloading and reloading strain, and the true stress. The true stress is calculated by dividing the load with the actual measured cross-section area.

Figures 5.6 to 5.9 show pictures of specimens at fracture. They clearly indicate that necking and fracture occurred at the mid-length of the reduced area region for specimens with gage length less than 50 mm. When the gage length is large, the stress is almost uniform along the reduced area region up to the initiation of necking. As a result, necking can start at any point along the gage length where there is any slight weakness in the material or any geometric imperfection. For these reasons, there was no definite fracture location for 50 mm gage length specimens, as shown in Figure 5.9.

5.2 Assessing the Measurement from Digital Camera

In the testing program, digital camera images are used as backup for the direct measurement data obtained using a caliper. Since the test data from the caliper measurement are satisfactory, no deformation result extracted from the photo image is used in the numerical analyses. Nevertheless, it is desirable to assess the suitability of the digital camera so it may be used in other tests or in other areas of study.

In order to assess the performance of the digital camera, the photo image data are compared to the caliper reading for the G2 and G3 extensions, and the D4 diameter change. The results from AS1g6r5 and AS1g12r5 are used in the assessment. Since the camera was swung back and forth during the test, the grid beside the specimen is used for calibrating the image to the actual dimension. From the position where the camera was set up, one pixel in the image represents roughly 0.07 mm in physical dimension of the specimen. Comparisons of the caliper and camera data are shown in Figures 5.10 to 5.12. The camera data agree very well with the caliper data. The maximum difference is only 0.24 mm, as indicated in Table 5.2. This is within four-pixel size of the image, and that

is about the best that can be expected from the camera used. The standard deviation of the difference is only 0.12 mm, which is less than two-pixel widths. With the small difference between photo image and caliper data, this demonstrates that the digital camera image can be a useful backup to the physical measurement.

5.3 Procedure for Obtaining Parameters for the Model

Parameters for the model are obtained through the numerical simulation of tension coupon tests. The effective true stress versus true plastic strain curve, and other parameters are adjusted until the numerical analysis is able to reproduce the engineering stress versus deformation curve of a tension coupon test. The deformation measurement can either be the longitudinal extension over a specific length or the radial contraction of a specimen at the necking location. Since the radial contraction provides a better representation of the local strain than the longitudinal extension, the engineering stress versus radial contraction values are thus used in the calibration. The numerical simulation procedure is based on the approach used by Matic et al. (1987). The procedure for obtaining the effective true stress versus true plastic strain curve is illustrated below. In the following, the loading direction is assigned as '1', and directions transverse to the load as '2' and '3'.

In uniaxial loading, $\varepsilon^p_{eq} = \varepsilon^p_{11}$ and $\sigma_{eq} = \sigma_{11}$. This condition exists in the neck region of a 50 mm gage length specimen until the peak load is reached and before the initiation of necking. Using (3.2) to (3.16) in Chapter 3, the following relationships between the various strain components can be established for a uniaxial loading condition.

$$\varepsilon_{11} = \varepsilon^e_{11} + \varepsilon^p_{11} + \varepsilon^v_{11}. \tag{5.1}$$

$$\varepsilon^e_{11} = \frac{\sigma_{11}}{E(1-D)}. \tag{5.2}$$

$$d\varepsilon^p_{11} = \frac{3d\varepsilon^p_{eq}\tilde{S}_{11}}{2\tilde{\sigma}_{eq}} = \frac{3d\varepsilon^p_{eq}S_{11}}{2\sigma_{eq}}. \tag{5.3}$$

$$\varepsilon_{11}^{v} = -\frac{1}{3}\ln\left(1-\frac{4}{3}\sqrt{\frac{D^3}{\pi}}\right). \tag{5.4}$$

$$dD = \left[\frac{\sigma_{11}^2}{2Es(1-D)^2}\right]^n d\varepsilon_{11}^{p}. \tag{5.5}$$

$$\varepsilon_{11}^{e} + \varepsilon_{11}^{p} + \varepsilon_{11}^{v} = \ln\left(1+\varepsilon_{11}^{E}\right) \tag{5.6}$$

and ε_{ij}^{E} is the engineering strain. The relationship between strains in the loading direction and the transverse direction can be expressed as

$$\varepsilon_{22}^{e} + \varepsilon_{33}^{e} = -2\nu\varepsilon_{11}^{e}, \tag{5.7}$$

$$\varepsilon_{22}^{p} + \varepsilon_{33}^{p} = -\varepsilon_{11}^{p} \text{ and} \tag{5.8}$$

$$\varepsilon_{22}^{v} + \varepsilon_{33}^{v} = 2\varepsilon_{11}^{v}. \tag{5.9}$$

Combining (5.7) to (5.9) gives

$$\varepsilon_{22}^{e} + \varepsilon_{33}^{e} + \varepsilon_{22}^{p} + \varepsilon_{33}^{p} + \varepsilon_{22}^{v} + \varepsilon_{33}^{v} = -2\nu\varepsilon_{11}^{e} - \varepsilon_{11}^{p} + 2\varepsilon_{11}^{v}. \tag{5.10}$$

Thus the ratio of the current transverse cross-section area to the undeformed cross-section area can be written in term of transverse strains as

$$\frac{A}{A_o} = \exp\left(\varepsilon_{22}^{e} + \varepsilon_{33}^{e} + \varepsilon_{22}^{p} + \varepsilon_{33}^{p} + \varepsilon_{22}^{v} + \varepsilon_{33}^{v}\right) \tag{5.11}$$

where A is the current transverse cross-section area and A_o is the undeformed cross-section area. In order to facilitate the calculation process in obtaining the effective true stress versus true plastic strain curve, the Poisson's ratio in (5.10) is assumed to be 0.5. This assumption does not introduce any notable error because the plastic strain component is dominant in situations where the strain is large. Thus, the term on the right side of (5.10) can be approximated as

$$-2\nu\varepsilon_{11}^{e} - \varepsilon_{11}^{p} + 2\varepsilon_{11}^{v} \approx -\varepsilon_{11}^{e} - \varepsilon_{11}^{p} + 2\varepsilon_{11}^{v}. \tag{5.12}$$

Combining (5.10) to (5.12) and engineering mechanics gives

$$\sigma_{11}^{E} = \sigma_{11}\exp\left(-\varepsilon_{11}^{p} - \varepsilon_{11}^{e} + 2\varepsilon_{11}^{v}\right) \tag{5.13}$$

and σ_{ij}^{E} the engineering stresses. Thus after selecting values for n, s and $\varepsilon_{eq_c}^{p}$, the ε_{eq}^{p} versus $\tilde{\sigma}_{eq}$ relationship is determined directly using the measured engineering stress versus engineering strain curve and (5.1) to (5.13). In the test, the engineering strain in the loading direction was measured with an extensometer, which only measures the average strain over a specific length. The strain reading using an extensometer is only equal to the local strain up to the point of the maximum load and before necking starts. Consequently, the extensometer strain can only be used to determine the ε_{eq}^{p} versus $\tilde{\sigma}_{eq}$ relationship up to the point of maximum load. By assuming the deformation is completely plastic, the local engineering strain beyond the peak load can be estimated using the change in the cross-section diameter as follows:

$$\varepsilon_{11}^{E} \approx \left(\frac{d_o}{d}\right)^2 - 1 \tag{5.14}$$

where d is the measured cross-section diameter and d_o is the undeformed cross-section diameter. Thus beyond the peak load, the ε_{eq}^{p} versus $\tilde{\sigma}_{eq}$ relationship is determined by using the estimated engineering stress and strain pairs. But this should only be extended down to approximately 95% of the peak load because the assumption of a uniaxial loading condition becomes invalid as necking develops. Occasionally, the estimated engineering stress and strain pairs have to be adjusted to give proper results. For the remainder of the curve, $\tilde{\sigma}_{eq}$ is assumed to vary linearly with ε_{eq}^{p}. The slope of the straight line, and the values of n, s and $\varepsilon_{eq_c}^{p}$ are then chosen by trial and error through the numerical simulation of the tension coupon test.

Observation by Le Roy et al. (1981), and Cox and Low (1974) showed that void nucleation starts at a low strain. The drop in the measured apparent elastic modulus as shown in Figure 5.5 also provides an indirect indication that damage may have started fairly early. For these reasons, the damage initiation equivalent plastic strain $\varepsilon_{eq_c}^{p}$ is assumed to be zero in all the numerical simulations.

Engineering stress versus engineering strain curves used in generating the ε_{eq}^{p} versus $\tilde{\sigma}_{eq}$ relationship for the test specimens are shown in Tables 5.3 to 5.5. As can be seen in Tables 5.3 and 5.4 for NM and AN heat treatments, the engineering strain data used are a combination of the measured extensometer strains up to the peak load and the estimated strains using (5.14). For NM and AN heat treatments, no adjustment is required for the estimated stress and strain pairs. But for AS heat treatment, Table 5.5 shows that the last two estimated engineering stress and strain pairs are modified to give a better result in the numerical simulation.

5.4 Numerical Analyses of Test Specimens

The proposed continuum damage mechanics constitutive model is incorporated into the finite element program ABAQUS (1997) to simulate the load-deformation behaviour and the fracture of the specimen. All numerical analyses are carried out using the axisymmetric element CAX8R and non-linear geometry option of ABAQUS. CAX8R is an eight-node biquadratic element with a reduced integration. The parameters and material properties n, s, $\varepsilon_{eq_c}^{p}$, and ε_{eq}^{p} versus $\tilde{\sigma}_{eq}$ relationship used in the numerical analyses are calibrated by trial and error to reproduce the load versus the change in diameter D4 curve of the 50 mm gage length specimen. Specimens used for the calibration are AS1g50r5, NM1g50r5 and AN1g50r5. As shall be seen in the subsequent sections, the load versus the change in diameter D4 curve can be reproduced by infinite choices of the parameter n. Thus, in addition to the load versus the change in the diameter curve, the most suitable value for n should also reproduce the load versus the change in the axial deformation curve of the test. This is done by matching the analytical axial deformation versus the change in the diameter curve to test results. Identical calibrated parameters and material properties are used in all numerical analyses for specimens from the same heat. In the analysis, the specimen is assumed to fracture instantaneously when the critical damage limit D_c is reached. Finite element meshes used in the numerical analyses are shown in Figures 5.13 to 5.18. In Appendix A, the mesh study for the refined region at the mid-length of the specimen shows that there is no significant difference in the result between the mesh in Figure 5.17 and the one that is

coarser. Thus the mesh scheme at the mid-length for Figure 5.17 is adopted for all specimens. All specimens are assumed to be axisymmetric and symmetric about the mid-length of the neck region. Thus only quarter of the specimen is modeled. Parameters and material properties are obtained according to the procedures as outlined in Section 5.3. Additional procedures established in Section 5.4.1 for AS heat treatment are also employed for all heat treatments.

5.4.1 AS Heat Treatment

Parameters and material properties used in the analyses were calibrated against the test results of AS1g50r5 and are shown in Table 5.6. Four numerical analyses were carried out for each specimen with values of n equal to 0.1, 0.5, 1.0 and 1.5. The analytical load versus change in diameter curves are plotted against the test results in Figures 5.19 to 5.24. These graphs show that the material model is able to closely predict the measured load versus change in diameter regardless of the value of n. However, when the load versus extensometer displacement from the finite element analyses are plotted in Figures 5.25 to 5.28, they exhibit that different values of n give a different load versus axial deformation relationship. But the overall appearance of the curve is not sensitive to a small variation of axial displacement due to the relative flatness of the curve over a wide range of the deformation. For this reason, the differences only show up at the tail end of the curves when the load starts to drop. A better illustration of the effect of n can be seen in radial versus axial deformation plots in Figures 5.29 to 5.32. Thus instead of trying to match the measured axial stress versus deformation curve, n is chosen to match the measured radial versus axial deformation of the test. Specimens with 50 mm gage length are not plotted for load versus axial deformation because the axial deformation for these specimens is sensitive to the geometric imperfection. This phenomenon is discussed in the subsequent section.

Thus, in order to select the most suitable n, measured radial versus axial deformation pairs for AS1g2r5, AS1g2r15, AS1g6r5 and AS1g12r5 specimens are compared to the analytical results for different n. Figures 5.29 to 5.32 are graphs of measured and predicted radial versus axial deformation curves. It can be seen in those figures that as n decreases, the slope of axial versus radial deformation curve increases.

This indirectly implies that lower n allows for greater volume expansion, and therefore greater overall damage. The following equation is used to measure the match between the measured and predicted axial versus radial deformation curve.

$$err = \frac{1}{k x_{max}^{test}} \sum_{i=1}^{k} \left| x_i^{anal} - x_i^{test} \right| \qquad (5.15)$$

where x_i^{anal} and x_i^{test} are the respective predicted and measured extensometer displacements at an identical radial deformation, x_{max}^{test} is the maximum measured extensometer displacement and k is the total measured radial versus axial deformation data pairs for each test specimen. Zero err implies a perfect match between the test and predicted results. Using (5.15), the calculated err for different test specimens and n are tabulated in Table 5.7. Summing err for all specimens and curve fit a third order polynomial through the results, the local minimum err on the polynomial is found to correspond to n equal to 0.571. Since analyses for n equal to 0.5 have already been carried out in the process of choosing n, for convenience 0.5 was selected as the n value to be used for AS specimens. Any choice of n in the range 0.5 and 0.6 should be fine because the differences between the results for n equal to 0.5 and 0.6 are small. Furthermore, there is also the uncertainty due to the measurement accuracy. For illustration, Figures 5.33 and 5.34 show that n = 0.5 provides a better fit to the measured radial versus extensometer deformation curve than n = 1.0.

The other parameter that needs to be calibrated from test results is the damage limit parameter D_o. The D_o value is chosen such that the absolute percentage error of the predicted and measured ratio of diameter D4 at fracture among all specimens is minimal. The selection is done by trial and error using the Goal Seek fuction in Microsoft EXCEL software. For D_o of 1.078×10^5 $(MPa)^2$, Table 5.8 shows that the model underestimates D4 at fracture for AS1g2r15 by 6% and overestimates the result for AS1g50r7 by 6%. Cox and Low (1974) in their tests noticed that the difference between the fracture strain and the strain at which the void coalescence was first detected was much smaller for a notched specimen than a smooth specimen. In relative terms, the notched specimen of Cox and Low can be considered as AS1g2r5 (short gage length) and the smooth specimen

as AS1g50r5 (long gage length). Thus the duration of the void coalescence process for AS1g50r5 would be longer than AS1g2r5. As stated in chapter 3, the proposed damage model does not attempt to capture the behaviour of the coalescence process. Based on the choice of D_o selected, the model is expected to under predict the ductility of long gage length specimens (50 mm gage length) and over predict the ductility of short gage length specimens (≤12 mm gage length). Thus, the error of the predicted fracture diameter for AS1g2r5 should be greater than AS1g2r15. But the values in Table 5.8 show the opposite. This may be due to the fact that the numerical analysis under predicts the peak stress of AS1g2r15 by 1.5% compared to 0.9% for AS1g2r5, as indicated in Table 5.10. The level of peak stress gives an indirect indication of the level of hydrostatic tension experienced by the specimen. Consequently, the hydrostatic tension stress in AS1g2r15 may actually be higher than predicted. Thus, the over prediction of the AS1g2r15 ductility is magnified due to the fact that the hydrostatic tension stress is under predicted. Looking at test results for short gage length specimens, they clearly show that any small change in the geometry has a great effect on the ductility and load behaviour. Taking into account the geometric sensitivity of the test results and the limitation of the fracture criterion in modeling the coalescence process, the maximum error of 6% for the predicted diameter at fracture can be considered to be quite good. For comparison, the predicted ratios of diameter D4 at fracture for a constant D_c are tabulated in Table 5.9. The maximum error for a constant D_c is 9%. However, regardless of the prediction of the diameter D4 at fracture, the predicted peak stress matches well with the measured stress. As can be seen in Table 5.10, all predicted and measured peak stresses are within 2%. Figures 5.35 and 5.36 compare the measured and predicted stress versus change in diameter curves with for $n = 0.5$ and $D_o = 1.078 \times 10^5 \text{ (MPa)}^2$. The analytical results closely match the measured values for all specimens even though the ε_{eq}^{p} versus $\tilde{\sigma}_{eq}$ relationship is calibrated from just a single test specimen.

Figure 5.37 shows the measured and predicted change in the apparent elastic modulus as the specimens were loaded. The drop in the measured apparent elastic modulus was much faster than the predicted one. One reason may be the fact that the proposed model assumes the effective elastic modulus does not change with deformation,

and any change in the apparent elastic modulus is caused by the nucleation and expansion of voids. But in actual fact, the effective elastic modulus may have decreased with deformation. The model may also under predict the damage in the specimen. But due to the difficulty in obtaining a reasonably accurate void count, no test was designed to measure the actual state of damage at different stages of loading.

5.4.2 AN Heat Treatment

Using similar procedures as for the AS heat treatment, the parameters and material properties used in the analyses for the AN treatment are calibrated against the test result of AN1g50r5. The parameters and material properties are shown in Table 5.11. Four numerical analyses are carried out for each specimen with values of n: 0.1, 0.5, 1.0 and 1.5. As can be seen in Figure 5.38, the graphs show that the material model is able to closely predict the measured load versus change in diameter regardless of the value of n. The same conclusion was reached for the AS heat treatment. Thus, the n that corresponds to zero err is the chosen value for the heat treatment. To illustrate the effect of n, plots of measured and predicted radial versus axial deformation for AN1g2r5 with different n are shown in Figure 5.39. Similar to the AS heat treatment, the 50 mm gage length specimen is excluded in the calculation for err. Values of err for various n and various specimens are tabulated in Table 5.12. The local minimum of err on the curve fit third order polynomial through the results corresponds to n = 0.581. Similar to AS heat treatment, n of 0.5 was selected as the parameter for the AN heat treatment. As shown respectively in Figures 5.40 and 5.41, the predicted radial versus axial deformation plots for n =0.5 provides a better fit to the measured values than n = 1.0.

Similarly, the D_o value is chosen such that the absolute percentage error of the predicted and measured ratio of diameter D4 at fracture among all specimens is minimal. For AN specimens, D_o is calibrated to be 7.78×10^5 $(MPa)^2$. Figure 5.42 shows the comparison of the predicted and measured NM specimens load versus deformation curve for n = 0.5 and $D_o = 7.78 \times 10^5$ $(MPa)^2$. Again, the material model is able to reproduce the load versus deformation curves of all test specimens even though the material properties are calibrated from just a single specimen. The predicted and measured diameters at fracture are listed in Table 5.13, and the maximum error is less than 4%. Similar to AS

heat treatment, the proposed fracture criterion under predicts the ductility of the 50 mm gage length specimen and over predict the ductility of 2 mm gage length specimen. For comparison, the maximum error doubled when D_c is assumed to be constant. The predicted diameters at fracture for a constant D_c are shown in Table 5.14. Table 5.15 also shows the good agreement between the predicted and measured peak stresses.

5.4.3 NM Heat Treatment

Four numerical analyses are carried out for each specimen with values of n equal to 0.5, 1.0, 1.5 and 2.0. Parameters and material properties used in the analyses are shown in Table 5.16. These parameters and material properties are calibrated against NM1g50r5. Figures 5.43 and 5.44 show the same characteristic as AS and AN specimens in term of the variation of load versus change in diameter and the radial versus axial deformation plots with respect to different n. For a short gage length specimen, there is a considerable stress concentration occurs at the neck region. Consequently, the damage at the neck region becomes more localized with a higher n, and the overall volume change due to damage is thus reduced. This is illustrated in Figure 5.44. As n becomes larger, the difference between the radial versus axial deformation curves gets smaller for different n. Using (5.15), the calculated values of err for different n are tabulated in Table 5.17. The local minimum of err on the curve fit third order polynomial through the results corresponds to n = 1.32. The differences bewteen the predicted results for n = 1.0 and n = 1.5 are small. Thus an n value of 1.5 is selected for analyses of all the NM specimens since analyses with n = 1.5 have already been carried out. Figures 5.45 and 5.46 show the radial versus axial deformation plots for n = 1.5 and n = 1.0. Even though n = 1.5 provides a better fit to the test data, it is difficult to discern that from plots alone.

For the NM heat treatment, the most suitable D_0 is 5.34×10^5 $(MPa)^2$. Bluhm and Morissey (1965) in their tests observed that as the strength of the material increases, the duration of stable void coalescence reduces. This may be partly due to the increase in relative stiffness of the test specimen to the test machine stiffness. The higher relative stiffness of a test specimen contributes to an earlier onset of unstable crack growth. Since the NM specimens have greater strength and less ductility than both the AS and AN

specimens, the range of error in the predicted fracture diameter is expected to be smaller due to a shorter duration of stable void coalescence. Table 5.18 shows that the maximum error is 3%. But discounting NM1g6r5, the difference in the error is only 1.3% among the other three specimens. As can be seen in Table 5.20, the peak stress for NM1g6r5 is under predicted by 1.8%. Similar to AS1g2r15, the over prediction of the NM1g6r5 ductility is magnified due to the under prediction of the hydrostatic tension. For comparison, the predicted fracture diameter for a constant D_c are tabulated in Table 5.19. Discounting NM1g6r5, the difference in the error for the predicted diameter at fracture with a constant D_c is 6%. Figure 5.47 compares the predicted and measured load versus deformation curves for NM specimens with $n = 1.5$ and $D_o = 5.34 \times 10^5$ $(MPa)^2$. In general, the proposed damage model gives a good prediction of the load deformation behaviour of the NM specimens.

5.4.4 Overall Results of Numerical Analyses

Overall, the proposed model is able to provide for all specimens, a good prediction of the load versus deformation behaviour and when fracture occurred. In order to compare the overall predicted shape of the specimens when close to fracture, the deformed finite element mesh is superimposed onto the digital photograph taken at the matching D4 diameter. Figures 5.48 to 5.50 show some of the comparisons for different heat treatments. The predicted deformed shape matches well with the actual specimen shape in the necking region. But in Figures 5.49 and 5.50, starting at the transition region of the specimen away from the neck area, the deformed mesh appears to have extended more than the actual specimen. The discrepancy is mainly due the optical effect caused by the positioning of the camera, the surface profile of the transition region and the shape of the specimen. As can be seen in Figure 4.51, there is disagreement even before any load is applied. This disagreement shows up in the photograph of an object with a concave surface profile, as in the case of the transition region.

The calculated values of the critical damage limit D_c for different specimens and heat treatments are summarized in Table 5.21. It shows that the value of D_c increases with the gage length and the ductility. A larger D_c allows for greater damage, and thus

greater ductility. All specimens have D_c greater than 0.16 except for NM1g2r5. As stated in Section 5.1, all specimens exhibited a cup-cone type fracture surface except for NM1g2r5 whose fracture surface is predominantly flat and shiny. This type of fracture surface is associated with a brittle mode of fracture. Thus, the type of fracture surface exhibited by NM1g2r5 is reflected in its rather low D_c as compared to other specimens.

Figures 5.52 to 5.57 show some of the contour plots of the damage state and the hydrostatic stress at close to fracture. In all cases, the numerical analyses predict that fracture is initiated from the axis of the specimen. Figures 5.58 and 5.59 clearly show that the effective hydrostatic tension at the centre of the specimen increases with the reduction in the gage length. This is consistent with the lower ductility observed in the shorter gage length specimens.

5.5 Sensitivity of the Axial Deformation to Geometric Imperfection

As mentioned in the previous section, the axial deformation of specimens with 50 mm gage length is very sensitive to any geometric imperfection. When the gage length is long, the stress is almost uniform throughout the reduced area region. This stress distribution exists up to the initiation of necking. Due to the stress uniformity in the reduced area region, necking can be triggered at any location due to its local geometric imperfection. Thus for a 50 mm gage length specimen, there is no specific location at which necking is expected. The actual location will depend on the imperfections. To demonstrate this phenomenon, AS1g50r5 is reanalyzed with different patterns of imperfection.

There are three patterns of imperfection considered. They are shown in Figure 5.60. Imperfect_1 has a full sine wave imperfection surface profile on half of the reduced area region. The amplitude of the imperfection is 0.04 mm or 0.3% of the specimen diameter. Imperfect_3 is the same as imperfect_2 except that the imperfection is duplicated for both half of the reduced area region. The last pattern is imperfect_2, which has amplitude of 0.04 mm for half of the reduced area region and 0.02 mm for the other half. The load versus deformation curves for all cases are plotted in Figures 5.61 and 5.62. It can be seen in Figure 5.61, the load versus radial deformation curves fall on top of each other. This indicates that the load versus radial deformation response of the

specimen is not sensitive to the geometric imperfection. However, the load versus axial deformation curves vary with the imperfection. In the case of imperfect_1, there is a distinct weak point in the specimen. Consequently, necking starts earlier than the perfect specimen. However, for imperfect_2 and imperfect_3, there are two weak points for necking to initiate. Necking occurs at two locations until one takes over, or a new necking develops and dominates. Thus depending on when a particular necking location starts to dominate, the descending portion of the load versus axial deformation curve may either be steeper or gentler than for a perfect specimen. As in Figure 5.62, the descending part of the load versus axial deformation curve for imperfect_3 is shallower than for the perfect specimen whereas that for imperfect_2 is steeper. Due to the geometric imperfection sensitivity of a load versus axial deformation curve, only the load versus radial deformation result is used for calibrating the parameters and material properties in the numerical analyses. The deformed meshes of all imperfection patterns are also shown in Figure 5.63. The location of necking varies with the pattern of the imperfection. This is part of the reason why necking does not occur at the same place for all 50 mm gage length specimens.

5.6 Comparison to Models by Matic et al. and Lemaitre

Only results from material models by Matic et al. (1987) and Lemaitre (1984, 1985) are compared to the proposed model because they require less effort to implement in the numerical analyses. The model by Matic et al. is an incremental plasticity model with fracture occurring when the total absorbed strain energy density reaches a critical limit. Lemaitre's model is similar to the proposed model except that it does not consider plastic volume change with damage and the critical damage limit D_c is constant. To carry out the comparison, numerical analyses for the AS specimens are performed using the models by Matic et al. and Lemaitre. The parameters and material properties used in the analyses are listed in Table 5.22.

Figures 5.64 and 5.65 show the load versus radial deformation plots of the three models without applying any fracture criterion. Since all parameters and material properties are calibrated from the load versus radial deformation curve, it is not surprising that all three models give good agreement to the test results. When the axial versus radial

deformation for the three models are plotted, models by Matic et al. and Lemaitre under predict the axial deformation since their models do not accommodate plastic volume change. This can be seen in Figures 5.66 and 5.67, and the tabulated values of err in Table 5.23. However the differences between results from three models are not big because damage is very localized as can be seen in Figures 5.52 and 5.54.

Using the same criterion to select the fracture limit as in Section 5.4, the predicted to measured ratio of diameter D4 at fracture for all three models are shown in Table 5.24. The maximum error from the proposed model is only 5.9%, as compared to 12% from the model by Lemaitre and 12.9% by Matic et al. The prediction by Matic et al. has the largest error because the absorbed strain energy density in a plastic deformation is independent of the hydrostatic stress. Thus the effect of hydrostatic tension is not taken into account in the fracture criterion by Matic et al. In Lemaitre's model, the critical damage limit is assumed to be constant. As a result, the error in the prediction is still rather high. Furthermore in the analysis, $n = 0.1$ is used for the Lemaitre model because it provides a better fit to the measured axial versus radial deformation curve than does a larger n. However, a smaller n reduces the influence of the hydrostatic stress on the damage rate. This is another reason why the maximum error for the diameter at fracture as predicted by Lemaitre's model is close to prediction by the Matic et al. model.

5.7 Obtaining Parameters and Material Properties in Practical Application

In the preceding sections, the parameters and material properties are obtained through calibration with test specimens of different gage length. Optimally, specimens with different gage length should be used to calibrate the parameters and material properties so the effect of hydrostatic stress can at least be quantified. However it is not always feasible to carry out different tension tests in practice. Even if tests with different gage lengths are carried out, it is difficult to measure the surface profile of the specimen accurately enough to provide a close numerical simulation. As illustrated in the test results, the load versus deformation response of a short gage length specimen is sensitive to the surface profile at both the transition and neck regions. However, the load versus radial deformation response for long gage length specimens, such as AS1g50r5 and AS1g50r7, does not vary much. Thus a standard ASTM round tension coupon test will

be an ideal choice for calibrating the effective true stress versus true strain curve. The choice of a round specimen is due to the ease and efficiency in the numerical simulation using an axisymmetric element rather a 3D solid element, which is required for a rectangular coupon. Due to the geometric imperfection sensitivity of the load versus axial deformation behaviour, as outlined in Section 5.5, the radial deformation should be measured in addition to the usual axial deformation.

In the numerical simulation of test specimens, the parameter n is calibrated from the short gage length specimens and the parameter D_o from all specimens. Based on the limited test results for the 50 mm gage length specimens, the parameter n is plotted against the ratio of cross-section area at fracture over the original area, A_f/A_o. The two marks on the graph in Figure 5.68 correspond to the result for NM1g50r5, and the average of AS1g50r5, AS1g50r7 and AN1g50r5 respectively. Unless the actual test using a short gage length specimen is carried out, the graph in Figure 5.68 may be used as a guide to select the parameter n. Since there are only two points available from the test result, the value of n is taken as 1.5 for A_f/A_o greater than 0.48, and n equal to 0.5 when A_f/A_o is less than 0.38. However caution should be exercised when using Figure 5.68 since it is based on a very limited data set. As mentioned in Chapter 3, the onset of unstable void coalescence and the duration of the stable void coalescence depend on many factors such as the specimen size, the relative stiffness of the testing machine and the test specimen, the loading rate and the dynamic effect of crack propagation. Due to the uncertainty and the complexity of the fracture process, D_o may be calibrated using the measured diameter (d_f) at fracture from a standard ASTM tension material test. However, to be conservative, 105% or 110% of d_f may be considered as the fracture diameter for calibrating D_o instead of the actual measured value because the duration of the stable void coalescence process is longer for a long gage length specimen than a short gage length specimen.

Table 5.1 Measured peak stress and diameter D4 at fracture.

Specimen	Peak stress MPa	Dia. D4 @ fracture over undeformed diameter	Specimen	Peak stress MPa	Dia. D4 @ fracture over undeformed diameter
AS1g2r5	638.5	0.787	NM1g2r5	732.5	0.847
AS1g2r15	578.4	0.749	NM1g6r5	650.4	0.813
AS1g6r5	572.8	0.716	NM1g12r5	602.6	0.707
AS1g12r5	537.9	0.680	NM1g50r5	583.6	0.688
AS1g50r5	516.6	0.616			
AS2g50r5	522.3	0.628	AN1g2r5	615.7	0.788
AS3g50r5	523.1	0.637	AN1g6r5	550.5	0.731
AS1g50r7	520.3	0.611	AN1g12r5	517.9	0.683
			AN1g50r5	494.5	0.627

Table 5.2 Comparison of camera and caliper data.

	Difference between camera and caliper reading, mm								
	G2 - extension			G3 - extension			D4 - diameter		
Specimen	Max.	Average	Standard deviation	Max.	Average	Standard deviation	Max.	Average	Standard deviation
AS1g6r5	0.16	0.06	0.09	0.16	-0.03	0.09	0.16	0.07	0.05
AS1g12r5	0.18	-0.02	0.09	0.24	-0.04	0.12	0.10	-0.01	0.06

Table 5.3 Engineering stress versus engineering strain used for NM heat treatment.

Measured for NM1g50r5			Used	
Extensometer strain, mm/mm	Estimated strain, $(d_o/d)^2$-1, mm/mm	Engineering stress, MPa	Strain, mm/mm	Engineering stress, MPa
0.00000	0.00000	4.44	0.00139	280.00
0.00495	0.00434	401.39	0.00495	401.39
0.01303	0.01164	454.88	0.01303	454.88
0.02788	0.02499	513.94	0.02788	513.94
0.04711	0.04474	549.93	0.04711	549.93
0.07013	0.06984	562.45	0.07013	562.45
0.09283	0.08926	580.08	0.09283	580.08
0.11381	0.11599	583.60	0.11599	583.60
0.13399	0.15976	583.46	0.15976	583.46
0.15214	0.21578	576.70		
0.16685	0.29915	567.29		
	0.39853	551.32		
	0.55912	531.37		
	0.62580	522.62		
	0.70325	512.81		
	0.77266	501.01		
	0.91716	483.25		
	1.01663	468.27		
	1.11515	443.90		

Table 5.4 Engineering stress versus engineering strain used for AN heat treatment.

Measured for AN1g50r5			Used	
Extensometer strain, mm/mm	Estimated strain, $(d_o/d)^2$-1, mm/mm	Engineering stress, MPa	Strain, mm/mm	Engineering stress, MPa
0.00000	0.00000	0.00		
0.00156	0.00000	340.95	0.00156	330.00
0.01247	0.00725	331.40	0.01247	331.40
0.02570	0.02799	344.06	0.02570	344.06
0.04201	0.04320	404.51	0.04201	404.51
0.06155	0.06348	440.30	0.06155	440.30
0.08583	0.09090	464.89	0.08583	464.89
0.11186	0.11940	480.33	0.11186	480.33
0.13848	0.14725	484.77	0.13848	484.77
0.18178	0.17800	490.21	0.18178	490.21
0.19824	0.22747	494.52	0.22747	494.52
0.23863	0.29489	491.40	0.29489	491.40
0.27453	0.37032	488.02		
0.31523	0.49647	474.83		
0.35881	0.67787	454.02		
0.44143	0.91334	428.63		
0.45675	1.04166	416.64		
	1.11959	408.15		
	1.23065	398.94		
	1.36634	388.07		
	1.50333	371.70		
	1.54382	359.60		

Table 5.5 Engineering stress versus engineering strain used for AS heat treatment.

Measured for AS1g50r5			Used	
Extensometer strain, mm/mm	Estimated strain, $(d_o/d)^2$-1, mm/mm	Engineering stress, MPa	Strain, mm/mm	Engineering stress, MPa
0.00000	0.00000	2.99	0.00163	350.00
0.00307	0.00000	347.98	0.00307	350.00
0.00759	0.00000	349.58	0.00759	350.00
0.02250	0.02054	360.21	0.02250	360.21
0.03089	0.03257	404.28	0.03089	404.28
0.04381	0.04790	443.04	0.04381	443.04
0.05764	0.05883	465.37	0.05764	465.37
0.07724	0.07960	493.69	0.07724	493.69
0.09750	0.09600	500.20	0.09750	500.20
0.11949	0.12130	509.31	0.11949	509.31
0.14253	0.14041	515.16	0.14253	515.16
0.16706	0.16728	516.62	0.16728	516.62
0.19330	0.19133	514.69	0.19133	514.69
0.22123	0.22982	510.97	0.22982	510.97
0.24809	0.33240	508.18	0.28000	506.00
0.26820	0.42350	501.07	0.40000	493.00
	0.56589	485.24		
	0.64829	475.94		
	0.75404	462.44		
	0.81961	453.54		
	0.90022	448.49		
	0.99444	439.18		
	1.09145	428.48		
	1.19103	417.18		
	1.29287	403.88		
	1.40198	394.98		
	1.57188	379.09		
	1.63872	370.00		

Table 5.6 Material properties and parameters used in the analyses for AS heat treatment.

Elastic modulus = 215000 MPa		Poisson's ratio = 0.3				$\varepsilon^{p}_{eq_c}$ = 0.0	
n = 0.1	s^{-n} = 0.33	n = 0.5	s^{-n} = 0.22	n = 1. 0	s^{-n} = 0.14	n = 1.5	s^{-n} = 0.09
True plastic strain, mm/mm	Effective true stress, MPa	True plastic strain, mm/mm	Effective true stress, MPa	True plastic strain, mm/mm	Effective true stress, MPa	True plastic strain, mm/mm	Effective true stress, MPa
0.00000	350	0.00000	350	0.00000	350	0.00000	350
0.00143	351	0.00143	351	0.00143	351	0.00143	351
0.00590	353	0.00592	353	0.00592	353	0.00592	353
0.02041	370	0.02050	369	0.02053	369	0.02054	368
0.02828	420	0.02843	418	0.02847	417	0.02848	417
0.04037	468	0.04062	465	0.04070	463	0.04072	463
0.05321	499	0.05358	496	0.05370	494	0.05374	493
0.07108	542	0.07163	537	0.07184	534	0.07190	533
0.08928	563	0.09004	556	0.09034	552	0.09043	551
0.10859	587	0.10959	579	0.11001	575	0.11015	572
0.12839	609	0.12966	600	0.13021	594	0.13040	592
0.14922	628	0.15078	617	0.15148	610	0.15173	607
0.16896	642	0.17080	630	0.17166	622	0.17198	618
0.19974	663	0.20206	649	0.20318	640	0.20362	635
0.23833	690	0.24128	674	0.24278	662	0.24338	656
0.32431	752	0.32879	730	0.33123	714	0.33231	705
0.35783	775	0.36293	749	0.36579	730	0.36710	719
4.00000	3282	4.00000	2820	4.00000	2435	4.00000	2163

Table 5.7 Calculated err for AS heat treatment.

Specimen	err			
	n = 0.1	n = 0.5	n = 1.0	n = 1.5
AS1g2r5	0.010194	0.012472	0.018532	0.021073
AS1g2r15	0.016069	0.009791	0.012766	0.015933
AS1g6r5	0.019002	0.009521	0.009652	0.013381
AS1g12r5	0.019381	0.008914	0.009851	0.014416
Sum Σ	0.064645	0.040697	0.050802	0.064804

Table 5.8 Measured and predicted diameter D4 at fracture for AS heat treatment with $D_o = 1.078 \times 10^5$ $(MPa)^2$ and the corresponding calculated D_c.

Specimen	Ratio of diameter D4 over the original diameter at fracture			Corresponding calculated D_c at predicted failure
	Measured	Predicted	% error	
AS1g2r5	0.787	0.750	-4.8	0.218
AS1g2r15	0.749	0.705	-5.9	0.265
AS1g6r5	0.716	0.696	-2.8	0.290
AS1g12r5	0.680	0.667	-2.0	0.301
AS1g50r5	0.616	0.648	5.1	0.314
AS1g50r7	0.611	0.647	5.9	0.314

Table 5.9 Measured and predicted diameter D4 at fracture for AS heat treatment with constant $D_c = 0.278$.

Specimen	Ratio of diameter D4 over the original diameter at fracture		
	Measured	Predicted	% error
AS1g2r5	0.787	0.716	-9.1
AS1g2r15	0.749	0.697	-6.9
AS1g6r5	0.716	0.703	-1.8
AS1g12r5	0.680	0.679	-0.1
AS1g50r5	0.616	0.667	8.2
AS1g50r7	0.611	0.666	9.1

Table 5.10 Measured and predicted peak stress for AS heat treatment.

Specimen	Peak stress, MPa		
	Measured	Predicted	% error
AS1g2r5	638.5	632.9	-0.9
AS1g2r15	586.8	578.0	-1.5
AS1g6r5	572.8	568.0	-0.8
AS1g12r5	537.9	533.7	-0.8
AS1g50r5	516.6	517.3	0.1
AS1g50r7	520.3	517.2	-0.6

Table 5.11 Material properties and parameters used in the analyses for AN heat treatment.

Elastic modulus = 212000 MPa		Poisson's ratio = 0.3				$\varepsilon^{p}_{eq_c}$ = 0.0	
n = 0.1	s^{-n} = 0.28	n = 0.5	s^{-n} = 0.20	n = 1. 0	s^{-n} = 0.15	n = 1.5	s^{-n} = 0.09
True plastic strain, mm/mm	Effective true stress, MPa	True plastic strain, mm/mm	Effective true stress, MPa	True plastic strain, mm/mm	Effective true stress, MPa	True plastic strain, mm/mm	Effective true stress, MPa
0.00000	330	0.00000	330	0.00000	330	0.00000	350
0.01077	336	0.01080	336	0.01081	336	0.00143	351
0.02359	355	0.02368	354	0.02370	353	0.00592	353
0.03891	425	0.03908	423	0.03914	422	0.02054	368
0.05706	474	0.05737	470	0.05748	469	0.02848	417
0.07920	514	0.07968	510	0.07987	507	0.04072	463
0.10237	547	0.10307	541	0.10334	538	0.05374	493
0.12552	568	0.12645	561	0.12683	557	0.07190	533
0.16196	601	0.16327	592	0.16384	587	0.09043	551
0.19889	635	0.20061	624	0.20139	617	0.11015	572
0.25082	673	0.25317	660	0.25428	651	0.13040	592
0.28754	694	0.29035	677	0.29171	669	0.15173	607
4.00000	2817	4.00000	2494	4.00000	2361	4.00000	2094

Table 5.12 Calculated err for AN heat treatment.

Specimen	err			
	n = 0.1	n = 0.5	n = 1.0	n = 1.5
AN1g2r5	0.007193	0.011236	0.015905	0.018817
AN1g6r5	0.016639	0.005938	0.005286	0.008115
AN1g12r5	0.015524	0.005273	0.007968	0.013356
Sum Σ	0.039357	0.022447	0.029159	0.040288

Table 5.13 Measured and predicted diameter D4 at fracture for AN heat treatment with $D_o = 7.78 \times 10^4$ $(MPa)^2$ and the corresponding calculated D_c.

Specimen	Ratio of diameter D4 over the original diameter at fracture			Corresponding calculated D_c at predicted failure
	Measured	Predicted	% error	
AN1g2r5	0.788	0.758	-3.9	0.168
AN1g6r5	0.731	0.704	-3.7	0.232
AN1g12r5	0.683	0.673	-1.5	0.244
AN1g50r5	0.627	0.651	3.8	0.256

Table 5.14 Measured and predicted diameter D4 at fracture for AN heat treatment with constant $D_c = 0.216$.

Specimen	Ratio of diameter D4 over the original diameter at fracture		
	Measured	Predicted	% error
AN1g2r5	0.788	0.723	-8.3
AN1g6r5	0.731	0.716	-2.1
AN1g12r5	0.683	0.694	1.6
AN1g50r5	0.627	0.679	8.2

Table 5.15 Measured and predicted peak stress for AN heat treatment.

Specimen	Peak stress, MPa		
	Measured	Predicted	% error
AN1g2r5	615.7	602.4	-2.2
AN1g6r5	550.5	543.2	-1.3
AN1g12r5	517.9	511.4	-1.3
AN1g50r5	494.5	495.2	0.1

Table 5.16 Material properties and parameters used in the analyses for NM heat treatment.

Elastic modulus = 202000 MPa		Poisson's ratio = 0.3				$\varepsilon^{p}_{eq_c}$ = 0.0	
n = 0.5	s^{-n} = 0.20	n = 1.0	s^{-n} = 0.13	n = 1. 5	s^{-n} = 0.08	n = 2.0	s^{-n} = 0.055
True plastic strain, mm/mm	Effective true stress, MPa	True plastic strain, mm/mm	Effective true stress, MPa	True plastic strain, mm/mm	Effective true stress, MPa	True plastic strain, mm/mm	Effective true stress, MPa
0.00000	280	0.00000	280	0.00000	280	0.00000	280
0.00294	404	0.00294	403	0.00294	403	0.00294	403
0.01065	461	0.01066	461	0.01066	461	0.01066	461
0.02482	530	0.02486	529	0.02488	529	0.02488	528
0.04303	580	0.04312	578	0.04316	577	0.04317	576
0.06449	608	0.06467	605	0.06475	604	0.06478	603
0.08514	643	0.08541	639	0.08554	637	0.08559	636
0.10387	661	0.10424	657	0.10443	654	0.10644	654
0.14366	693	0.14426	687	0.14458	683	0.14471	681
0.18514	715	0.18602	707	0.18652	701	0.18672	698
4.00000	2714	4.00000	2499	4.00000	2328	4.00000	2224

Table 5.17 Calculated err for NM heat treatment.

	err			
Specimen	n = 0.5	n = 1.0	n = 1.5	n = 2.0
NM1g2r5	0.01368	0.00842	0.00643	0.00682
NM1g6r5	0.01210	0.00713	0.00592	0.00634
NM1g12r5	0.00779	0.00423	0.00622	0.00831
Sum Σ	0.03357	0.01979	0.01857	0.02147

Table 5.18 Measured and predicted diameter D4 at fracture for NM heat treatment with $D_o = 5.34 \times 10^4$ (MPa)^2 and the corresponding calcullated D_c.

Specimen	Ratio of diameter D4 over the original diameter at fracture			Corresponding calculated D_c at predicted failure
	Measured	Predicted	% error	
NM1g2r5	0.847	0.862	1.7	0.097
NM1g6r5	0.813	0.789	-3.0	0.161
NM1g12r5	0.707	0.728	3.0	0.171
NM1g50r5	0.688	0.702	2.1	0.177

Table 5.19 Measured and predicted diameter D4 at fracture for NM heat treatment with constant $D_c = 0.166$.

Specimen	Ratio of diameter D4 over the original diameter at fracture		
	Measured	Predicted	% error
NM1g2r5	0.847	0.824	-2.8
NM1g6r5	0.813	0.786	-3.4
NM1g12r5	0.707	0.731	3.4
NM1g50r5	0.688	0.708	3.0

Table 5.20 Measured and predicted peak stress for NM heat treatment.

Specimen	Peak stress, MPa		
	Measured	Predicted	% error
NM1g2r5	732.5	729.0	-0.5
NM1g6r5	659.4	647.4	-1.8
NM1g12r5	602.6	605.8	0.5
NM1g50r5	583.6	585.0	0.2

Table 5.21 Calculated D_c at fracture for specimens with 5 mm transition radius.

Gage length	Corresponding calculated D_c at predicted failure		
	AS	AN	NM
g2	0.218	0.168	0.097
g6	0.290	0.232	0.161
g12	0.301	0.244	0.171
g50	0.314	0.256	0.177

Table 5.22 Material properties and parameters used in the analyses for models by Lemaitre and Matic et al.

Elastic modulus = 215000 MPa Poisson's ratio = 0.3			
$n = 0.1$ $s^{-n} = 0.36$ $\varepsilon^p_{eq_c} = 0.0$ (Lemaitre)		Matic et al.	
True plastic strain, mm/mm	Effective true stress, MPa	True plastic strain, mm/mm	True stress, MPa
0.00000	350	0.00000	350
0.00143	351	0.00143	351
0.00592	353	0.00592	353
0.02053	371	0.02054	368
0.02847	421	0.02848	417
0.04070	469	0.04073	462
0.05371	501	0.05375	492
0.07187	545	0.07193	532
0.09040	566	0.09048	549
0.11012	592	0.11022	570
0.13038	616	0.13051	589
0.15173	636	0.15189	603
0.17201	652	0.17219	613
0.20371	676	0.20393	628
0.24357	708	0.24385	647
0.33283	783	0.33327	687
0.36780	810	0.52715	748
4.00000	3595	0.68950	784
		0.87171	809
		4.00000	1235

Table 5.23 Err values for different material models.

Specimen	err		
	Proposed	Lemaitre	Matic et al.
AS1g2r5	-0.0319	-0.0604	-0.0609
AS1g2r15	-0.0240	-0.0718	-0.0769
AS1g6r5	0.0077	-0.0539	-0.0602
AS1g12r5	0.0041	-0.0960	-0.1125
Sum Σ	-0.0440	-0.2820	-0.3105

Table 5.24 Predicted diameter D4 at fracture for various material models.

Specimen	Ratio of diameter D4 over the original diameter at fracture						
	Measured	Proposed, D_o = 1.078×10^5 MPa^2		Lemaitre, $D_c = 0.316$		Matic et al., Strain energy density limit = 0.553 Nm/m^3	
		Predicted	% error	Predicted	% error	Predicted	% error
AS1g2r5	0.787	0.750	-4.8	0.693	-12.0	0.686	-12.9
AS1g2r15	0.749	0.705	-5.9	0.696	-7.1	0.695	-7.2
AS1g6r5	0.716	0.696	-2.8	0.708	-1.1	0.708	-1.1
AS1g12r5	0.680	0.667	-2.0	0.696	2.3	0.700	2.9
AS1g50r5	0.616	0.648	5.1	0.684	11.1	0.690	12.0
AS1g50r7	0.611	0.647	5.9	0.684	12.0	0.690	12.9

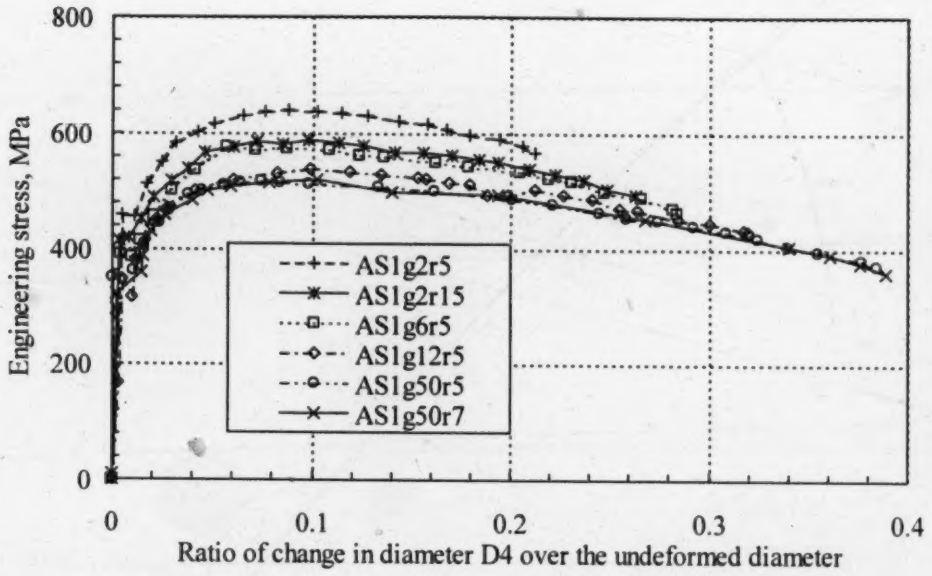

Figure 5.1 Measured stress versus change in diameter D4 for AS heat treatment.

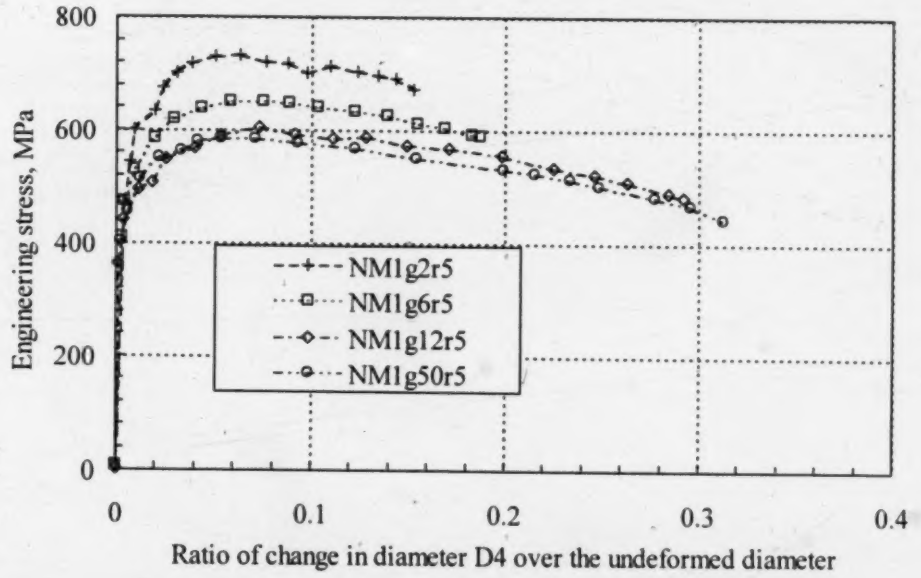

Figure 5.2 Measured stress versus change in diameter D4 for NM heat treatment.

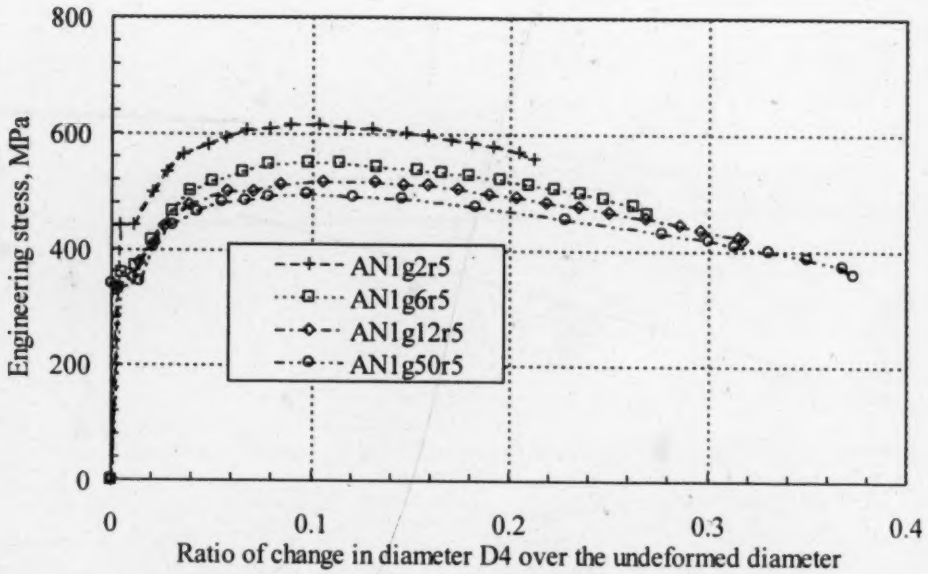

Figure 5.3 Measured stress versus change in diameter D4 for AN heat treatment.

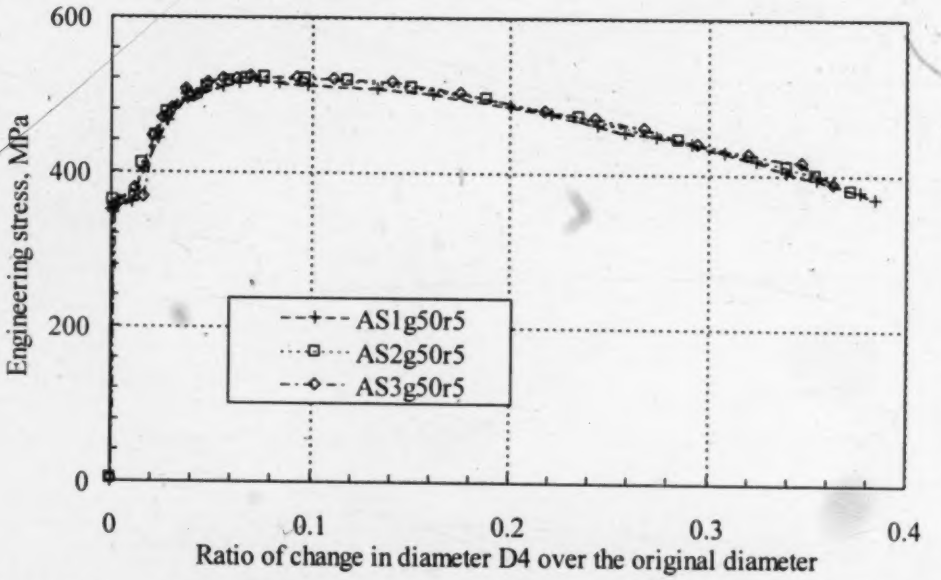

Figure 5.4 Measured stress versus change in diameter D4 for monotonic, and load and unload tests.

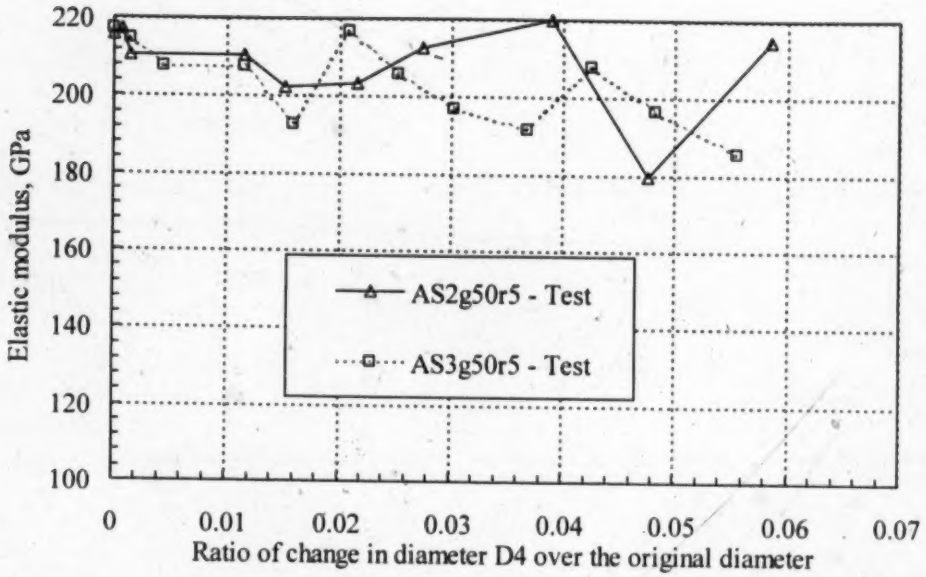

Figure 5.5 Measured apparent elastic modulus versus change in diameter D4 for load and unload specimens.

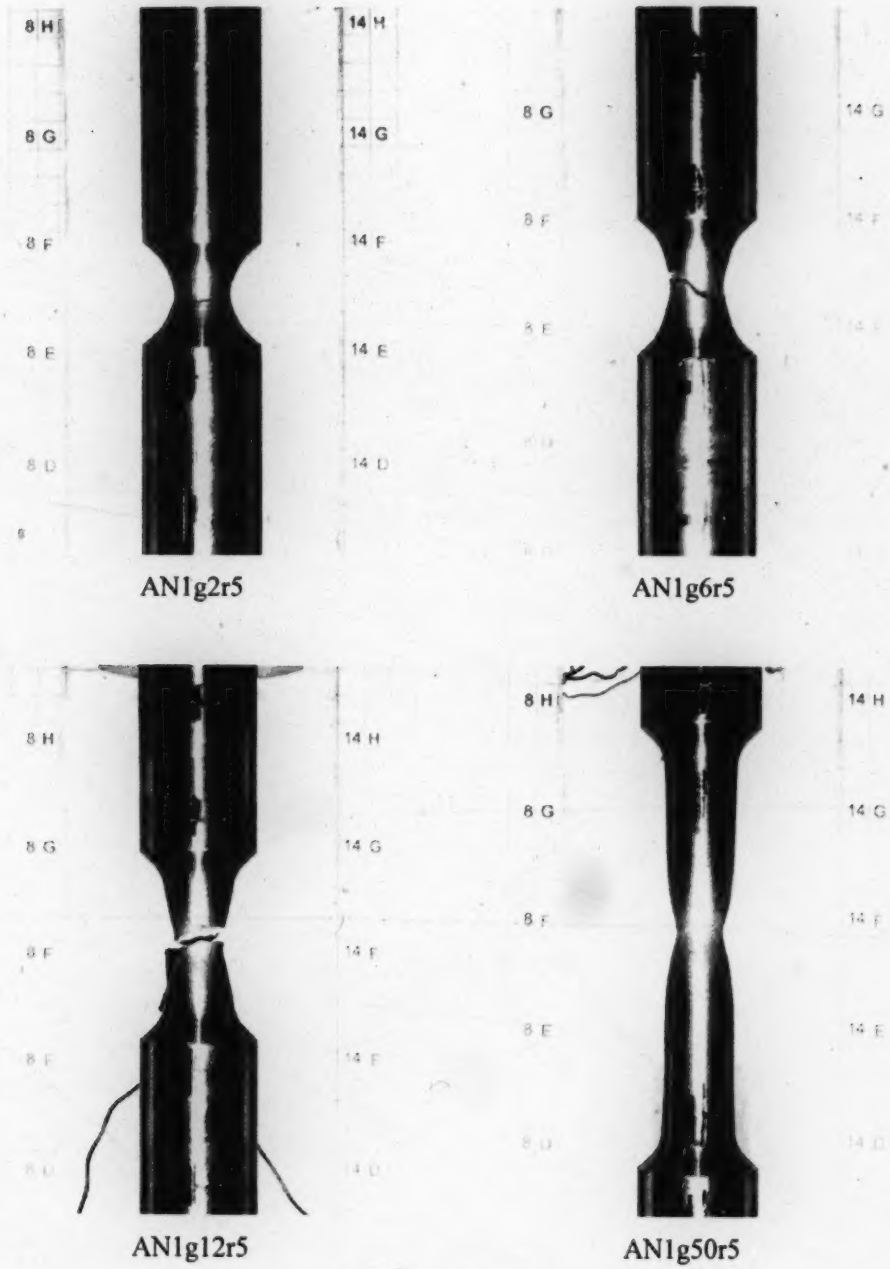

Figure 5.6 Fracture of AN heat treatment specimens.

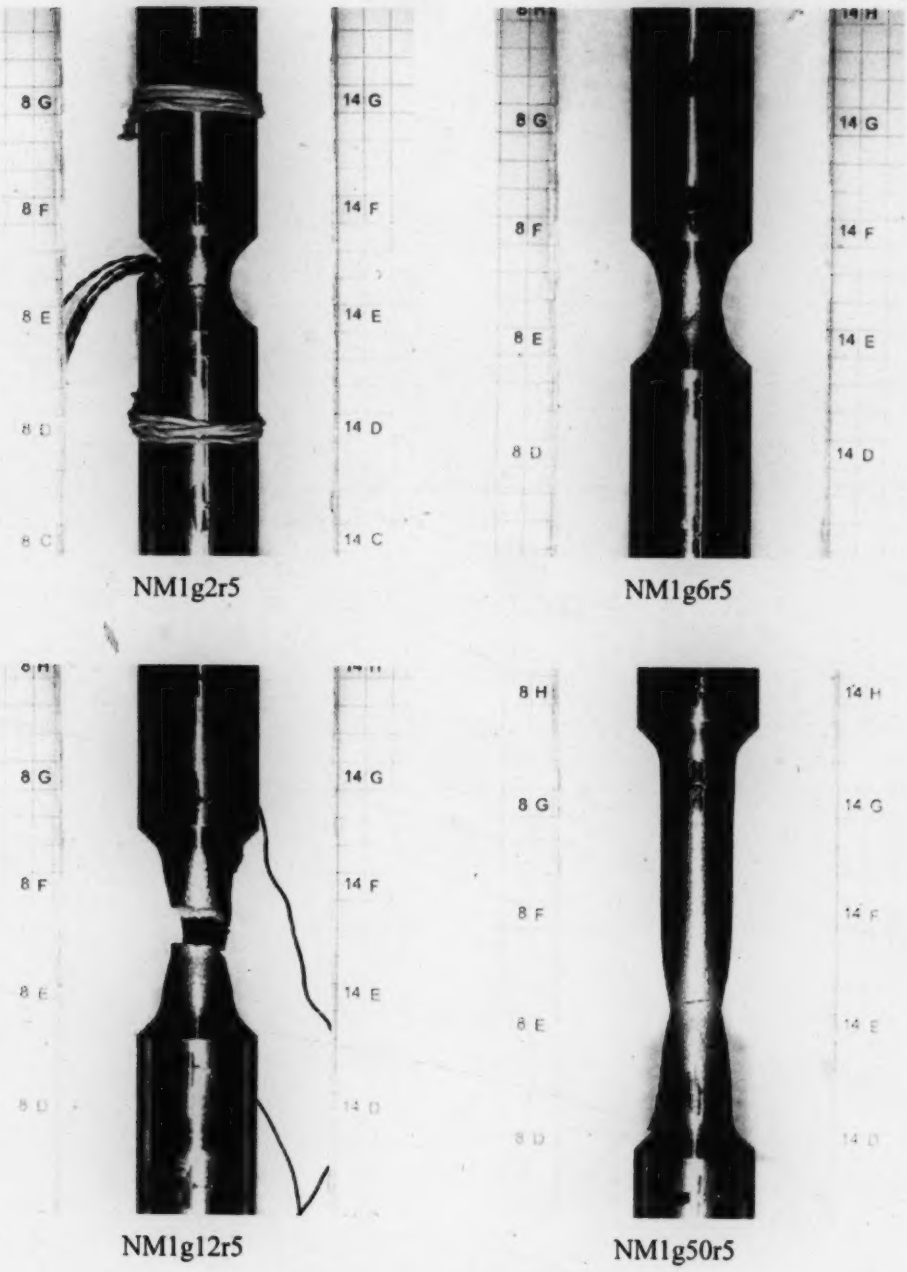

Figure 5.7 Fracture of NM heat treatment specimens.

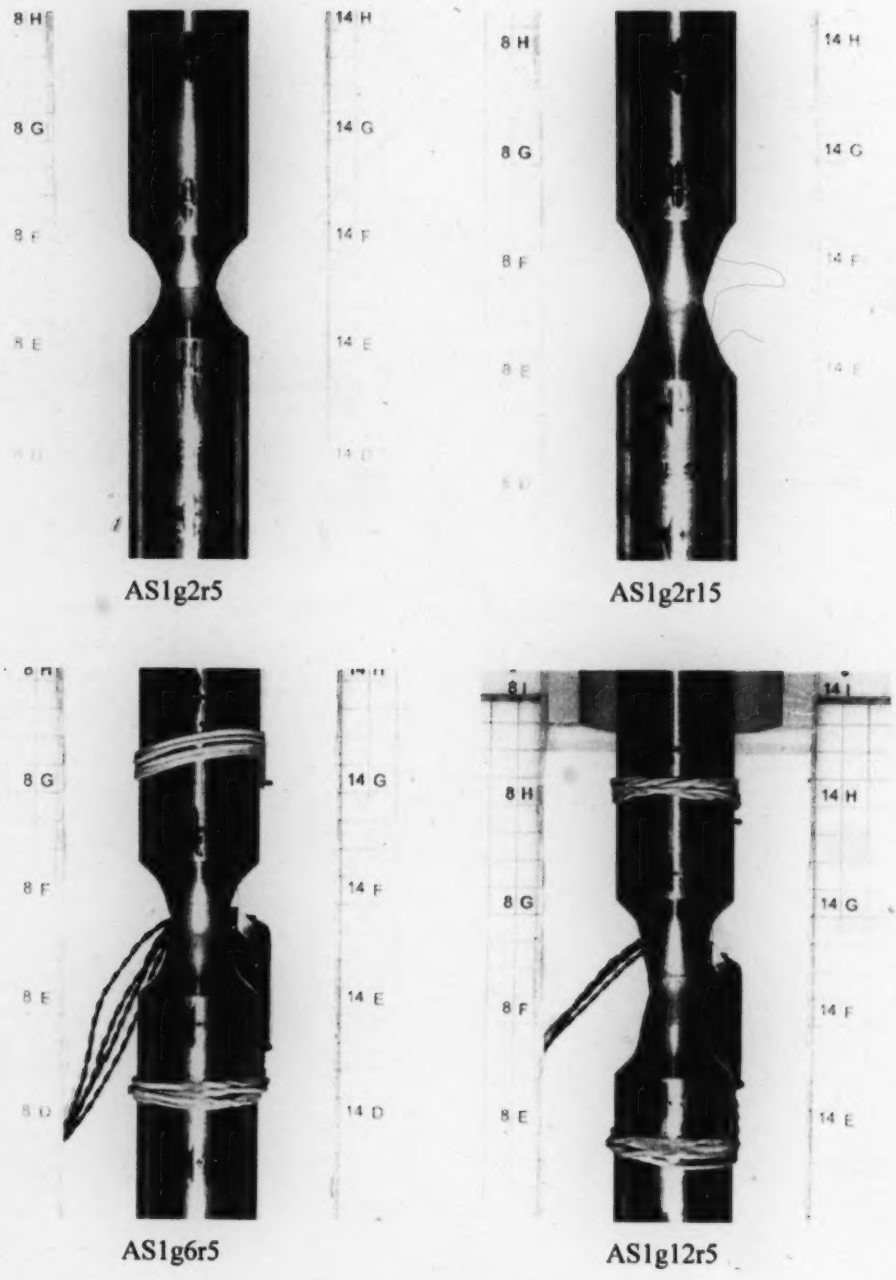

Figure 5.8 Fracture of AS heat treatment specimens.

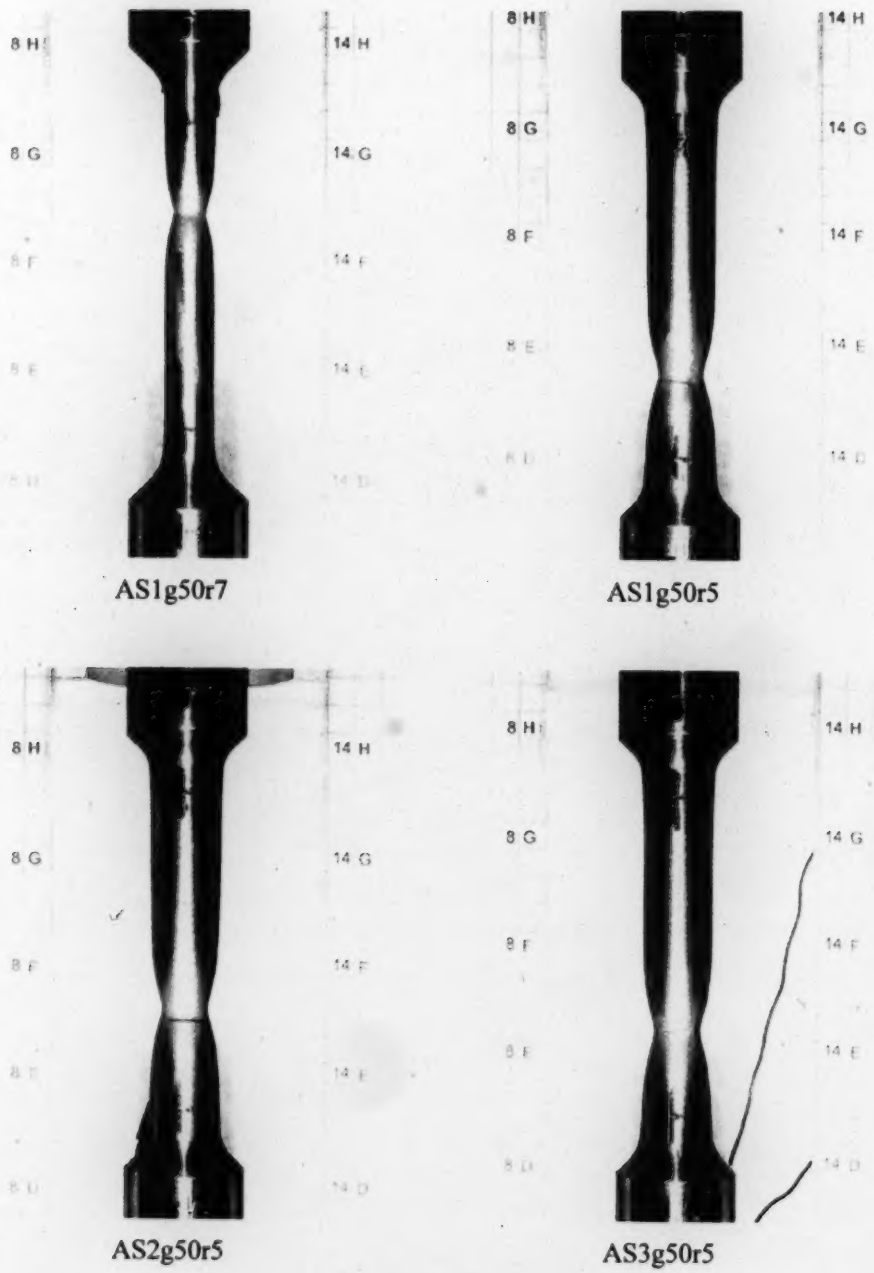

Figure 5.9 Fracture of AS heat treatment specimens.

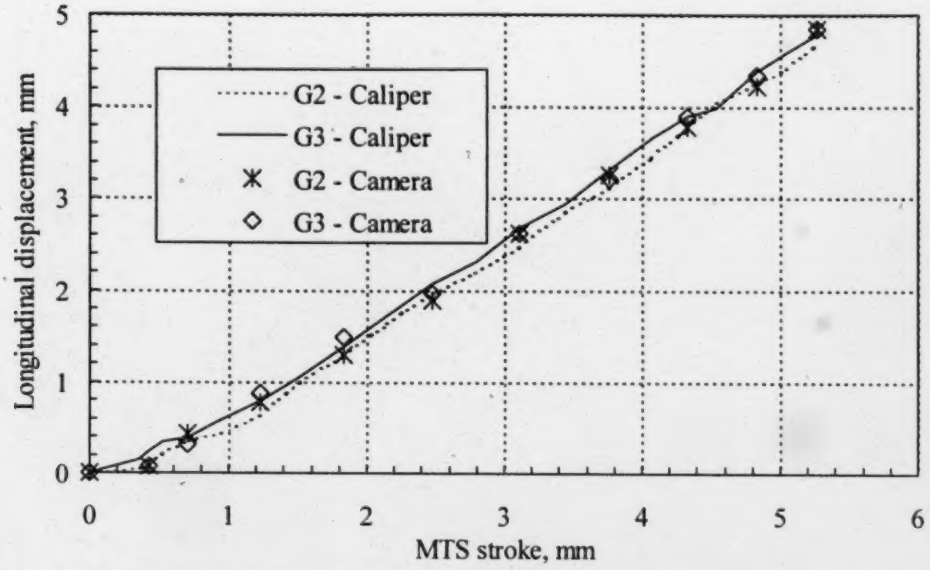

Figure 5.10 G2 and G3 extensions from caliper and camera for AS1g6r5.

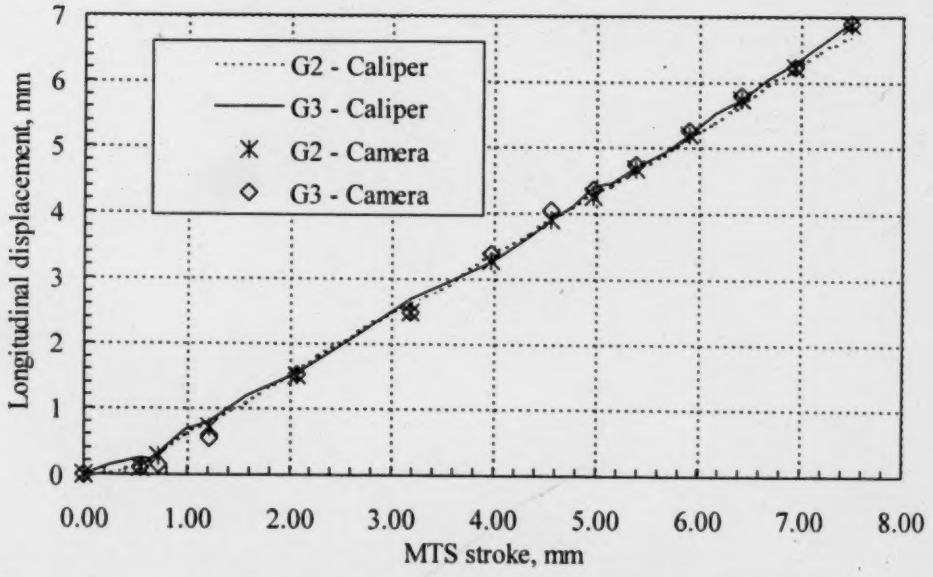

Figure 5.11 G2 and G3 extensions from caliper and camera for AS1g12r5.

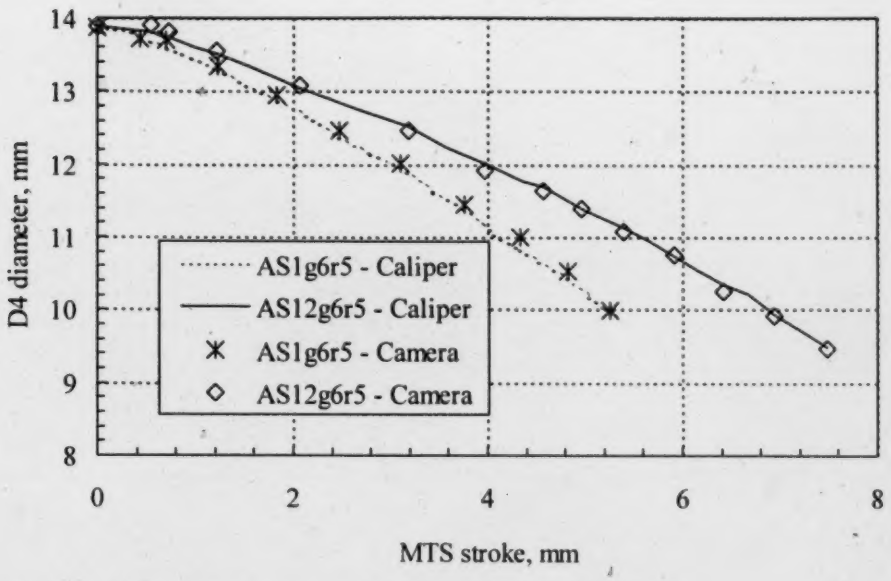

Figure 5.12 D4 diameter measurement from caliper and camera.

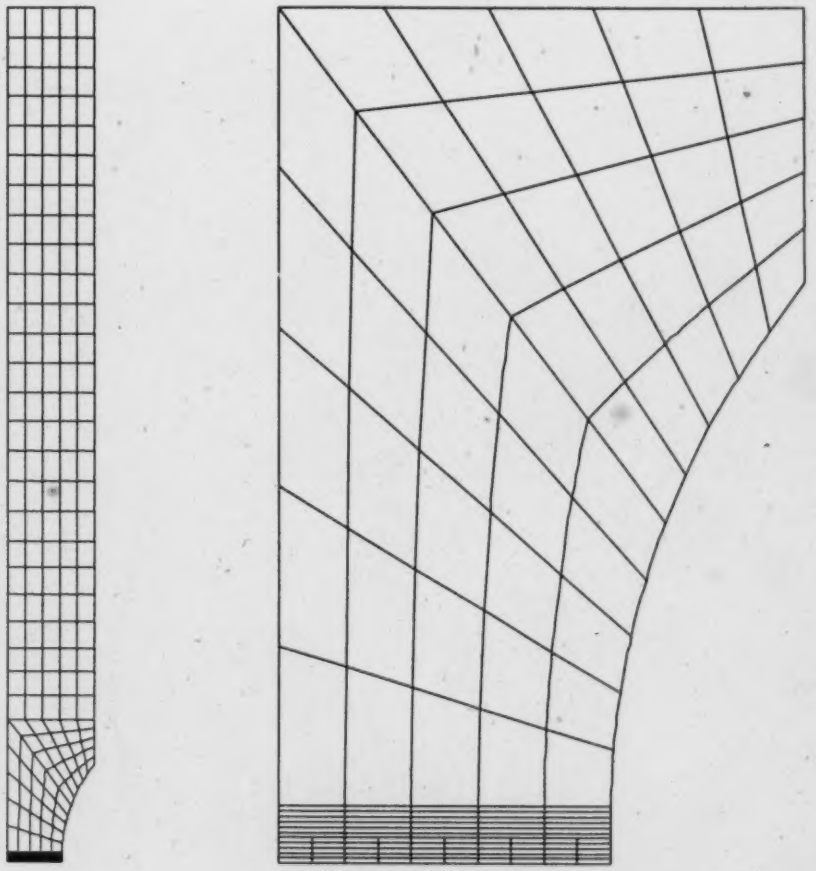

Overall

Mesh at the neck section is magnified for clarity.

Figure 5.13 Finite element mesh for AS1g2r15.

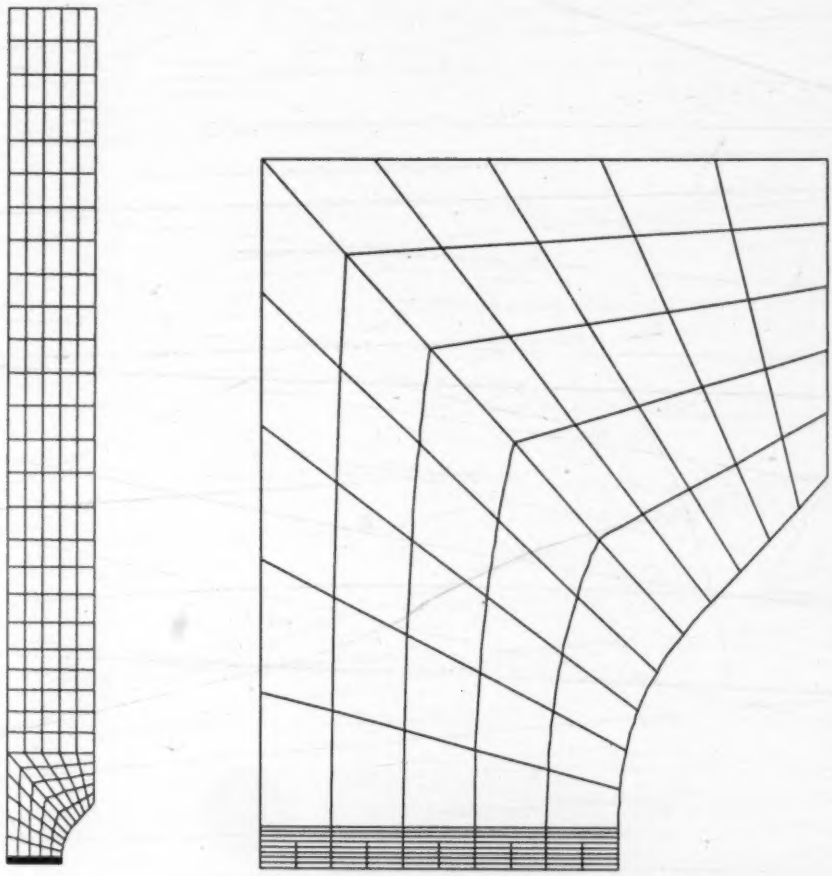

Overall

Mesh at the neck section is magnified for clarity.

Figure 5.14 Finite element mesh for AS1g2r5, NM1g2r5 and AN1g2r5.

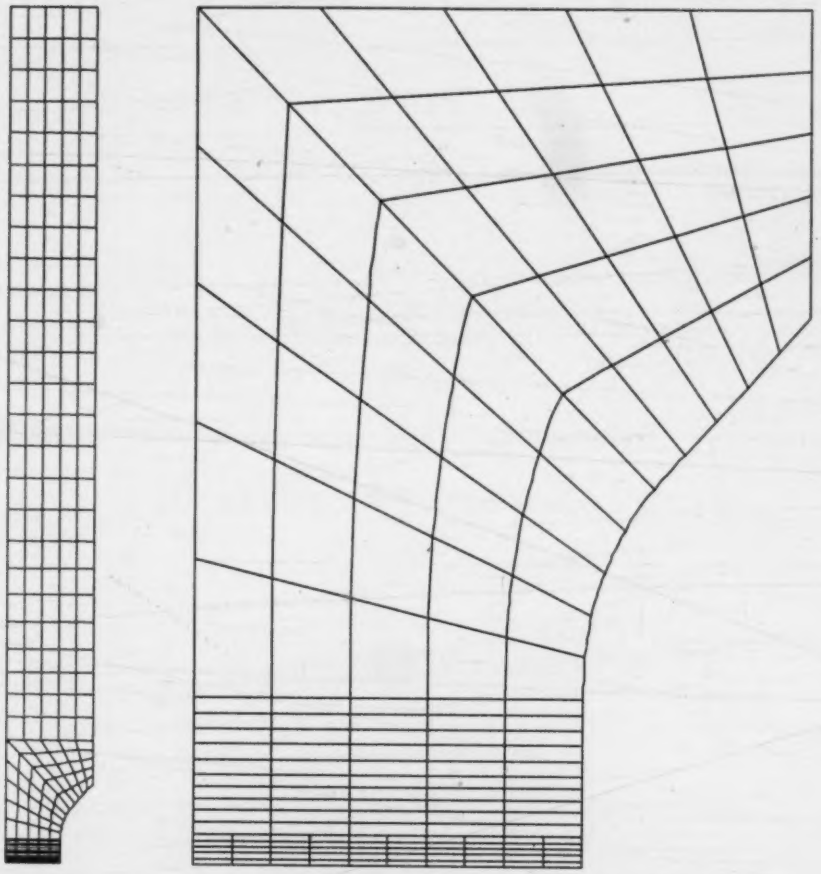

Overall

Mesh at the neck section is magnified for clarity.

Figure 5.15 Finite element mesh for AS1g6r5, NM1g6r5 and AN1g6r5.

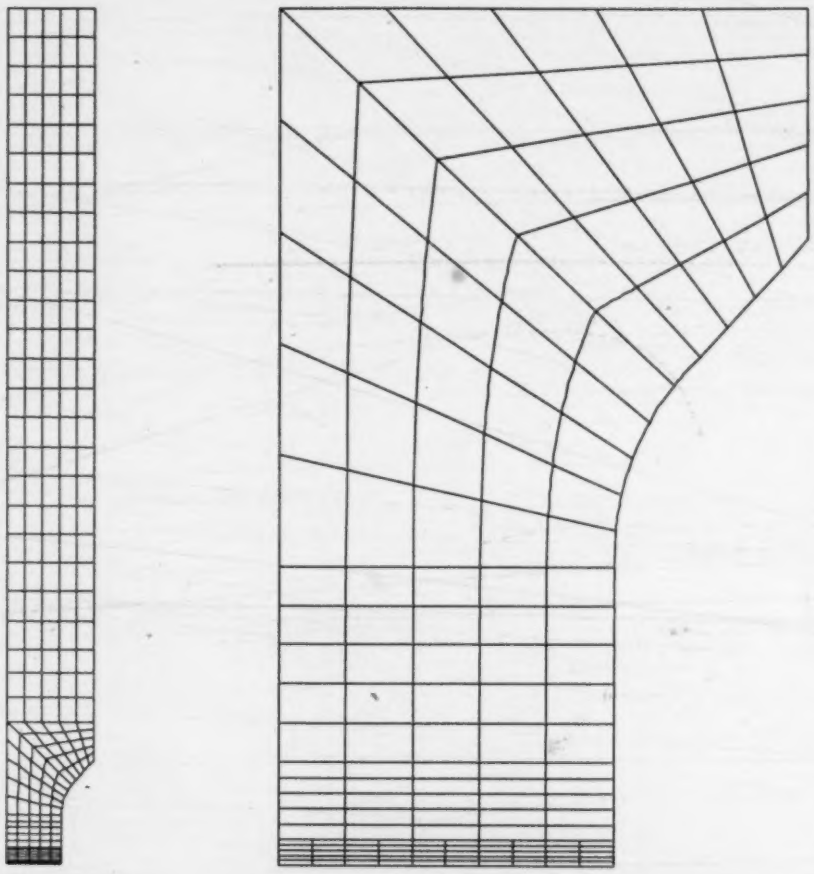

Overall

Mesh at the neck section is magnified for clarity.

Figure 5.16 Finite element mesh for AS1g12r5, NM1g12r5 and AN1g12r5.

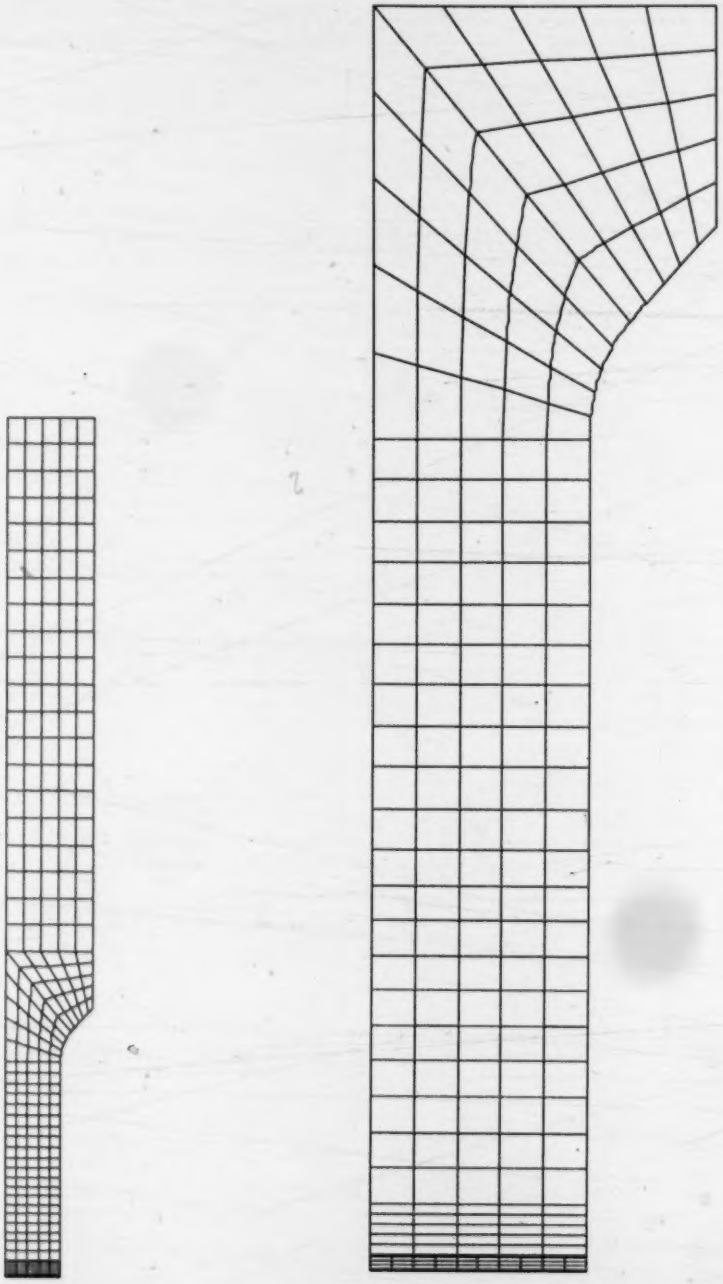

Overall

Mesh at the neck section is magnified for clarity.

Figure 5.17 Finite element mesh for AS1g50r5, NM1g50r5 and AN1g50r5.

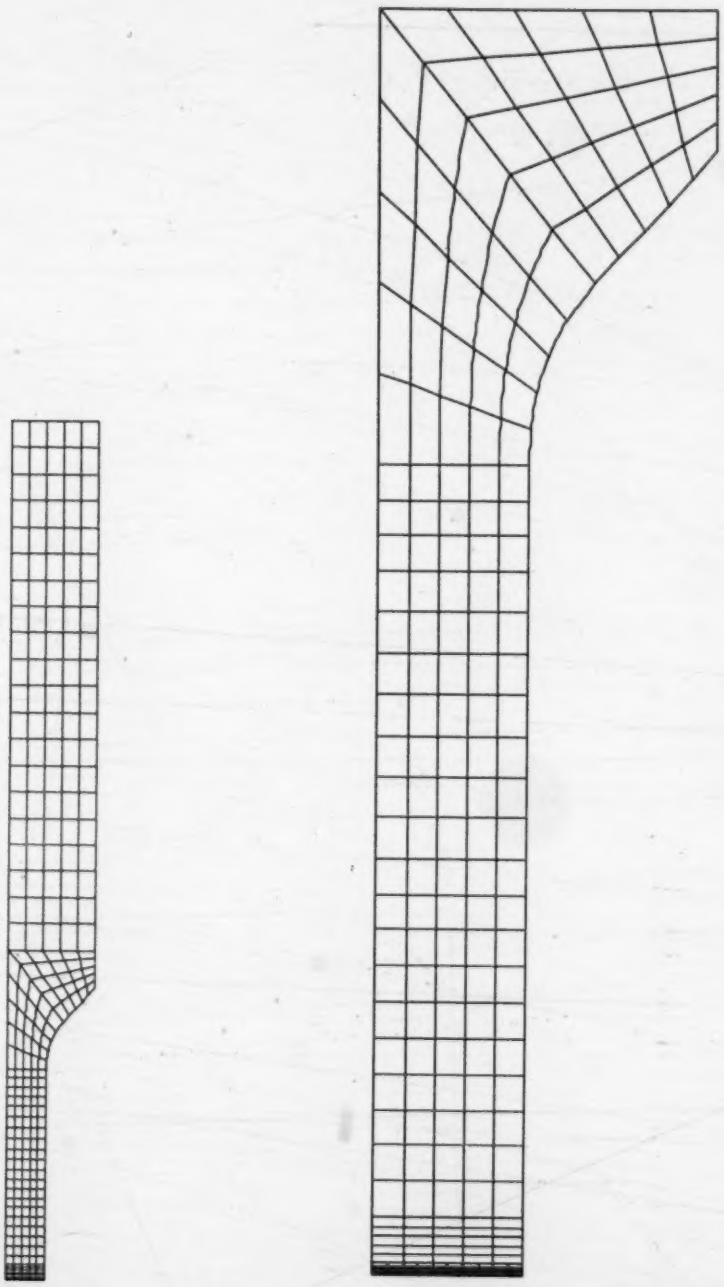

Overall

Mesh at the neck section is magnified for clarity.

Figure 5.18 Finite element mesh for AS1g50r7.

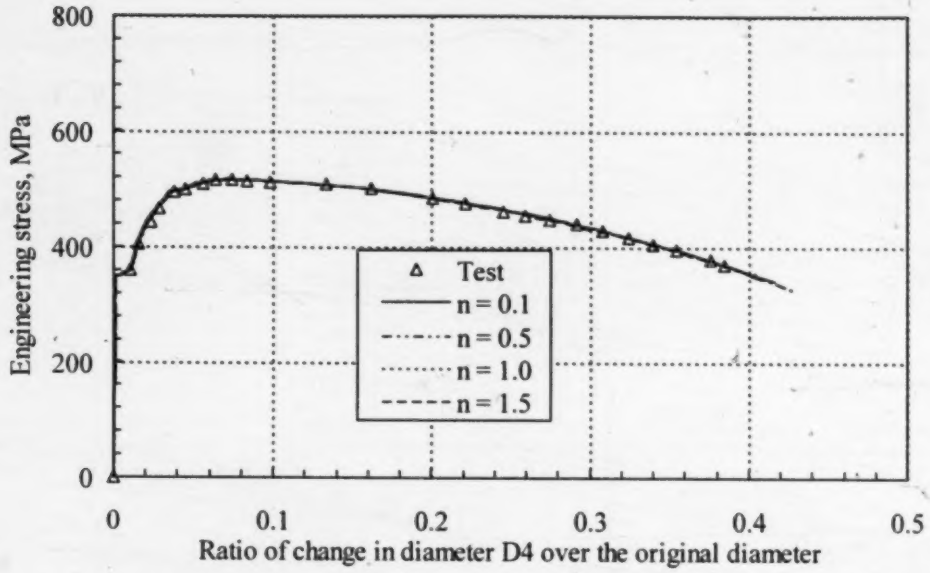

Figure 5.19 Measured and analytical stress versus change in diameter D4 for AS1g50r5.

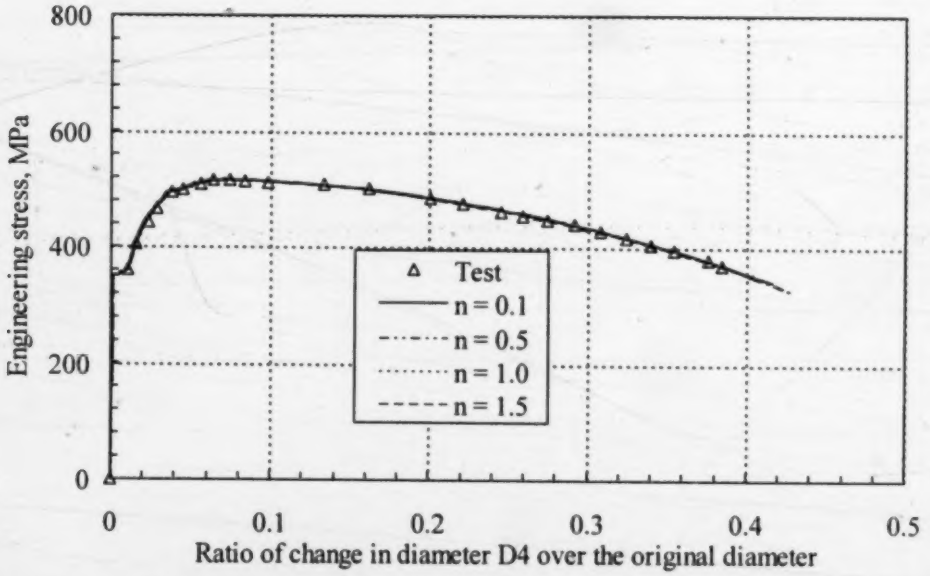

Figure 5.20 Measured and analytical stress versus change in diameter D4 for AS1g50r7.

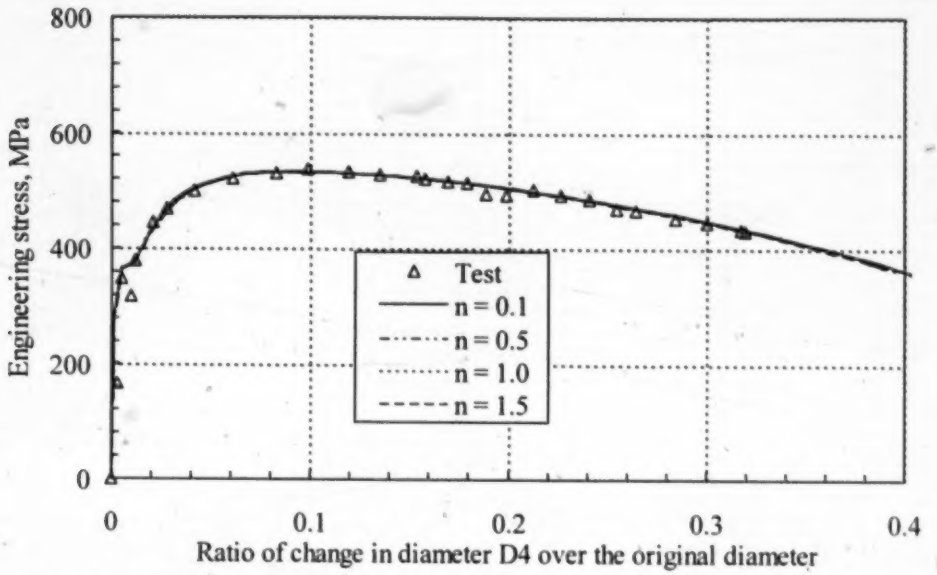

Figure 5.21 Measured and analytical stress versus change in diameter D4 for AS1g12r5.

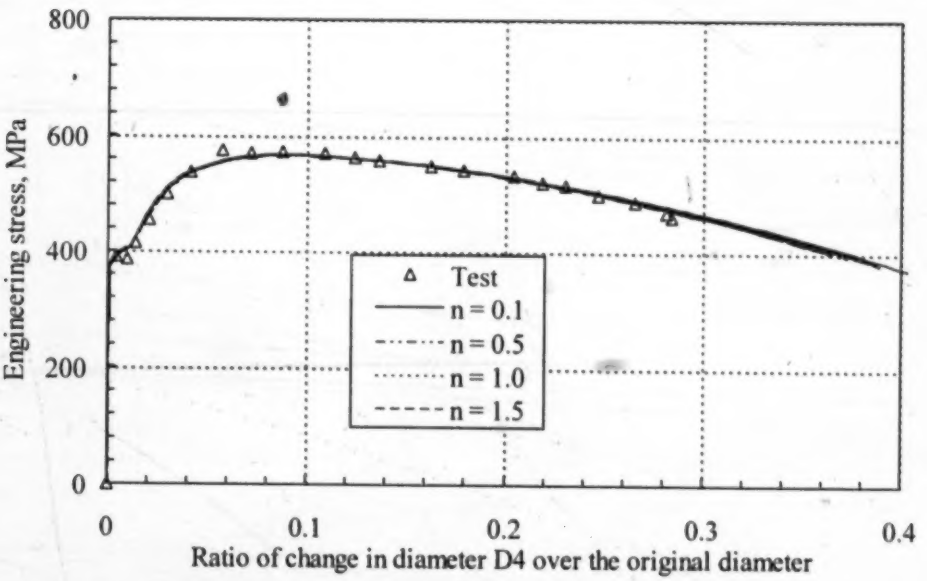

Figure 5.22 Measured and analytical stress versus change in diameter D4 for AS1g6r5.

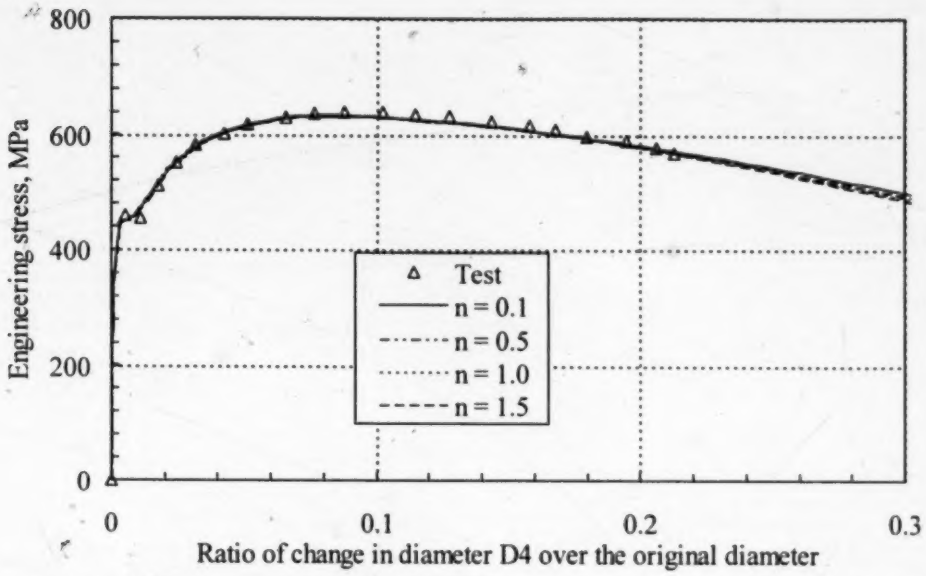

Figure 5.23 Measured and analytical stress versus change in diameter D4 for AS1g2r5.

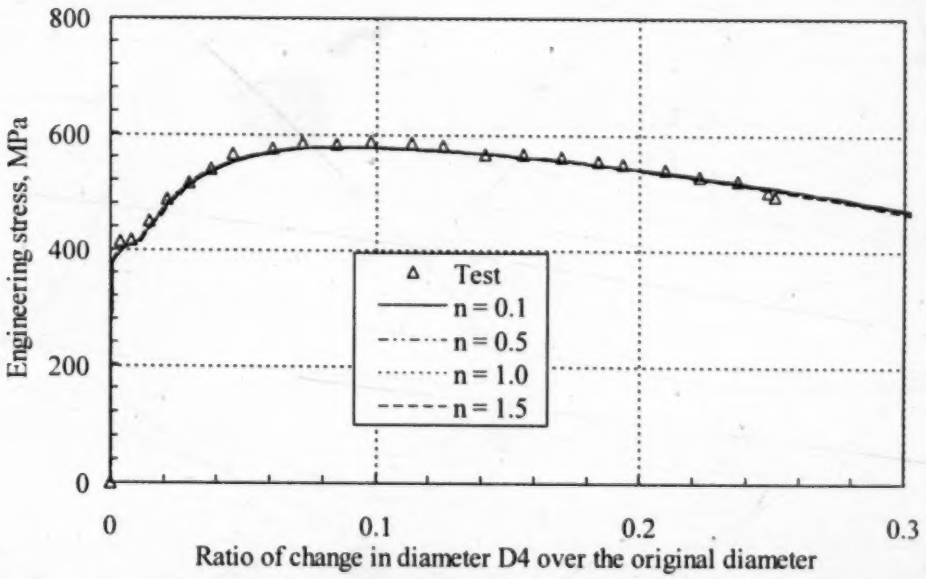

Figure 5.24 Measured and analytical stress versus change in diameter D4 for AS1g2r15.

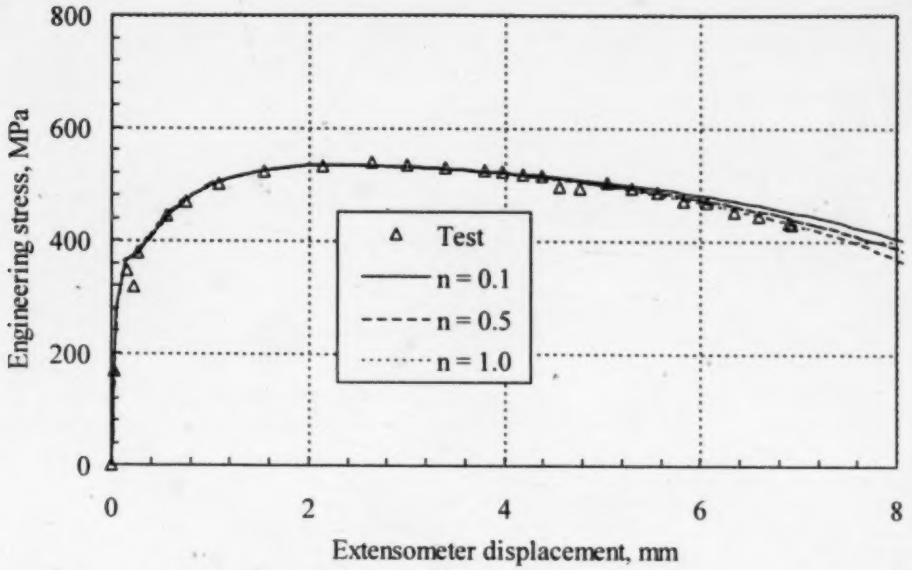

Figure 5.25 Measured and analytical stress versus extensometer displacement for AS1g12r5.

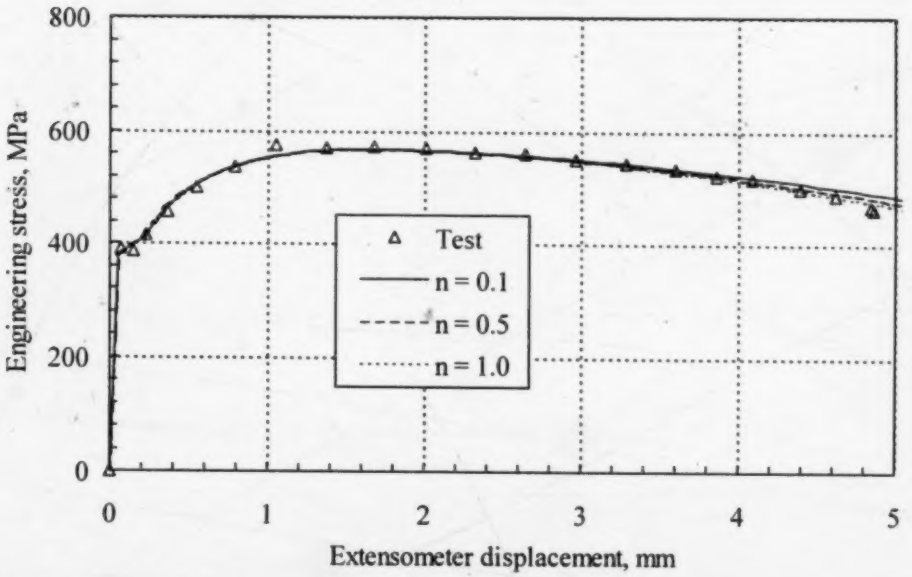

Figure 5.26 Measured and analytical stress versus extensometer displacement for AS1g6r5.

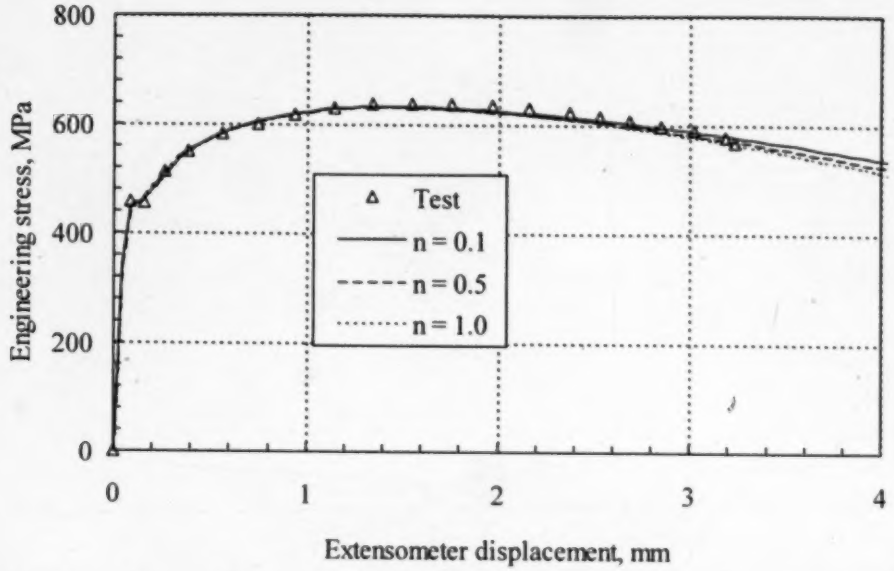

Figure 5.27 Measured and analytical stress versus extensometer displacement for AS1g2r5.

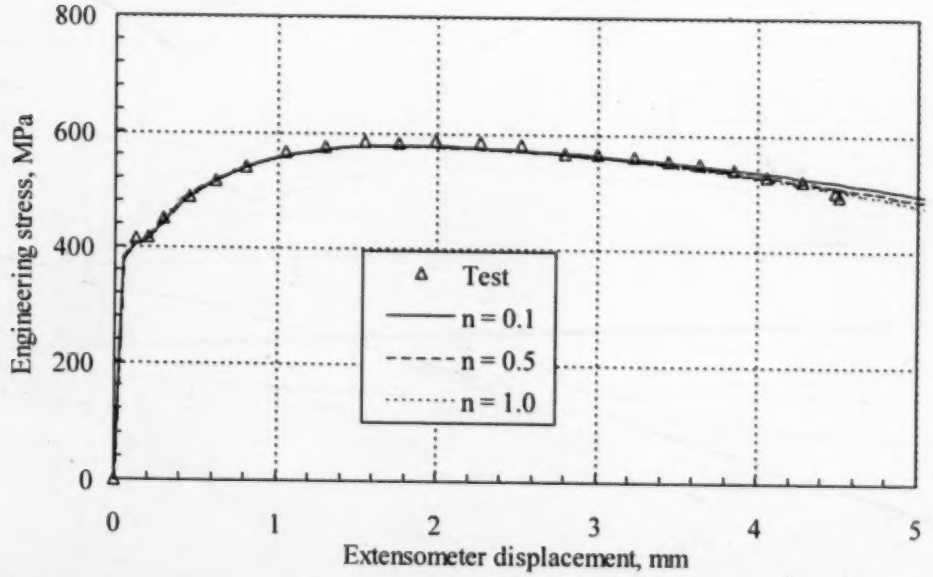

Figure 5.28 Measured and analytical stress versus extensometer displacement for AS1g2r15.

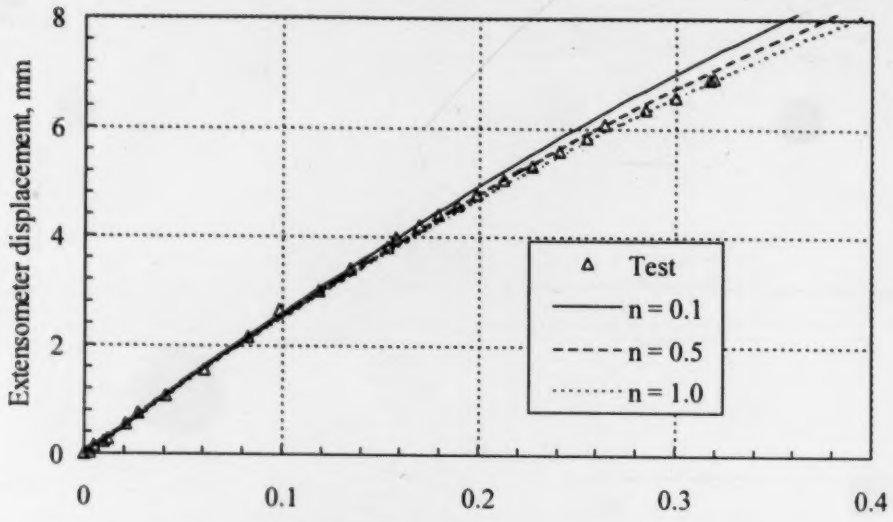

Figure 5.29 Measured and analytical extensometer displacement versus change in diameter D4 for AS1g12r5.

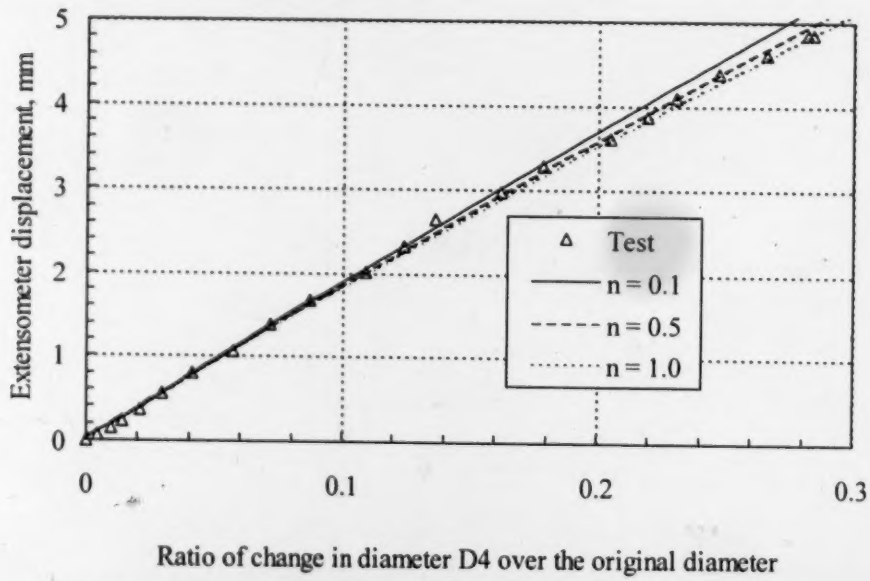

Figure 5.30 Measured and analytical extensometer displacement versus change in diameter D4 for AS1g6r5.

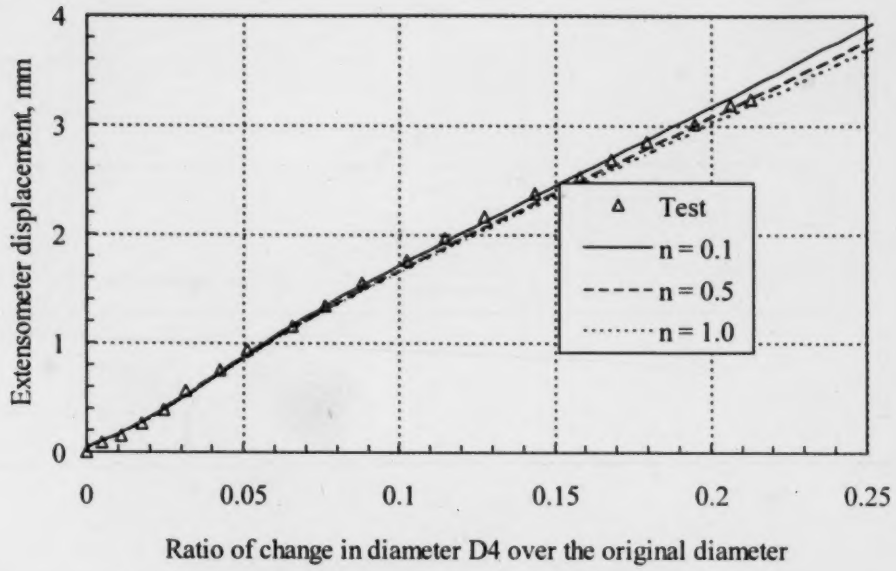

Figure 5.31 Measured and analytical extensometer displacement versus change in diameter D4 for AS1g2r5.

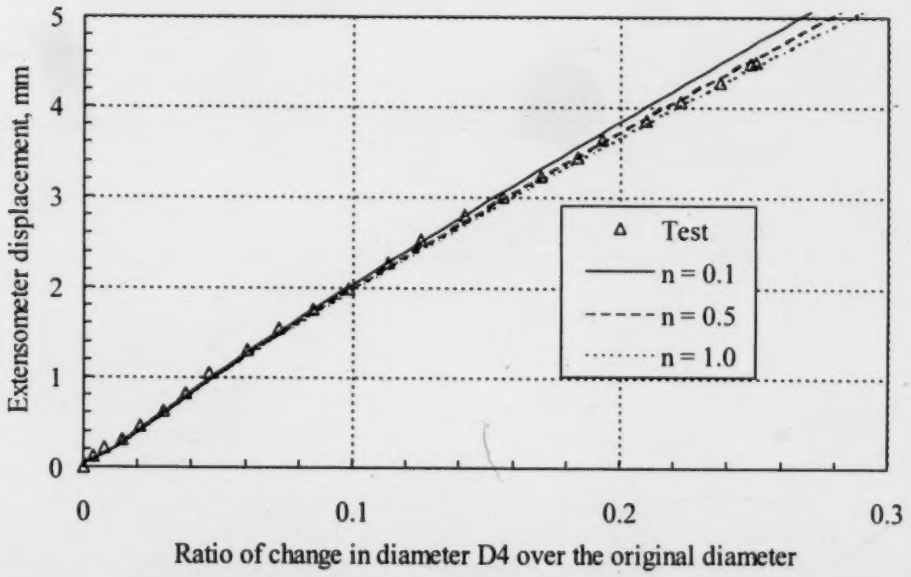

Figure 5.32 Measured and analytical extensometer displacement versus change in diameter D4 for AS1g2r15.

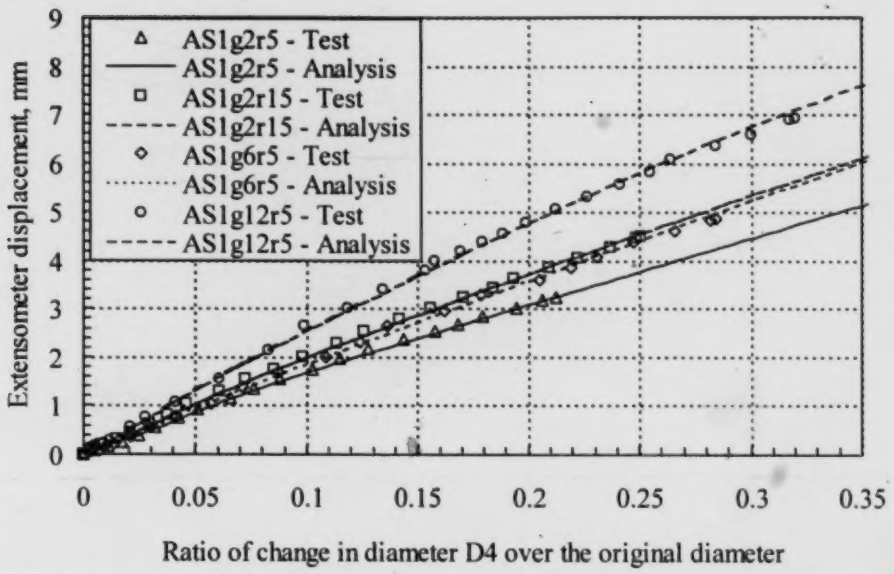

Figure 5.33 Measured and analytical extensometer displacement versus change in diameter D4 for AS specimens with gage length less than 12 mm and n = 0.5.

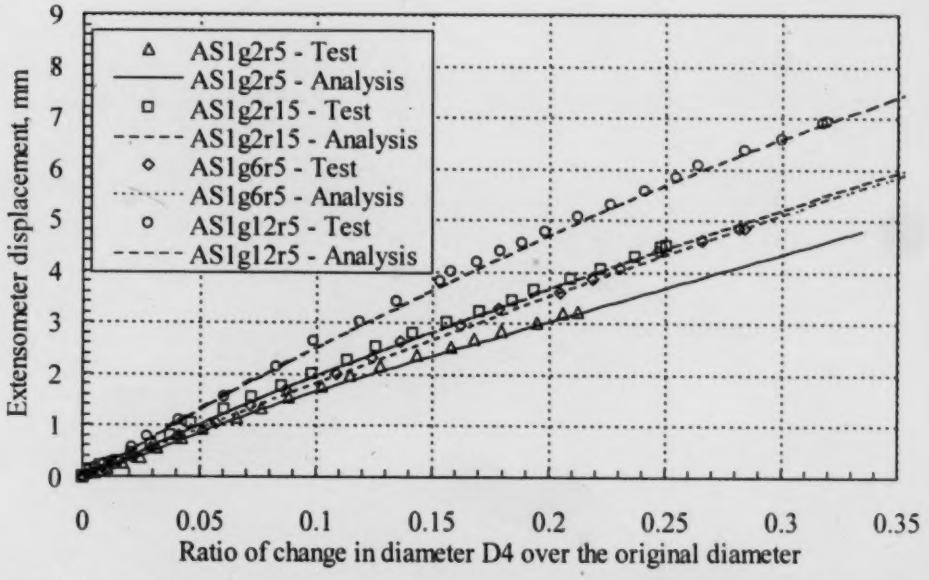

Figure 5.34 Measured and analytical extensometer displacement versus change in diameter D4 for AS specimens with gage length less than 12 mm and n = 1.0.

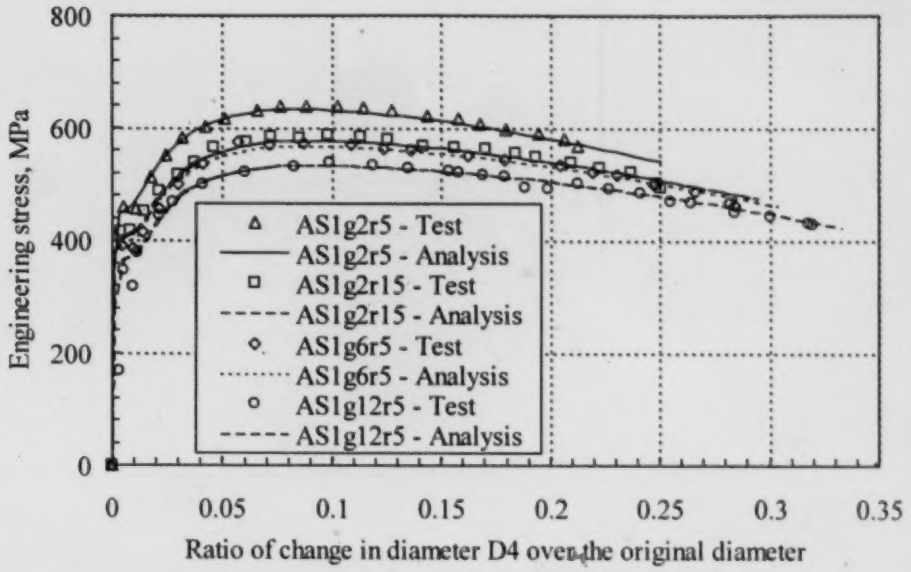

Figure 5.35 Measured and analytical stress versus change in diameter D4 for AS specimens with gage length less than 12 mm and n = 0.5.

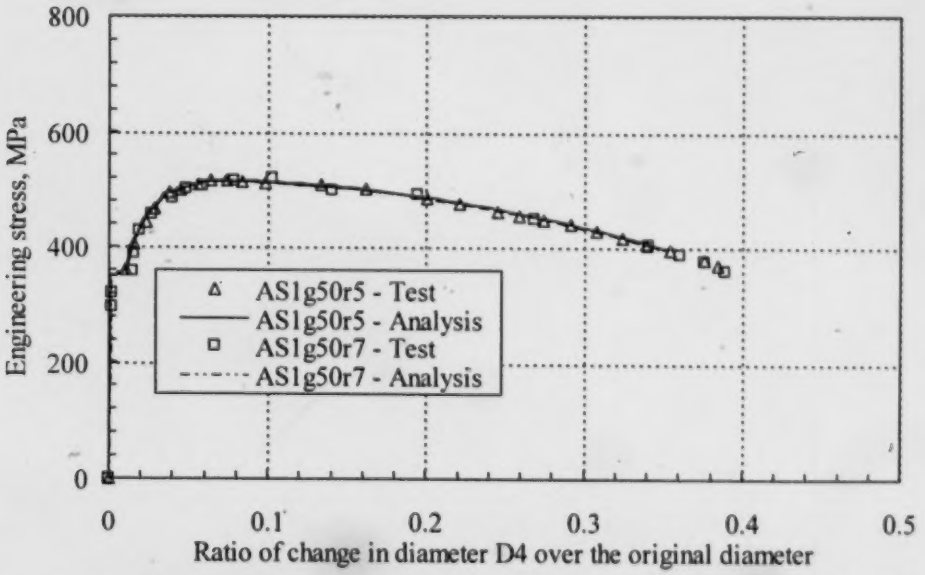

Figure 5.36 Measured and analytical stress versus change in diameter D4 for AS specimens with gage length equal to 50 mm and n = 0.5.

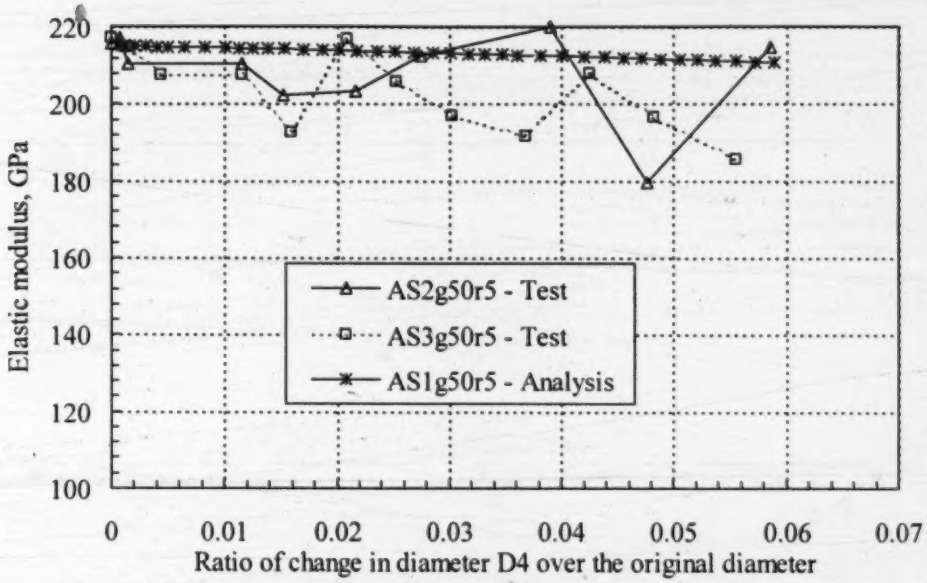

Figure 5.37 Measured and predicted apparent elastic modulus versus change in diameter D4 for load and unload specimens.

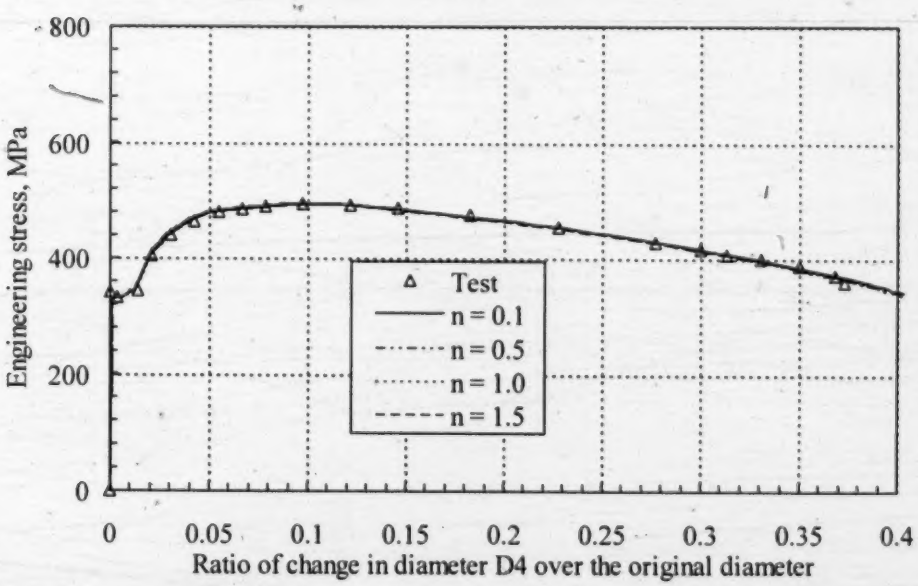

Figure 5.38 Measured and analytical stress versus change in diameter D4 for AN1g50r5.

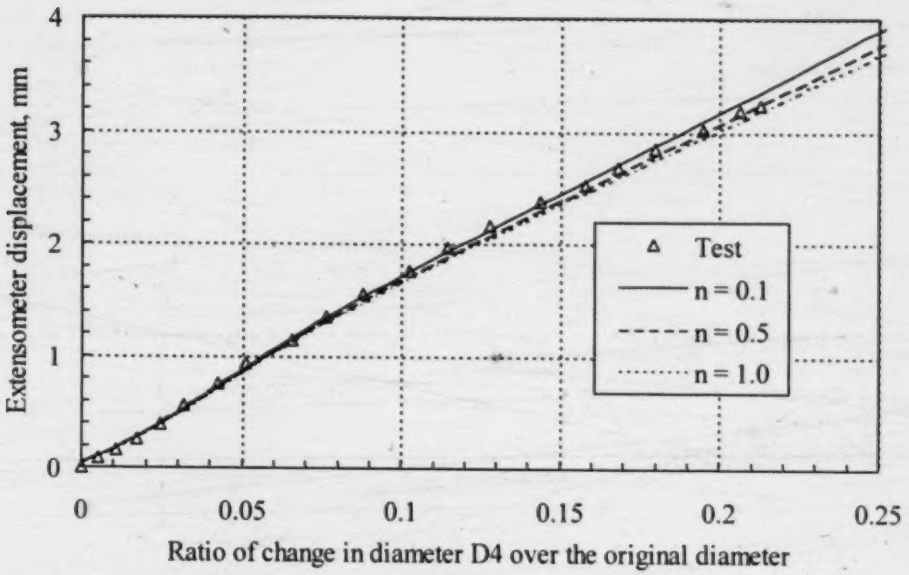

Figure 5.39 Measured and analytical extensometer displacement versus change in diameter D4 for AN1g2r5.

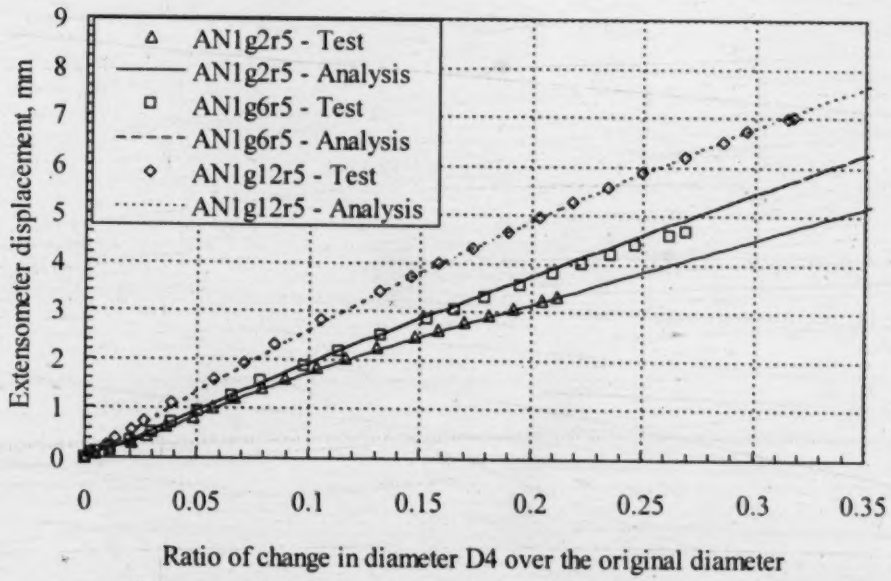

Figure 5.40 Measured and analytical extensometer displacement versus change in diameter D4 for AN specimens with gage length less than 12 mm and n = 0.5.

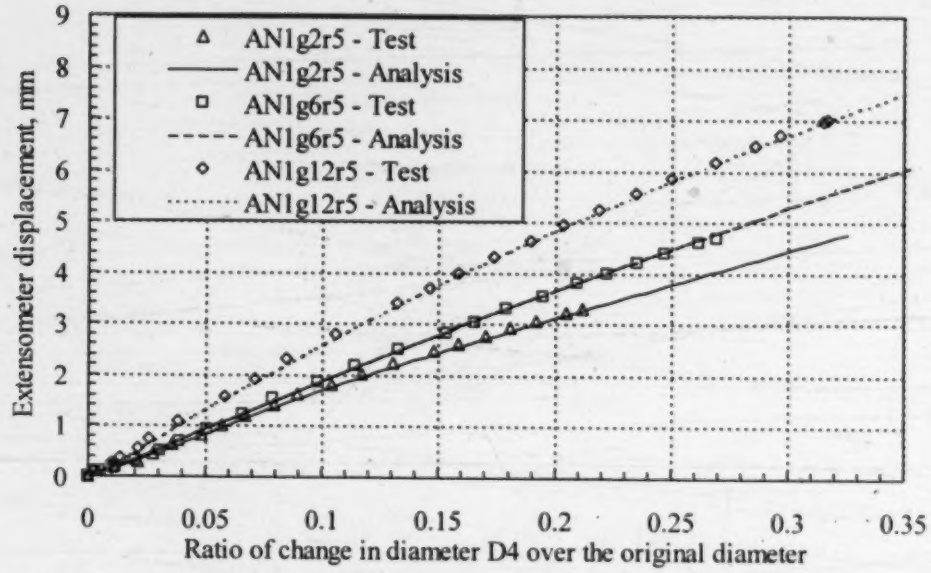

Figure 5.41 Measured and analytical extensometer displacement versus change in diameter D4 for AN specimens with gage length less than 12 mm and n = 1.0.

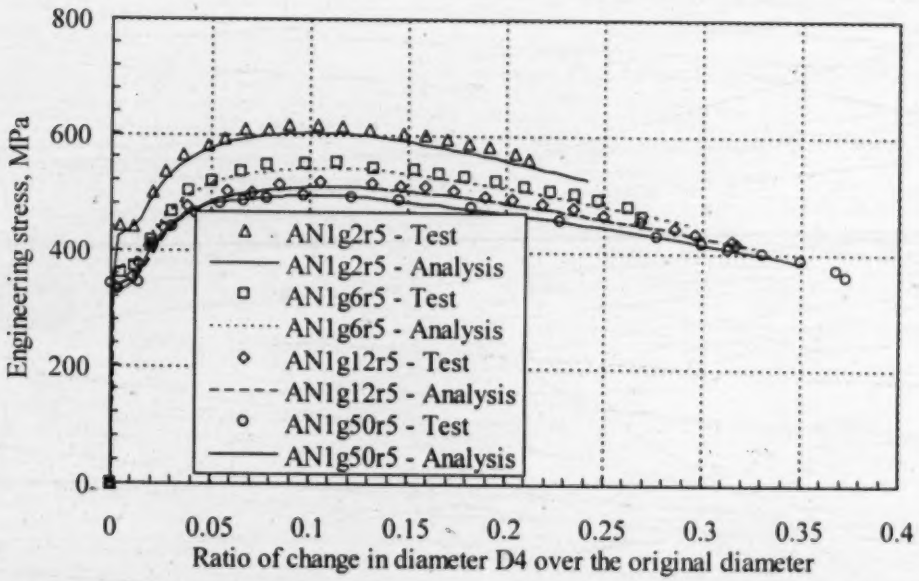

Figure 5.42 Measured and analytical stress versus change in diameter D4 for AN specimens with n = 0.5.

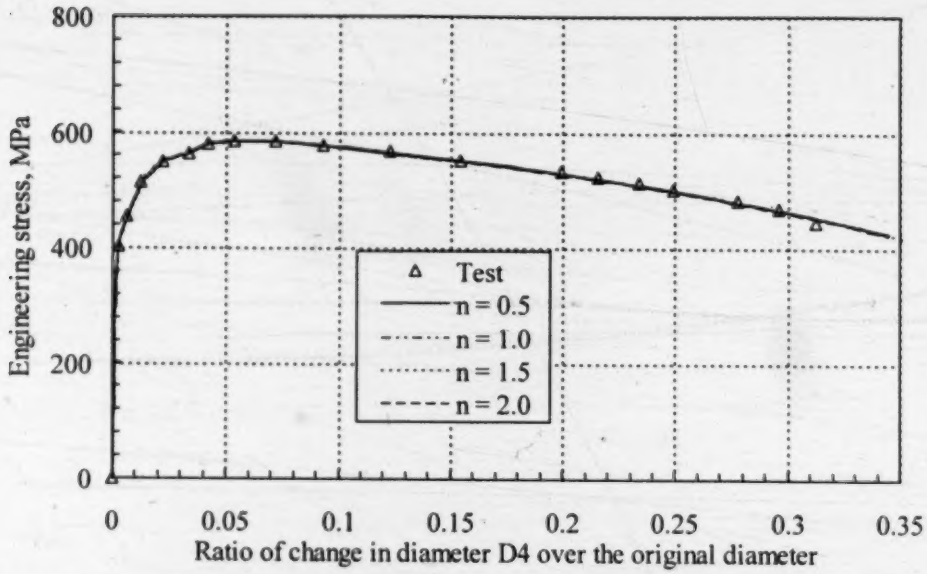

Figure 5.43 Measured and analytical stress versus change in diameter D4 for NM1g50r5.

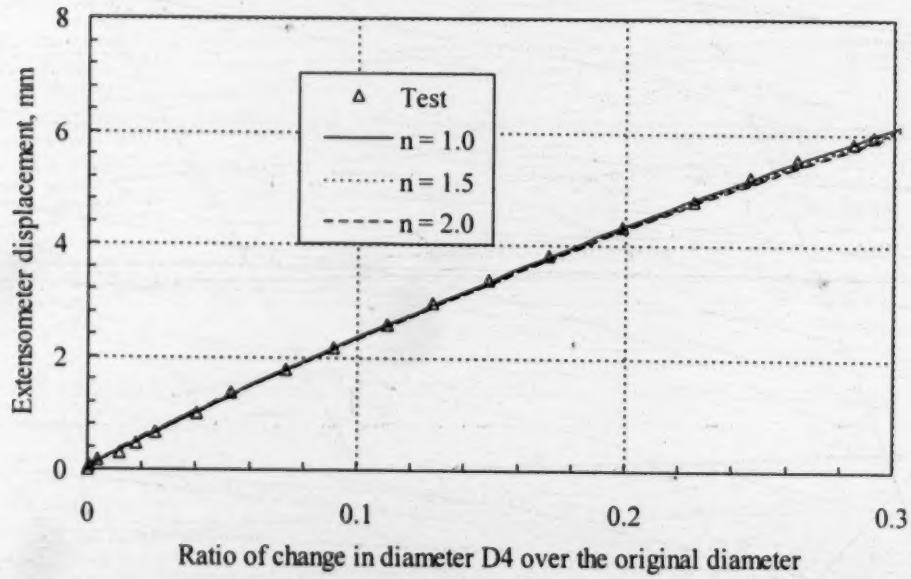

Figure 5.44 Measured and analytical extensometer displacement versus change in diameter D4 for NM1g12r5.

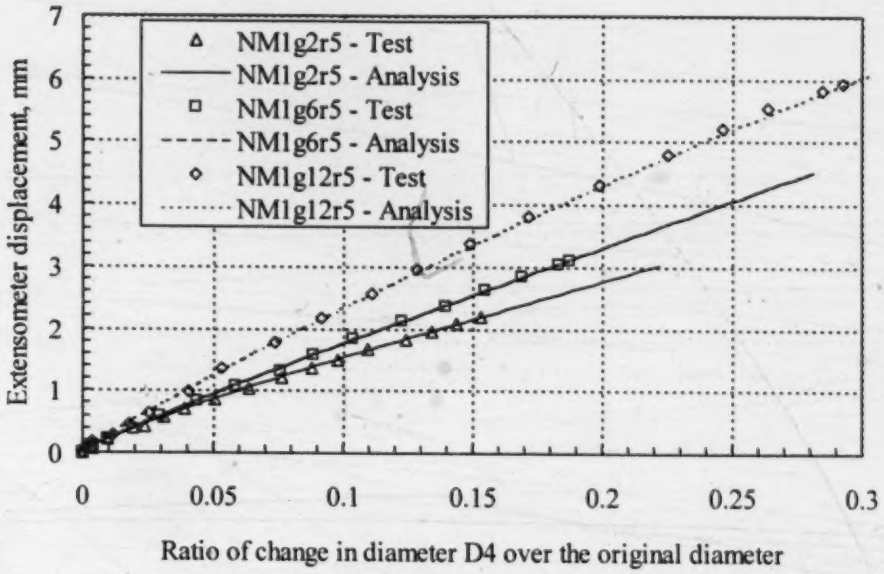

Figure 5.45 Measured and analytical extensometer displacement versus change in diameter D4 for NM specimens with gage length less than 12 mm and n = 1.5.

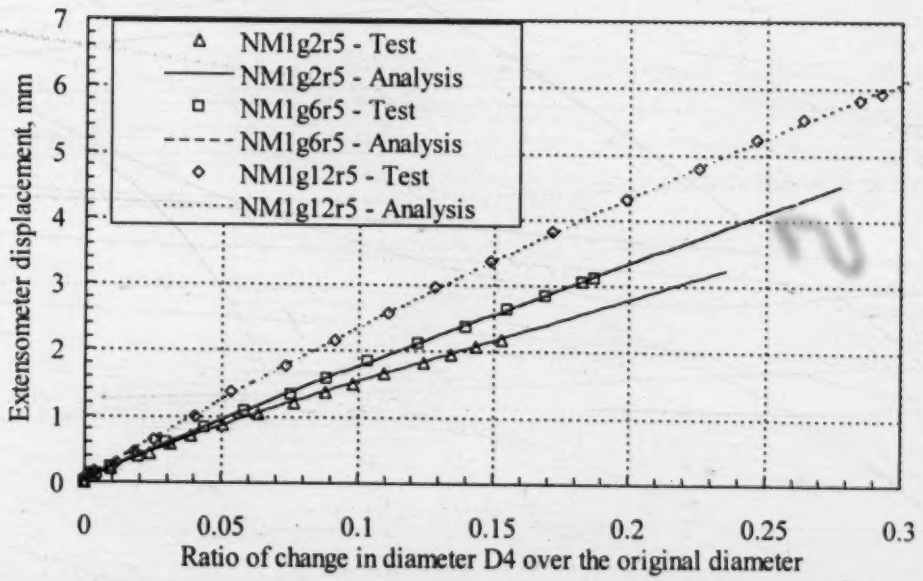

Figure 5.46 Measured and analytical extensometer displacement versus change in diameter D4 for NM specimens with gage length less than 12 mm and n = 1.0.

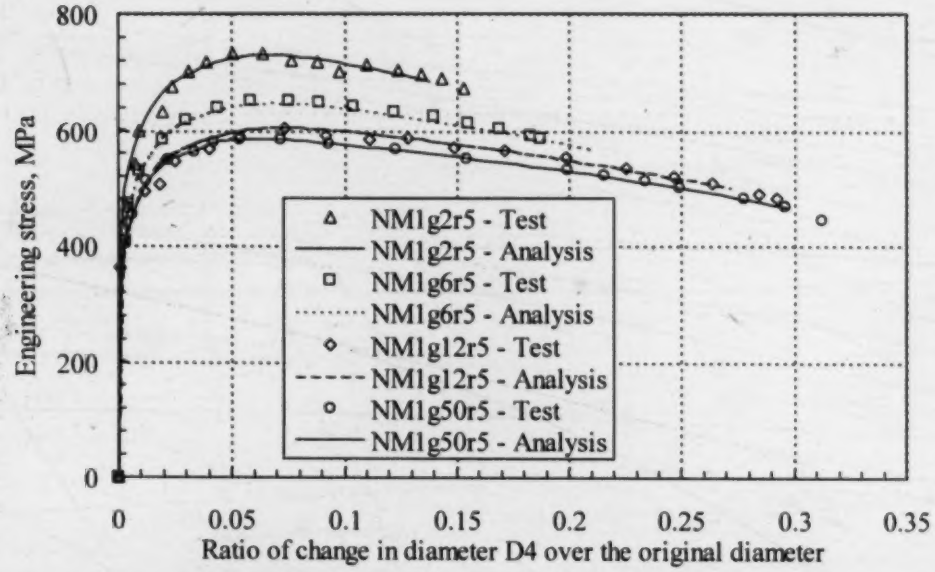

Figure 5.47 Measured and analytical stress versus change in diameter D4 for NM specimens with n = 1.5.

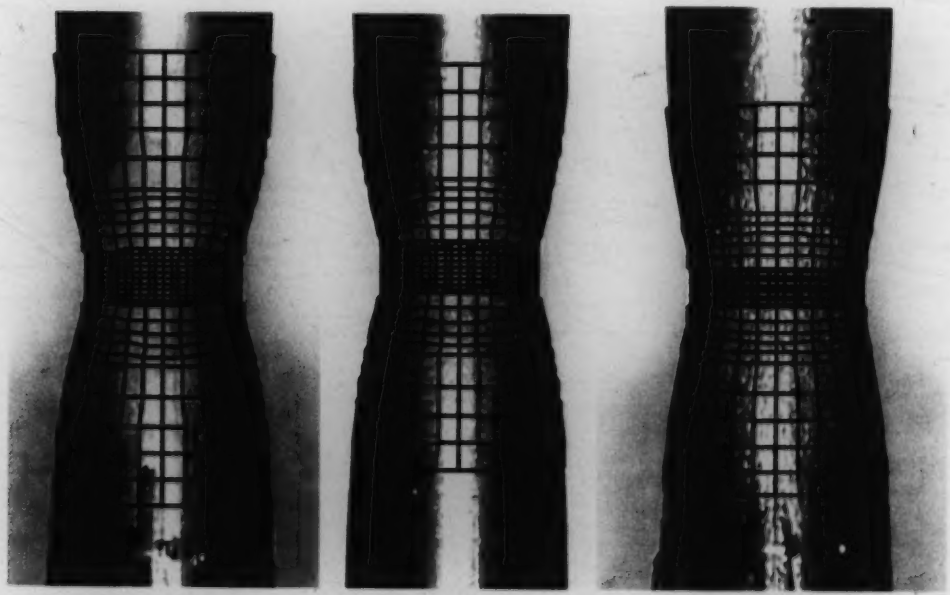

AS1g50r5, D4=8.63 mm AN1g50r5, D4=8.76 mm NM1g50r5, D4=9.76 mm

Figure 5.48 Superposition of the deformed mesh on the 50 mm gage length specimen at close to fracture.

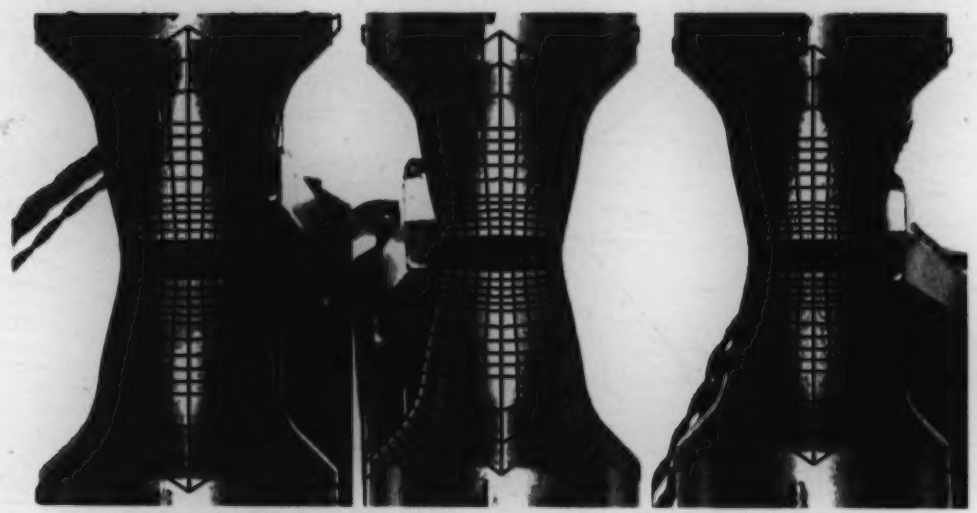

AS1g12r5, D4=9.48 mm AN1g12r5, D4=9.45 mm NM1g12r5, D4=9.93 mm

Figure 5.49 Superposition of the deformed mesh on the 12 mm gage length specimen at close to fracture.

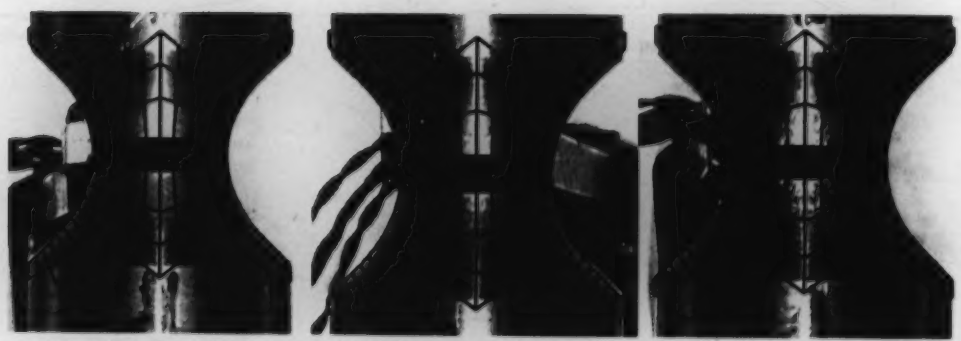

AS1g2r5, D4=11.01 mm AN1g2r5, D4=11.02 mm NM1g2r5, D4=11.87 mm

Figure 5.50 Superposition of the deformed mesh on the 2 mm gage length specimen at close to fracture.

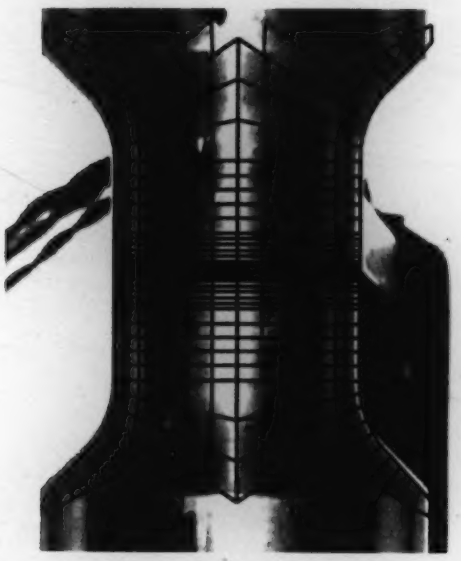

Figure 5.51 Superposition of the undeformed mesh on AS1g12r5 before any application of load.

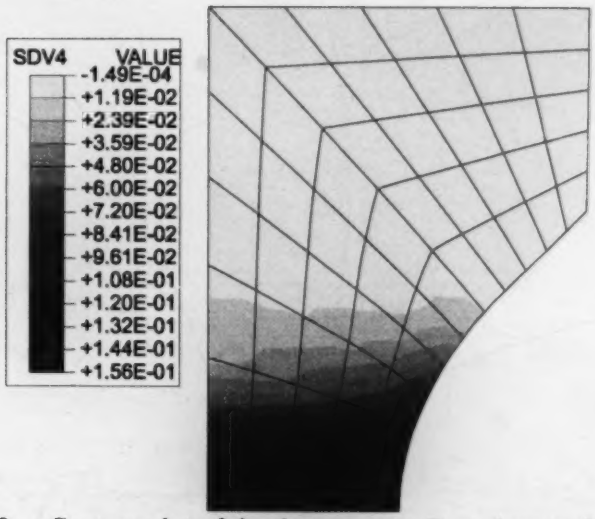

Figure 5.52 Contour plot of the damage state D at close to fracture for AS1g2r5.

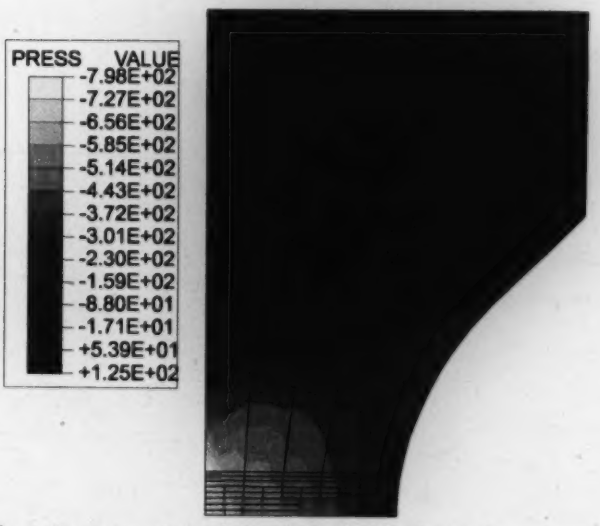

Figure 5.53 Contour plot of the negative hydrostatic pressure ($-\sigma_h$) at close to fracture for AS1g2r5.

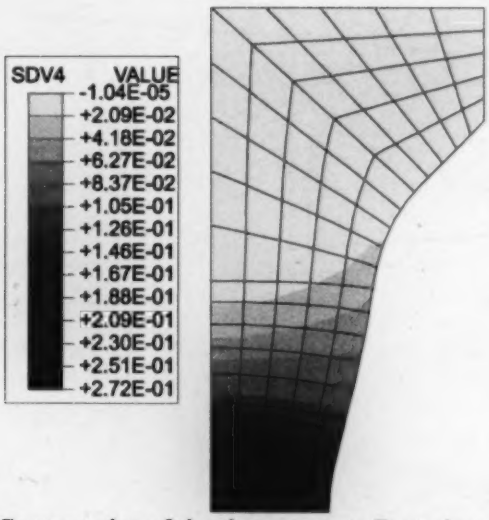

Figure 5.54 Contour plot of the damage state D at close to fracture for AS1g12r5.

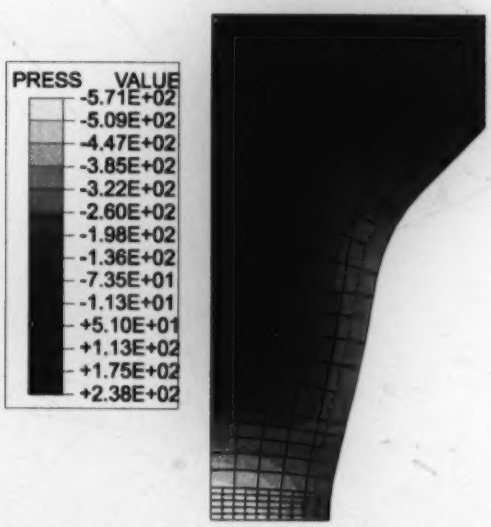

Figure 5.55 Contour plot of the negative hydrostatic pressure ($-\sigma_h$) at close to fracture for AS1g12r5.

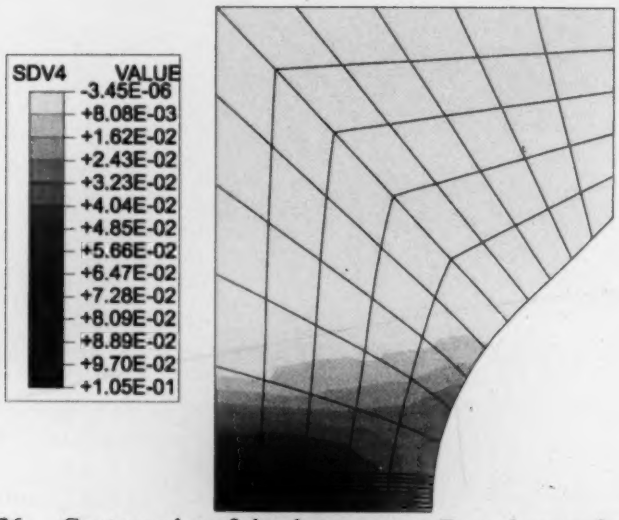

Figure 5.56 Contour plot of the damage state D at close to fracture for NM1g2r5.

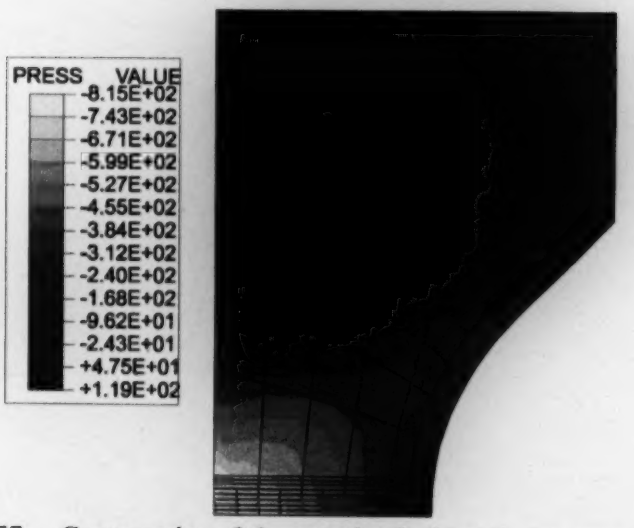

Figure 5.57 Contour plot of the negative hydrostatic pressure ($-\sigma_h$) at close to fracture for NM1g2r5.

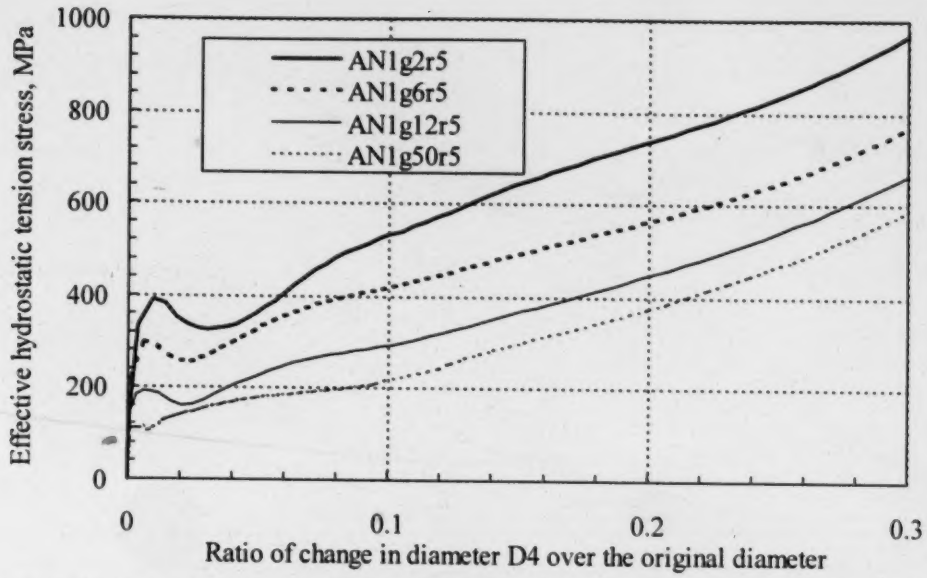

Figure 5.58 Analytical effective hydrostatic tension stress versus change in diameter D4 for AN heat treatment at the mid-length along the axis of the specimen.

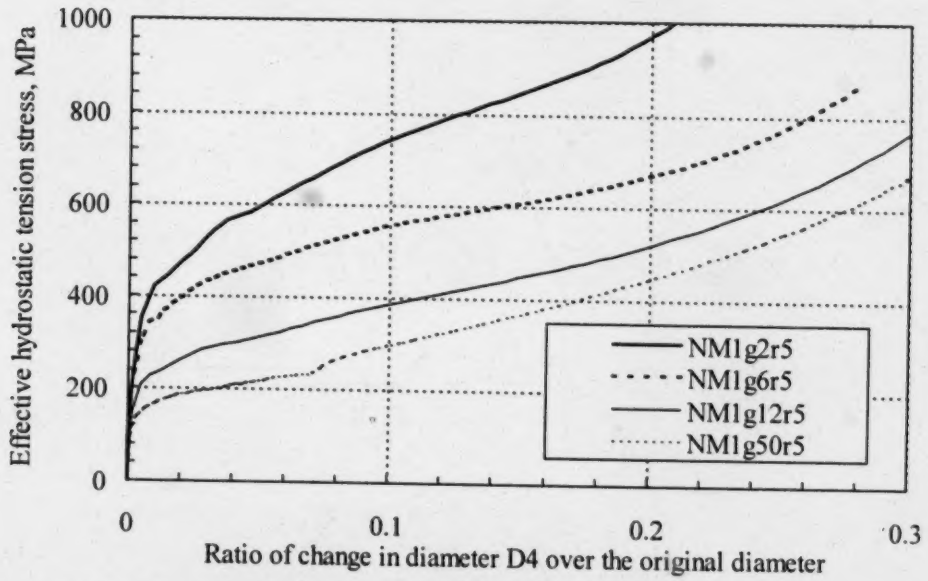

Figure 5.59 Analytical effective hydrostatic tension stress versus change in diameter D4 for NM heat treatment at the mid-length along the axis of the specimen.

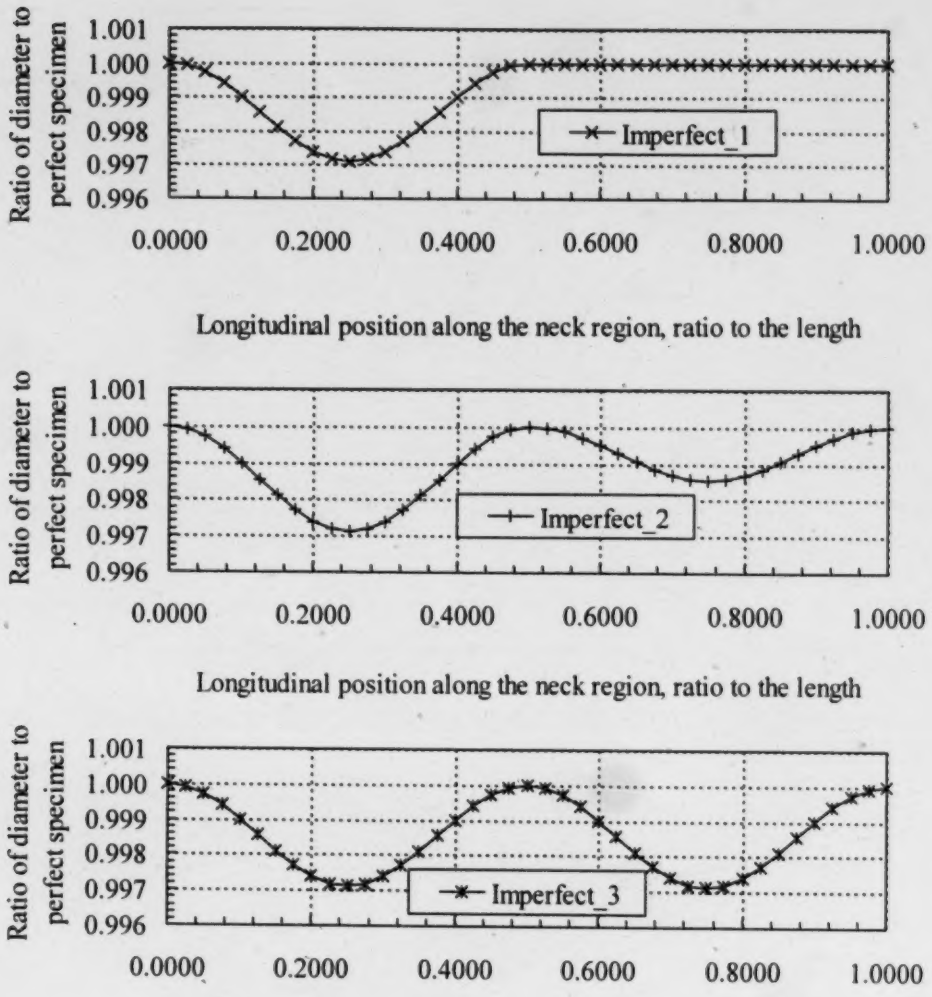

Figure 5.60 Patterns of imperfection.

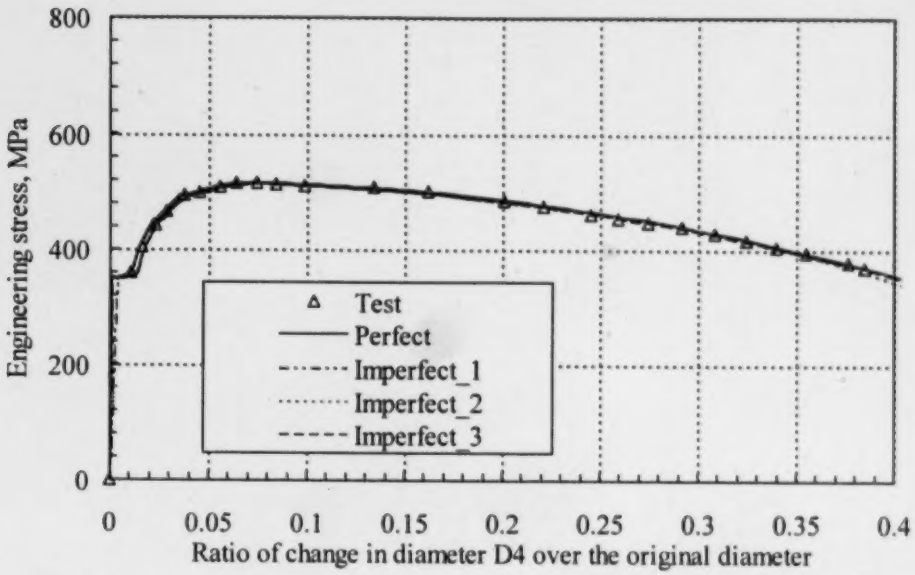

Figure 5.61 Stress versus change in diameter D4 for various imperfection patterns.

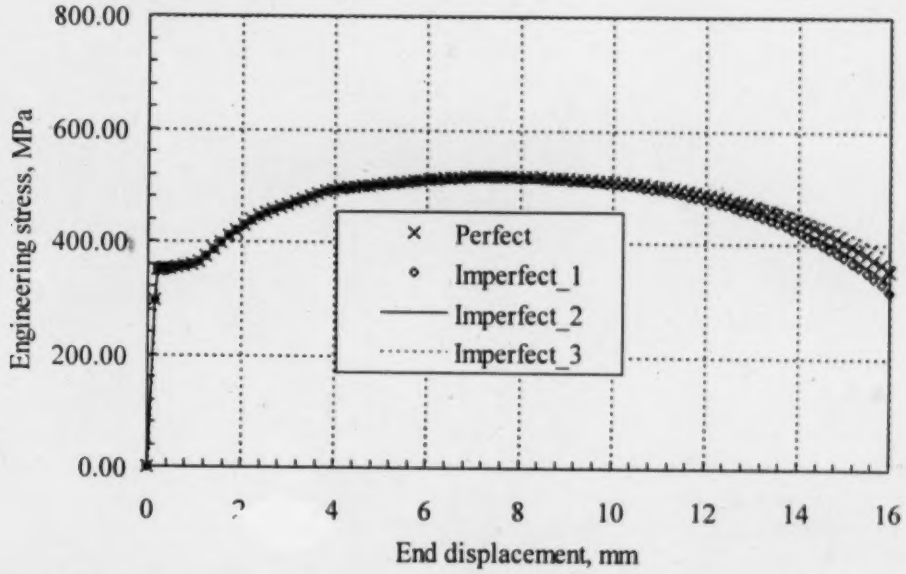

Figure 5.62 Stress versus change in end displacement for various imperfection patterns.

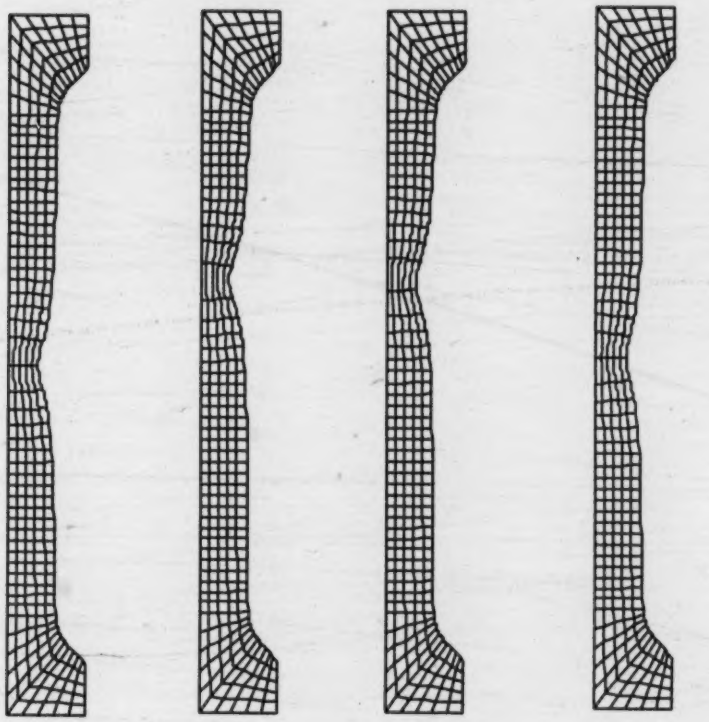

Figure 5.63 Deformed mesh for various imperfection patterns.

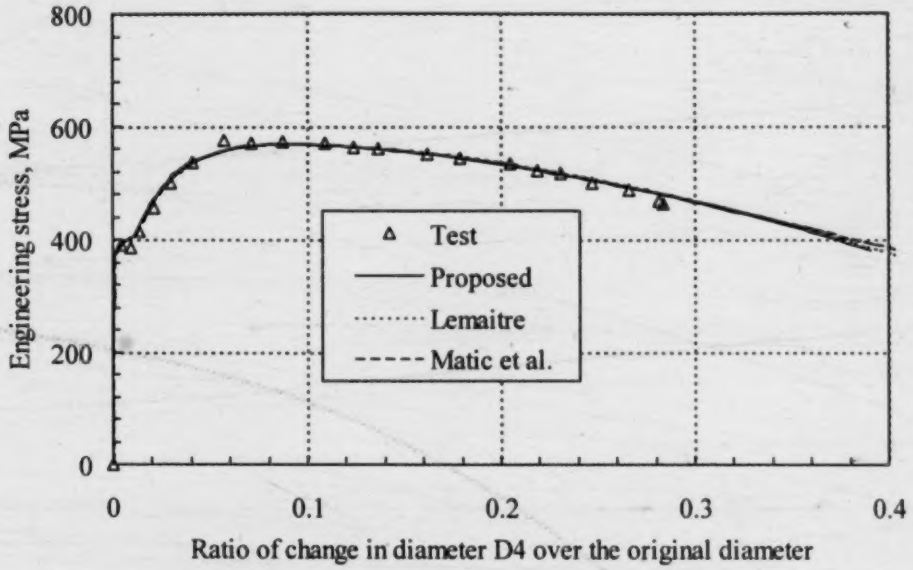

Figure 5.64 Measured and analytical stress versus change in diameter D4 with different material models for AN1g50r5.

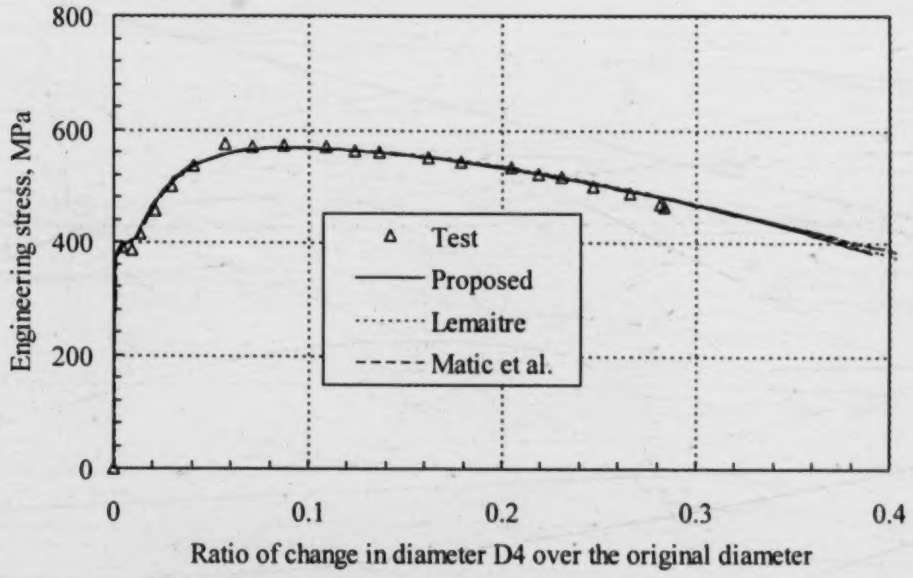

Figure 5.65 Measured and analytical stress versus change in diameter D4 with different material models for AS1g6r5.

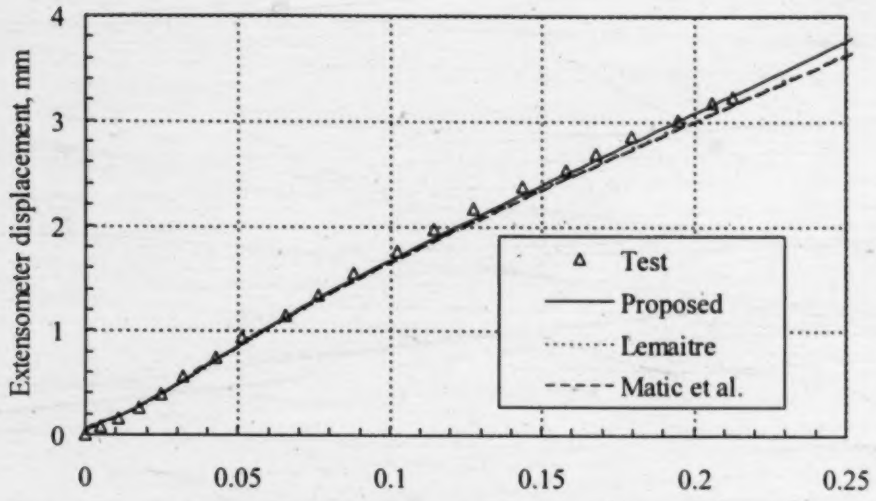

Figure 5.66 Measured and analytical extensometer displacement versus change in diameter D4 with different material models for AS1g2r5.

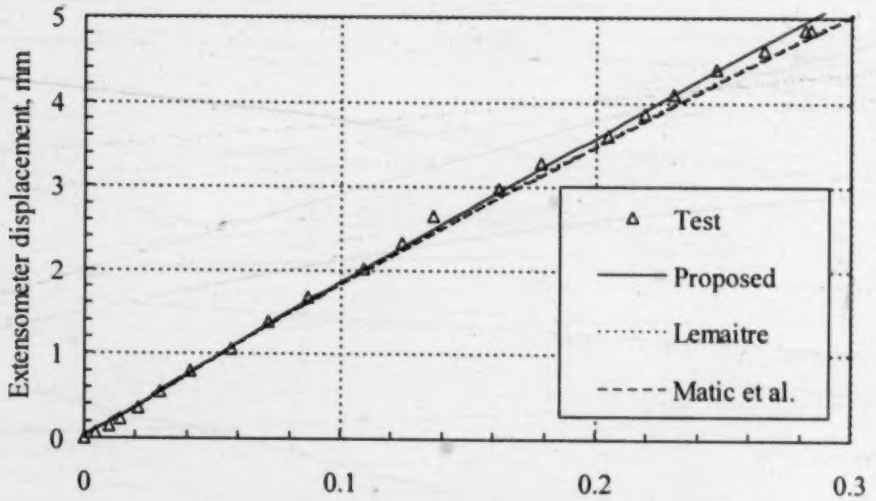

Figure 5.67 Measured and analytical extensometer displacement versus change in diameter D4 with different material models for AS1g6r5.

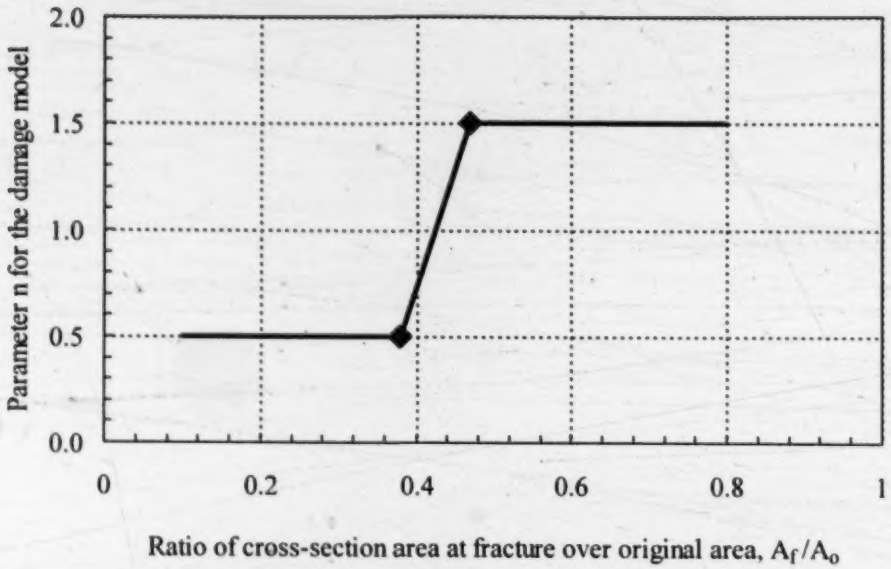

Figure 5.68 Choice of n based on final cross-section area of tension coupon test.

6 Application of the Damage Model

The ability to closely represent the behaviour of steel up to fracture enables a better prediction of the capacity and the response of a steel structure. The proposed damage model allows for the numerical testing of structural components, and provides a useful alternative to costly physical tests. This is especially useful in the prediction for a structural component where there is stress concentration. The stress concentration may be due to defects or discontinuities in the geometry. In these situations, the material at different points in the structure does not reach the ultimate strength simultaneously. Thus, it is essential that the actual behaviour up to the point of fracture be known so that the capacity can be analyzed accurately. In following sections, numerical simulations of slotted tubular tension member tests and machined corroded pipe tests are carried out to illustrate applications for the damage model.

In a tubular tension member test, end connections were fabricated by slotting the tube longitudinally and inserting a gusset plate, which was then welded to the tube using parallel longitudinal fillet welds. As a result, stress concentration occurs at the slotted end of the assembly. The level of stress concentration is dependent on the relative length of the weld to the circumference of the tubular member. Depending on the level of stress concentration, premature fracture at the slotted end may reduce the capacity and the ductility of the tension member. This type of connection is commonly used in steel structures for a tubular tension member. In a machined corroded pipe test, regions of the pipe were machined so as to reduce the wall thickness, and thereby simulate the effects of corrosion. This creates a weakened region in the pipe, thus induces stress concentration and a reduction in the overall ductility. In the test, the pipe was subjected to a combined axial load, internal pressure and bending moment to simulate conditions in the field.

The slotted tubular tension member tests by Cheng et al. (1998) carried out at the University of Alberta are used in comparison with the results of numerical simulation.

6.1 Numerical Simulation

In most tension coupon material tests conducted, only the load versus longitudinal deformation (or engineering stress versus engineering strain) relationship is measured. As demonstrated in Chapter 5, this measurement does not accurately capture the post

maximum load behaviour of the tension coupon test. Since the complete tension material test result is not available, an idealized stress versus change in cross-section area response for the material is used in the analyses. The idealization involves combining the test results of either the actual material or the material with same grade up to the peak load, and results from either AS, AN or NM heat treatment for the post peak response.

The commercial finite element package ABAQUS is used for the numerical simulation. For these tests, a 3D solid element is required to accurately model the necking and the triaxial state of stress in the ductile fracture process. However, modeling using a 3D solid element requires considerably more computing effort than using a finite strain shell element. Thus, a compromise is made regarding the accuracy of the modeling and the computer effort by using a shell element. Even though a finite strain shell element is able to capture the reduction in the thickness, it is unable to represent the triaxial state of stress that exists when necking starts. Furthermore at the junction of intersecting plates or shells, a triaxial state of stress exists but a shell element only considers normal stress in two directions. Thus, (3.22) for the critical damage limit D_c is modified to account for this discrepancy. In a shell element the hydrostatic stress is given by

$$\sigma_h = \frac{1}{3}(\sigma_{11} + \sigma_{22}) \tag{6.1}$$

where σ_{33} is zero. Substituting (6.1) into (3.22), the critical damage limit D_c is given by

$$D_c = \frac{9D_o}{(\sigma_{11} + \sigma_{22})^2}. \tag{6.2}$$

By assuming that the actual σ_{33} in a shell element is an average of $(\sigma_{11} + \sigma_{22})$, (6.2) therefore becomes

$$D_c = \frac{4}{9} \times \frac{9D_o}{(\sigma_{11} + \sigma_{22})^2}. \tag{6.3}$$

Back substituting (6.1) into (6.3), the modified critical damage limit D_c to be used in a shell element where there is a considerable out-of-plane normal stress is given by

$$D_c = \frac{4D_o}{9(\sigma_h)^2}. \tag{6.4}$$

6.2 Slotted Tubular Tension Members

End connections for a tubular tension member are normally created by slotting the tube longitudinally and inserting a gusset plate, which is then welded to the tube using parallel longitudinal fillet welds. However, the overall strength of the tubular tension member may be affected by the shear lag phenomenon at the connection depending on the length of the fillet weld. Using the end connection configuration, the tests for the slotted tubular tension member were conducted by pulling the gusset plate longitudinally (Cheng et al., 1998). Dimensions for specimens tested are shown in Figure 6.1. All specimens have fillet weld continued around the plate at the slotted end except for PWC1.

The material properties and parameters used in the numerical analyses are shown in Table 6.1. They are obtained through the numerical simulation of idealized stress versus change in cross-section dimension curves of tension coupon tests for the HSS section and the gusset plate. The idealized stress versus change in cross-section dimension curves are shown in Figures 6.2 and 6.3. The material properties of AS heat treatment are used as the basis to form the idealized stress versus change in cross-section dimension for both the HSS section and the gusset plate. For example, using (5.14) and the actual stress versus strain data of the tension coupon test of HSS 219 x 8.0 up to the peak load, the graph for HSS 219 x 8.0 is plotted in Figure 6.2. This curve is then scaled by the ratio of the ultimate strength of AS material to HSS 219 x 8.0 forming the ascending segment of the idealized curve. The descending segment of the idealized curve is assumed to follow the response of AS1g50r5, and the point of fracture of the AS material. The idealized curve for the 20 mm gusset plate is also obtained using the similar method.

Welding usually reduces the fracture toughness of the material. Therefore, the D_o at the weldment and the heat-affected zone is arbitrary assumed to be one-ninth that of the virgin material. Based on the analogy drawn on (3.21) and (3.22) where K_{IC} is the plane strain fracture toughness, one-ninth D_o is equivalent to one-third of the fracture toughness of the original material. Thus, the fracture toughness of the weldment and the heat-affected zone is assumed to be one-third that of the virgin material. The

corresponding fracture points on the idealized tension coupon load-deformation curves are shown in Figures 6.2 and 6.3. Due to the uncertainty of the fracture toughness at the weldment and the heat-affected zone, numerical analyses with different D_o may be carried out in a parametric study.

To numerically simulate the test, a four-node finite strain shell element S4 is used to model both the tube and the plate. Only one-eighth of the specimen is modeled. The critical damage limit D_c based on (6.4) is used in the analyses. The extra thickness due to the weld is distributed evenly between the plate and the tube according to the tributary width. The heat-affected zone is assumed to extend half a weld size beyond the toe of the weld. Thus for a fillet weld of 6 mm, the heat-affected zone is 3 mm. The typical finite element mesh and the thickening at the weld are shown in Figure 6.4. Since the ultimate tensile strength of an idealized HSS section is different from that of the actual material, the load from the numerical solution is scaled according to the ultimate tensile strength ratio of the actual material to the AS material before comparing to the test results. The actual measured ultimate tensile strength of the material is listed in Table 6.2 together with the value for the AS heat treatment.

The comparisons of the test and predicted results are listed on Tables 6.3 and 6.4. Based on the parameters selected, the numerical solution is able to give a reasonable prediction of the test results. When the weld does not go around the end of the plate (PWC1) or the weld length is short relative to the circumferential length of the tube (SPEC2), fracture occurred at the slotted end. This occurrence is reflected in the predicted location of fracture. In general, the predicted deformation at fracture is within 30% of the test value, with the exception of PWC7. The test to predicted peak load is within 4%. For illustration, Figure 6.5 shows the actual and predicted deformed shape when fracture is at the mid-length.

From the analytical results, a better understanding of the behaviour of the slotted tubular tension member is obtained. Due to the shape of the HSS section, the gusset plate restrains the tube from contracting circumferentially as the tube elongates. As a result, hoop tension stress develops at the slotted end as indicated in Figures 6.6 and 6.8. The hoop stress has an effect of stiffening the tube at the slotted end as compared to the mid-length. Figure 6.7 shows the stress concentration at the end of the fillet weld for

PWC1 where fracture eventually occurred. Since the weld did not continue around the gusset plate for PWC1, the net section area at the slotted end is smaller than the rest of the tube. Thus regardless of the stiffening effect of the hoop tension stress, fracture occurred at the slotted end for PWC1. Even when the weld continues around the plate, there is still considerable stress concentration at the slotted end as shown in Figure 6.8. Thus depending on the ratio of weld length to the circumferential length of the tube, a high stress concentration may result in fracture at the slotted end, such as SPEC2. However, if the stress concentration is not very high, the stiffening effect of the hoop tension stress will eventually cause necking and fracture to occur at the mid-length as shown in most of the tests. The agreement is also quite good between the test and predicted load-deformation curves. These comparisons are shown in Figures 6.9 to 6.12.

6.3 Machined Corroded Pipes

In the field, most pipes experience corrosion. Corrosion reduces the strength of steel structures. Numerical tests are carried out to study the effect of corrosion on X70 (minimum yield strength of 482 MPa (70 ksi)) 609.6 mm diameter pipes. In order to simulate corrosion, regions of the pipe were machined to a thinner wall thickness. The loading for the pipe test is shown in Figure 6.13. The loading has been used extensively by the pipeline research group at the University of Alberta (DelCol et al., 1998 and Mohareb et al., 1994). Collars were provided at the ends of the test specimens to minimize the end effects. During the test, the axial load and the internal pressure were kept constant while the ends were subjected to an increasing bending rotation. This is to simulate the increasing curvature due to soil movement. The following average stresses, calculated based on the undeformed dimension of the pipe specimen with no corrosion, are generated by the combined applied axial load and internal pressure:

- An axial tensile stress of 0.24 σ_u where σ_u is the ultimate tensile strength of the pipe.
- A hoop tensile stress of 0.64 σ_u.

All the tests were carried out with the same axial load and internal pressure. The geometry of the specimens and their designation are tabulated in Table 6.5. Three test specimens are considered in the numerical simulation. These specimens have three corrosion shapes: no corrosion, circumferential groove and square patch. Sketches of

corrosion patterns for specimens II and III are shown in Figures 6.14 and 6.15. There are altogether six numerical simulations carried out, two for each specimen. A four-node finite strain shell element S4 is used to model the pipe. Only half the pipe is modeled. No geometry imperfection is considered in the modeling. Some of the finite element meshes are shown in Figures 6.16 to 6.18. The differences between the finite element models are listed below.

- IA - According to Table 6.5.
- IB - Same as IA, but the thickness over the length of a pipe diameter at the mid-length is reduced to 98% of the measured average thickness.
- IIA - According to Table 6.5.
- IIB - Same as IIA, but the thickness is increased to 6.6 mm at a 3.4 mm wide longitudinal strip along the machined corrosion boundary.
- IIIA - According to Table 6.5.
- IIIB - Same as IIA, but the thickness is increased to 9.40 mm at a 5.3 mm wide longitudinal strip along the machined corrosion boundary.

Similar to the slotted tubular tension member tests, properties and parameters used in the numerical analyses are obtained through the numerical simulation of an idealized stress versus change in cross-section dimension curves for a pipe tension coupon test. The load versus deformation curve of NM1g50r5 is used as the basis to form the idealized load-deformation curve for the tension coupon test because its ultimate strength is close to that of the pipe. Using the ascending segment of the test data for a X70 pipe tension coupon by DelCol et al. (1998), the idealized load-deformation curve is shown in Figure 6.19. The actual ultimate tensile strength of the pipe and the material for NM material are tabulated in Table 6.6. The end moment from the numerical solution is scaled according to the ultimate tensile strength ratio of the actual material to the NM material before plotting. Properties and parameters used in the numerical analyses are listed in Table 6.7.

In this discussion, the pipe specimen without any machined corrosion is referred to as the plain pipe. The predicted deformed shapes at failure are shown in Figure 6.20. For the pressurized plain pipe, multiple buckling waves are formed during the test until one wave takes over and dominates the deformation. Since no geometric imperfection is

considered in the numerical modeling, the greatest disturbance for a pressurized plain pipe occurs at specimen ends because the collar restrains the pipe from expanding. Thus two symmetric buckles formed at the end of the pipe for IA. In order for the numerical solution to produce bulging in the middle, the modeling scheme for IB is adopted. Figure 6.21 shows the predicted moment-curvature curves for IA and IB. For a pressurized plain pipe, the most highly stressed point in the specimen is at the crest of the bulge along the extreme compression face. This is indicated in the contour plots in Figures 6.22 and 6.23. The state of damage is also the greatest at that location. However at the end of the analysis, the state of damage along the pipe is not sufficiently high to form any crack. Point 1 in Figure 6.23 marks the stage when the analysis for IB is stopped.

For II and III, there is a weakened area in the pipe for bulging to take place. Thus, no special modification is required in the numerical simulation to produce failure at the mid-length of the pipe. The measured and predicted moment versus curvature graphs are shown in Figures 6.24 to 6.25. Point 1 in Figures 6.24 and 6.25 marks the stage where the critical damage limit D_c, calculated using (6.4), is first exceeded in IIA and IIIA respectively. They are the loading stages corresponding to the contour plots in Figures 6.26 to 6.29. However, all the predicted curves show a sudden drop at the end. This is due to the inability of the shell element to model the triaxial state of stress involved in the necking process. As the pipe wall starts to neck, the increased hydrostatic tension stress that develops stiffens that part of the pipe wall. This reduces the rate of localization of the deformation that may otherwise occur. Comparing IIB to IIA in Figure 6.24, a small increase in the thickness along the boundary gives a further extension on the curvature before the moment drops. This is similar to the stiffening effect caused by an increase in the hydrostatic tension stress. In Figures 6.24 and 6.25, the instant of fracture, which is marked on the graphs, corresponds to the critical damage limit D_c being reached, based on both (3.22) and (6.4). The instant of fracture predicted by the damage model is equivalent to the appearance of the surface crack on the pipe. In Figures 6.24 and 6.25, the predicted appearance of the surface crack by (6.4) occurs at a much earlier curvature than by (3.22). In (6.4), the out-of-plane normal stress is assumed to be the average of the in-plane normal stresses. But there is little out-of-plane stress at

the surface of the pipe. Thus, (6.4) is more suitable for situations similar to the slotted end of the tubular tension member where there is a large out-of-plane stress due to the geometric configuration. Consequently instead of using (6.4), an 80% or 90% of (3.22) may be more suitable for predicting fracture for a plate with no out-of-plane attachment.

IIA, IIB, IIIA and IIIB predict cracks to appear along the longitudinal boundary of the machined corrosion. It can be seen in Figures 6.26 to 6.28, the state of damage and the von Misés stress are the largest at the crest along the longitudinal boundary of the machined corrosion. The reduction in the wall thickness of the pipe is also the largest at that location as depicted in Figure 6.29. In contrast to I, the critical point in II and III is not at the crest of the bulge along the extreme compression face even though the magnitude of the buckle is the largest there. For II and III, the critical location is at the crest along the longitudinal boundary because the constraint provided by material outside the machined corrosion prevents the bulge from deforming freely, thus inducing a greater stress.

This exercise provides a good illustration of another possible application of the proposed model. However, with a shell element, the numerical analysis cannot properly model the pipe wall thickness reduction. Thus if possible, a 3D solid element should be used in the numerical analysis.

Table 6.1 Material properties and parameters used in the analyses for the slotted tubular tension member tests.

Elastic modulus = 215000 MPa		Poisson's ratio = 0.3 $\varepsilon^{p}_{eq_c} = 0.0$	
Plate		HSS section	
n = 0.5 $s^{-n} = 0.22$ $D_o = 107800$ (MPa)^2 for the rest of the plate. $D_o = 12000$ (MPa)^2 for the weldment and the heat affect zone.		n = 0.5 $s^{-n} = 0.22$ $D_o = 110300$ (MPa)^2 for the rest of the plate. $D_o = 12300$ (MPa)^2 for the weldment and the heat affect zone.	
True plastic strain, mm/mm	Effective true stress, MPa	True plastic strain, mm/mm	Effective true stress, MPa
0.00000	350	0.00000	414
0.00143	351	0.00400	416
0.00592	353	0.00651	450
0.02050	369	0.01300	483
0.02843	418	0.02787	509
0.04062	465	0.04253	525
0.05358	496	0.05697	540
0.07163	537	0.07119	554
0.09004	556	0.08520	568
0.10959	579	0.09900	579
0.12966	600	0.11261	591
0.15078	617	0.15065	618
0.17080	630	0.17067	631
0.20206	649	0.20191	650
0.24128	674	0.24112	675
0.32879	730	0.32859	731
0.36293	749	0.36272	750
4.00000	2820	4.00000	2825

Table 6.2 Ultimate tensile strength of the materials for slotted tubular tension member tests.

Material	Static ultimate strength, MPa
HSS 102 x 6.4	449
HSS 102 x 4.8	451
HSS 219 x 8.0	431
10 mm gusset	474
20 mm gusset	476
AS heat treatment	516

Table 6.3 Test and predicted fracture location.

Specimen	Fracture location	
	Test	Analysis
PWC1	Slotted end	Slotted end
PWC2-PWC4	Mid-length	Mid-length
PWC5-PWC7	Mid-length	Mid-length
SPEC1	Mid-length	Mid-length
SPEC2	Slotted end	Slotted end

Table 6.4 Test and predicted results of the slotted tubular tension member tests.

Specimen	Maximum load, kN			Maximum deformation[1], mm		
	Test	Analysis	Test / Analysis	Test	Analysis	Test / Analysis
PWC1	829.8	831.3	1.00	34.3	45.0	0.76
PWC2	868.6	847.6	1.02	134.7	128.9	1.04
PWC3	849.4	847.6	1.00	137.3	128.9	1.07
PWC4	874.8	847.6	1.03	141.9	128.9	1.10
PWC5	644.7	622.7	1.04	98.5	136.3	0.72
PWC6	634.0	622.7	1.02	102.6	136.3	0.75
PWC7	631.0	622.7	1.01	76.4	136.3	0.56
SPEC1	2160.0	2148.0	1.01	128.2	150.1	0.85
SPEC2	2138.6	2126.6	1.01	54.2	48.0	1.13

[1] Maximum deformation are from LVDT2 in PWC1-PWC7 and from LVDT3 in SPEC1 and SPEC2.

Table 6.5 Pipe dimensions.

Specimen	Corrosion shape	Machined corrosion geometry		
		Axial length, mm	Circumferential length, mm	Remaining thickness, mm
I	No corrosion	-	-	-
II	Circumferential groove	64	305	6.30
III	Square patch	305	305	9.20
General pipe geometry Outside diameter = 609.6 mm Average thickness = 12.7 mm				

Table 6.6 Ultimate tensile strength of the pipe.

Material	Static ultimate strength σ_u, MPa
Pipe	603
NM heat treatment	584

Table 6.7 Material properties and parameters used in the analyses for the machined corrosion pipe.

Elastic modulus = 202000 MPa	Poisson's ratio = 0.3	$\varepsilon^{p}_{eq_c} = 0.0$
Pipe		
$n = 1.5$ $s^{-n} = 0.08$ $D_o = 55900\ (MPa)^2$		
True plastic strain, mm/mm	Effective true stress, MPa	
0.00000	387	
0.00021	394	
0.00049	439	
0.00109	469	
0.00186	487	
0.00271	499	
0.00508	519	
0.00832	535	
0.01521	553	
0.02197	569	
0.03628	594	
0.05513	617	
0.07279	632	
0.10439	654	
0.14454	684	
0.18648	701	
4.00000	2329	

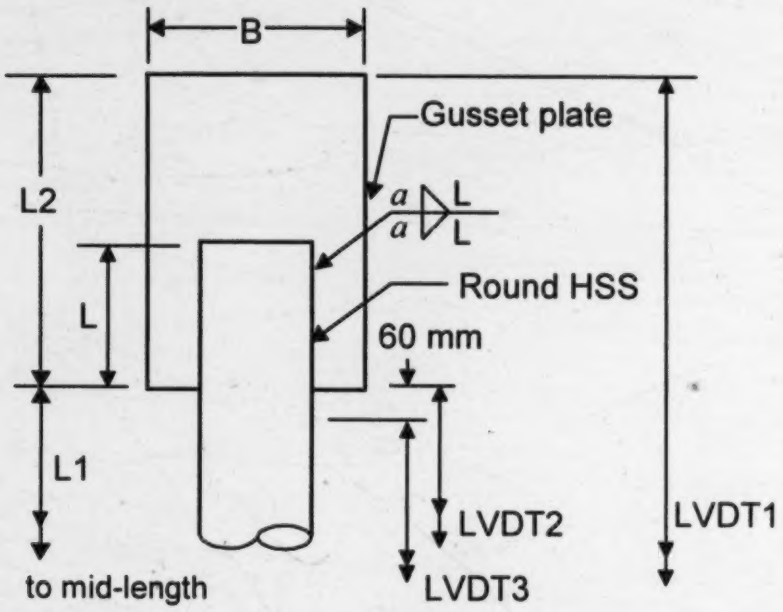

Specimen	HSS tube size (mm x mm)	Gusset width B, mm	L_1, mm	L_2, mm	L, mm	Weld size *a*, mm
PWC1[1]	102 x 6.4 (101.58 x 6.32)	230	330	350	170	6
PWC2-PWC4	102 x 6.4 (101.58 x 6.32)	230	330	350	170	6
PWC5-PWC7	102 x 4.8 (101.73 x 4.53)	200	350	300	150	5
SPEC1	219 x 8.0 (219.69 x 7.45)	440	345	750	345	10
SPEC2	219 x 8.0 (219.69 x 7.45)	440	345	680	275	10

[1] Welding did not continue around the gusset plate at the end of the slot.

Figure 6.1 Dimensions for the slotted tubular tension member test.

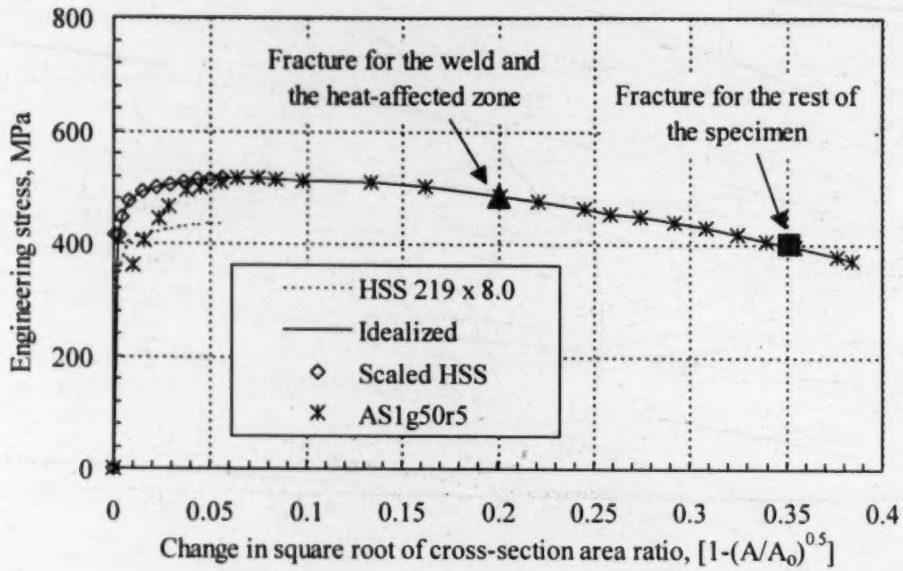

Figure 6.2 Idealized stress versus change in cross-section for the HSS section tension material test.

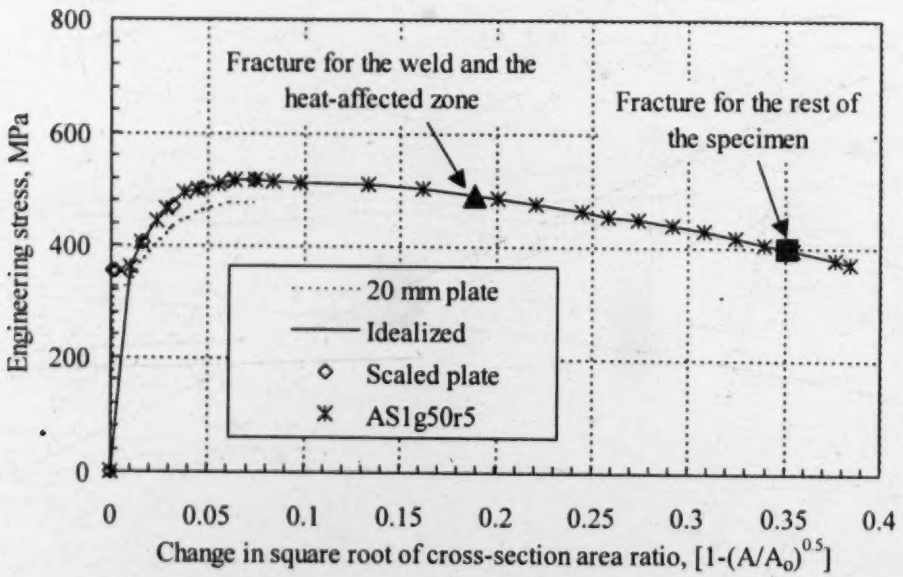

Figure 6.3 Idealized stress versus change in cross-section for the gusset plate tension material test.

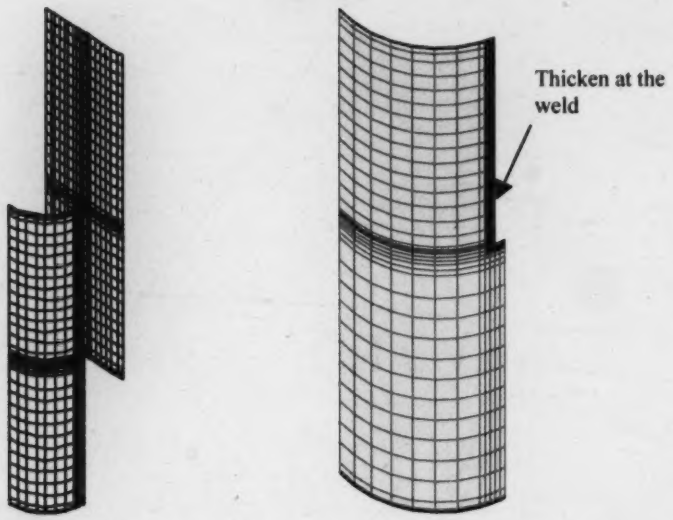

Figure 6.4 Typical finite element mesh for modeling slotted tubular tension member tests.

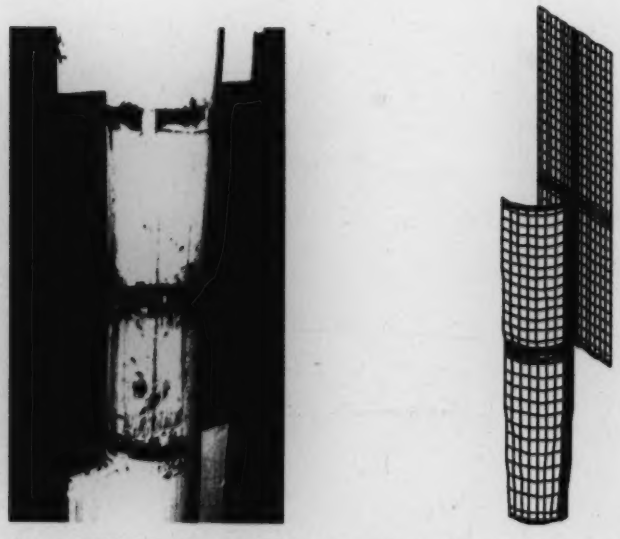

Figure 6.5 Specimen SPEC1, the typical test and predicted deformed shape for fracture at the mid-length of the specimen.

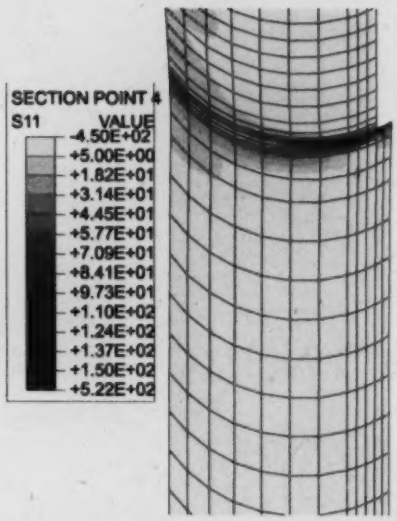

Figure 6.6 Contour plot of the hoop stress on the HSS section for PWC1.

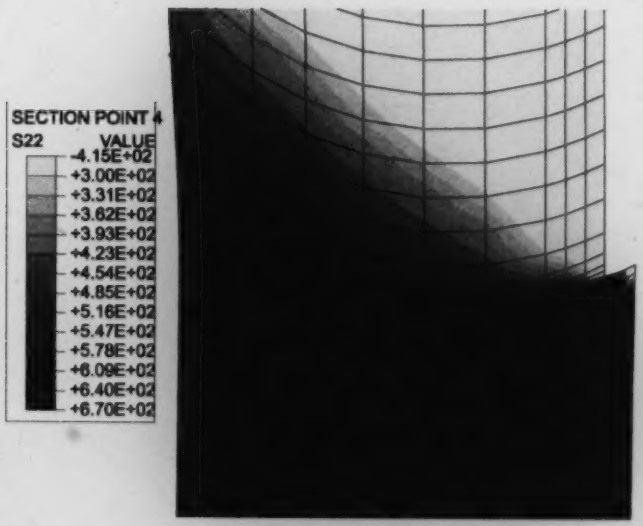

Figure 6.7 Contour plot of the longitudinal stress on the HSS section for PWC1.

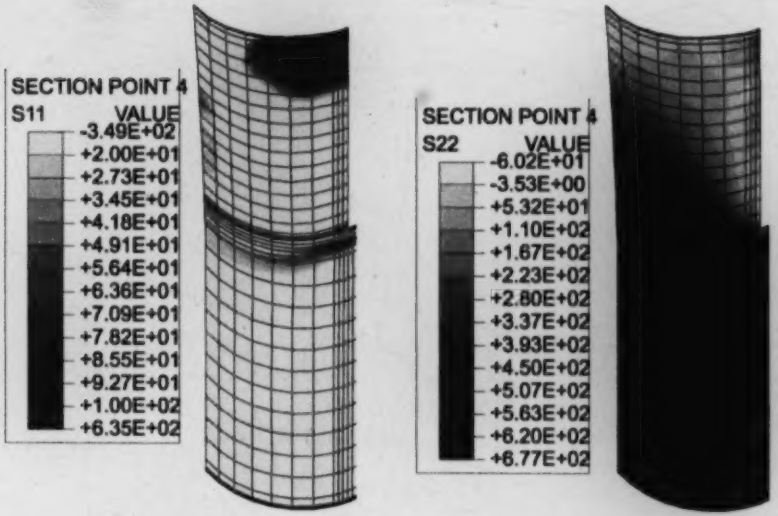

Hoop stress Longitudinal stress

Figure 6.8 Stress contour plot on the HSS section for SPEC2.

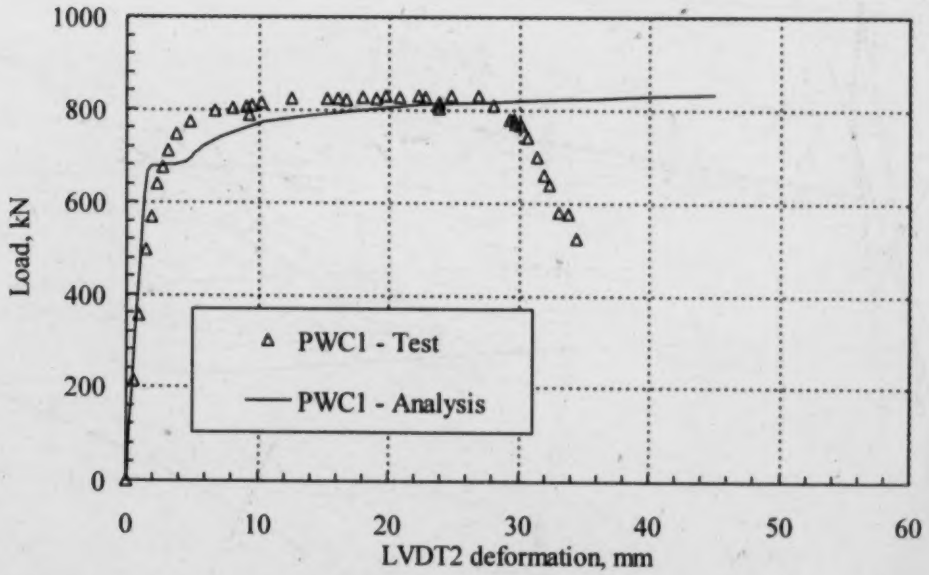

Figure 6.9 Test and predicted load versus deformation curve for PWC1.

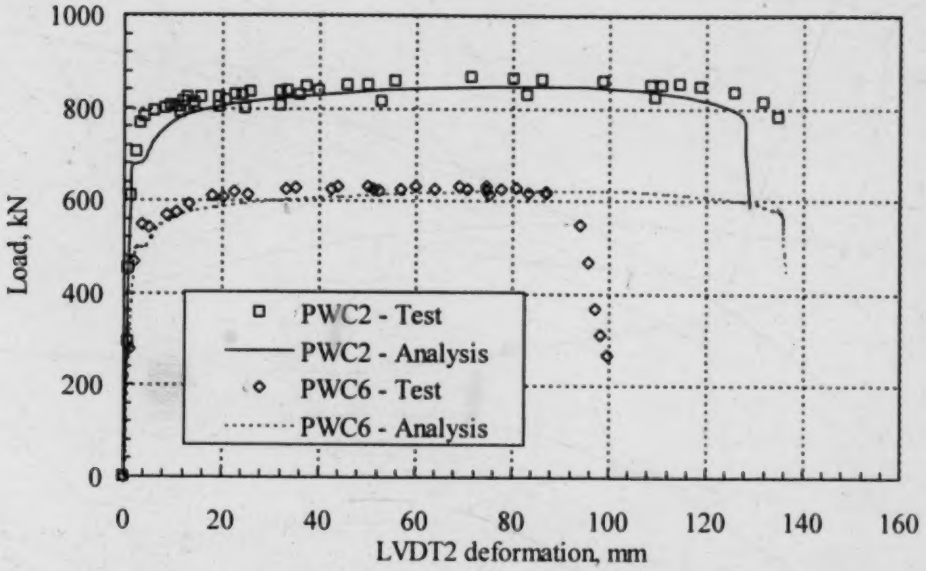

Figure 6.10 Test and predicted load versus deformation curve for PWC2 and PWC6.

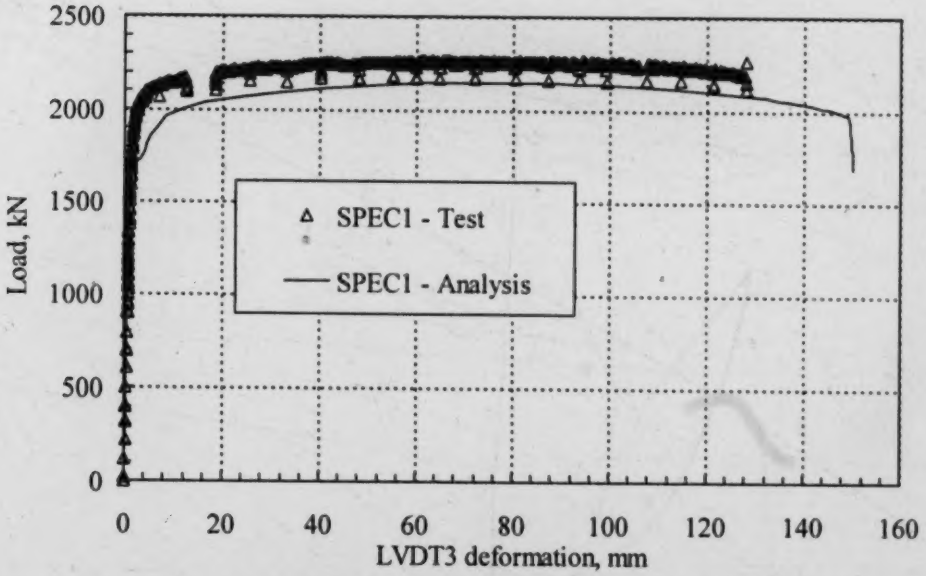

Figure 6.11 Test and predicted load versus deformation curve for SPEC1.

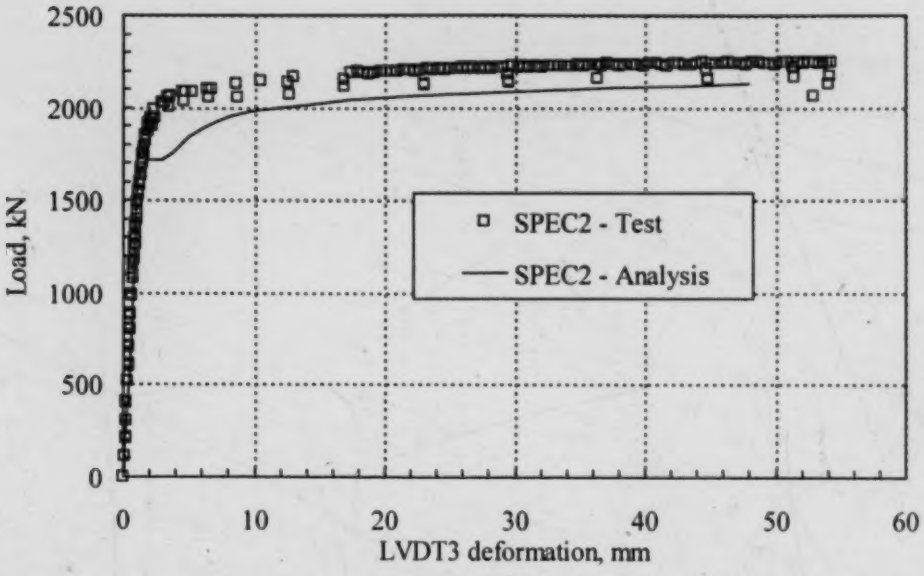

Figure 6.12 Test and predicted load versus deformation curve for SPEC2.

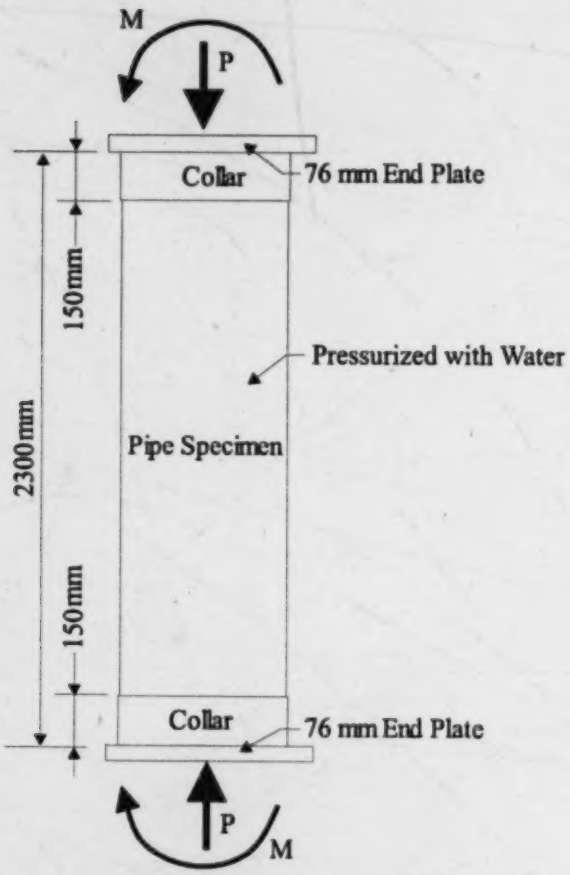

Figure 6.13 Loading in the machined corroded pipe test.

Figure 6.14 Pipe II with the circumferential groove machined corrosion.

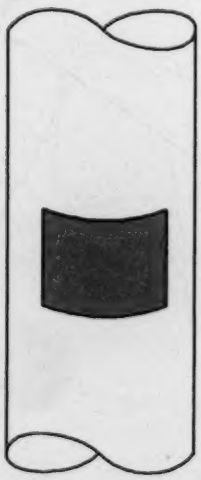

Figure 6.15 Pipe III with the square patch machined corrosion.

Figure 6.16 Finite element mesh for IB.

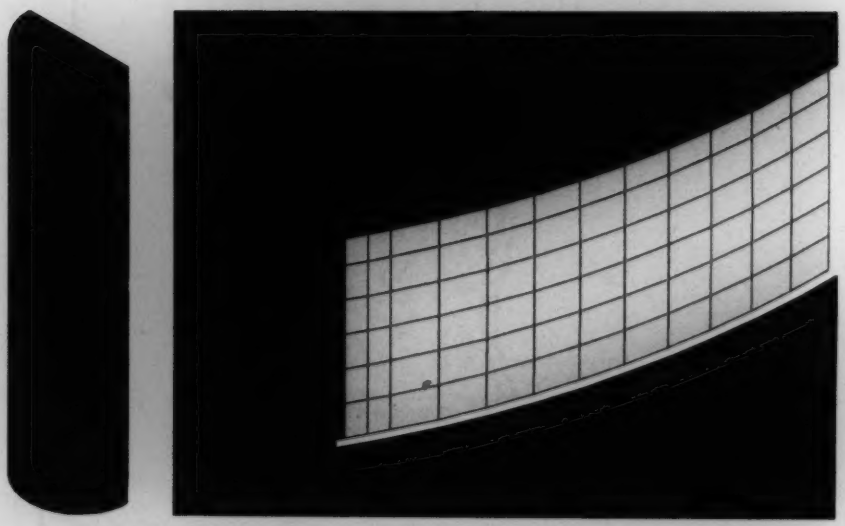

Figure 6.17 Finite element mesh for IIB and the close-up of the machined corrosion.

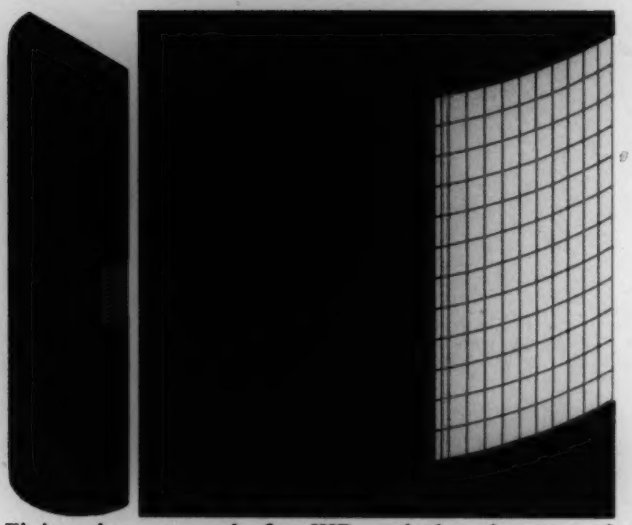

Figure 6.18 Finite element mesh for IIIB and the close-up of the machined corrosion.

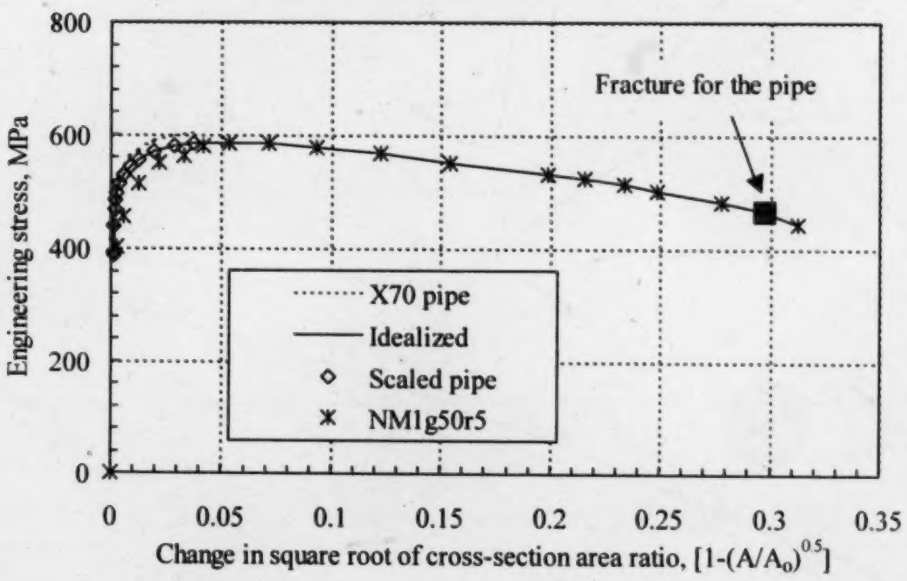

Figure 6.19 Idealized stress versus change in cross-section for the pipe tension material test.

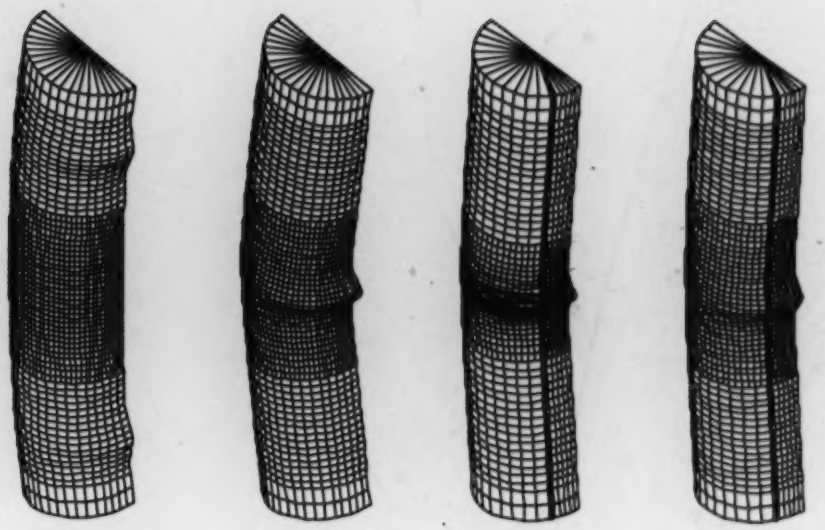

Figure 6.20 Predicted deformed shape.

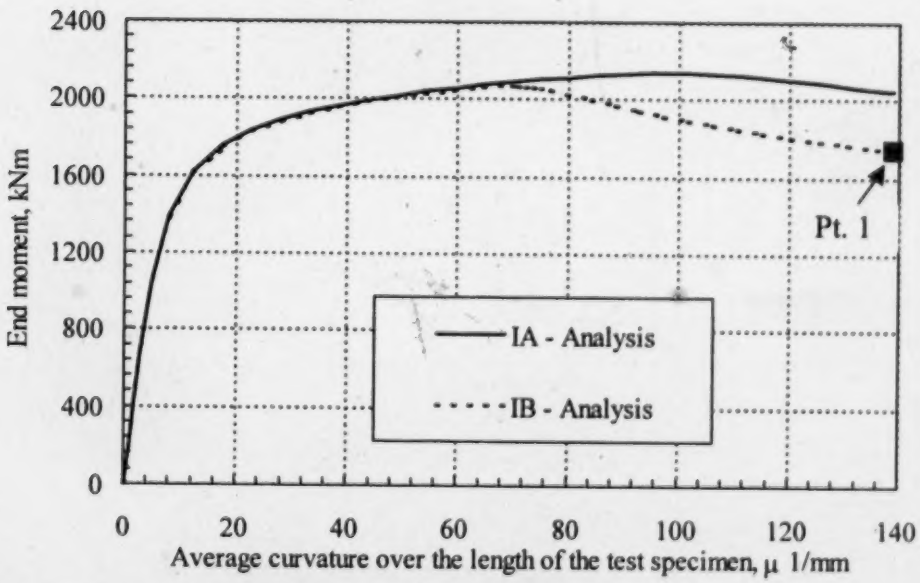

Figure 6.21 Predicted moment versus global curvature for pipe I.

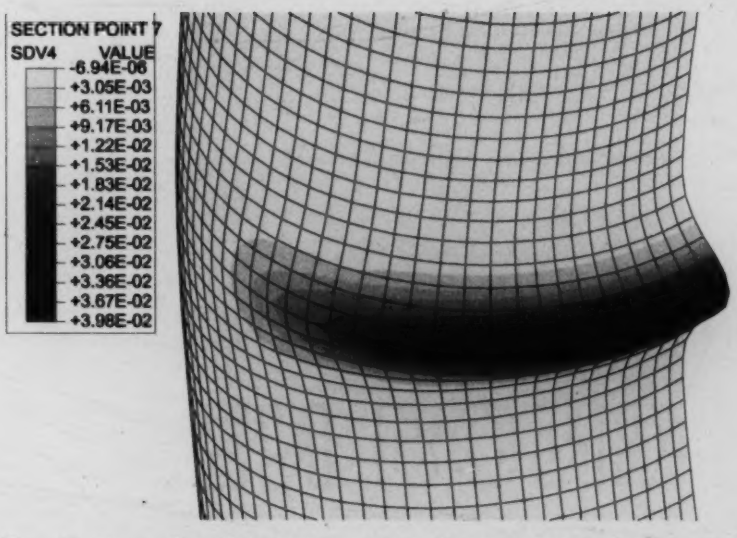

Figure 6.22 Contour plot of the outer surface damage state D for IB corresponding to the load point 1.

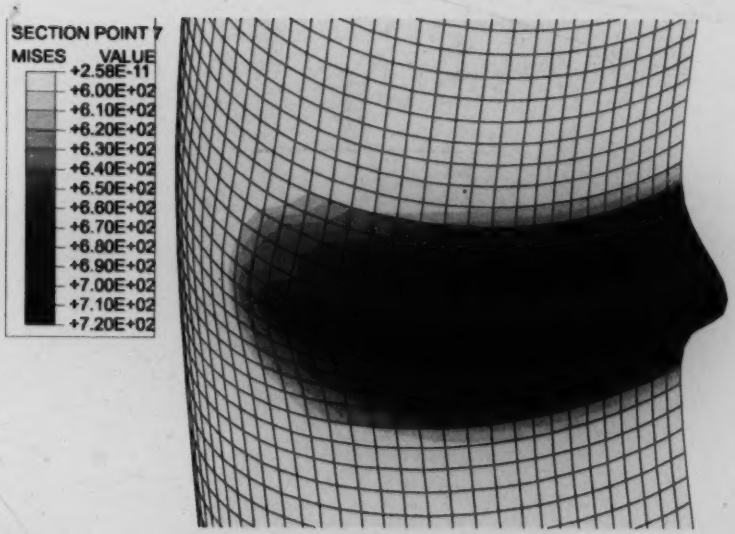

Figure 6.23 Contour plot of the outer surface von Misés stress (σ_{eq}) for IB corresponding to the load point 1.

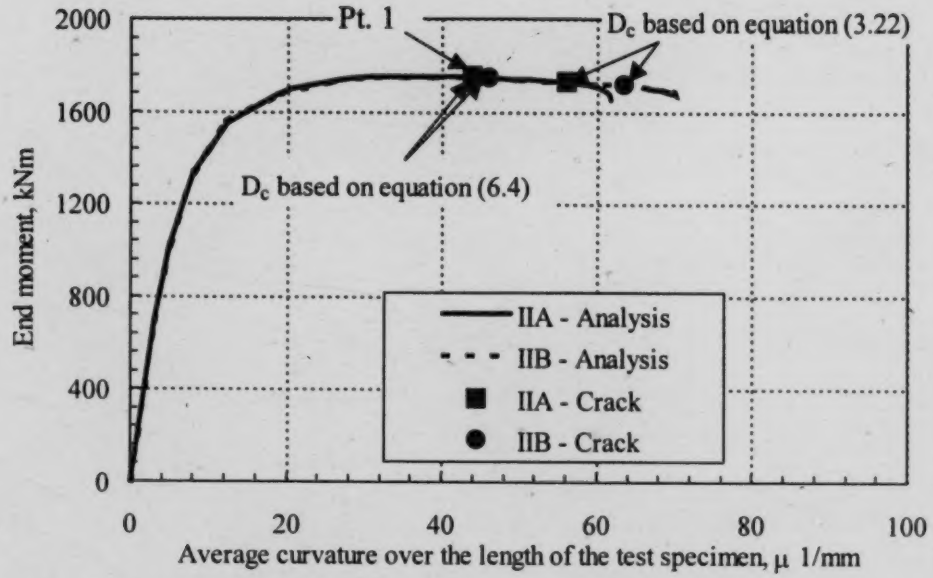

Figure 6.24 Predicted moment versus global curvature for pipe II.

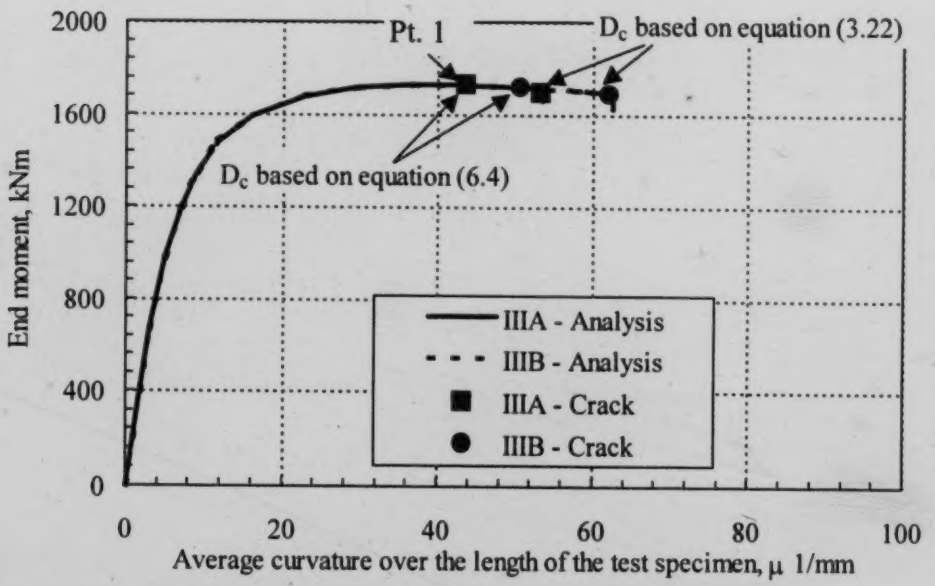

Figure 6.25 Predicted moment versus global curvature for pipe III.

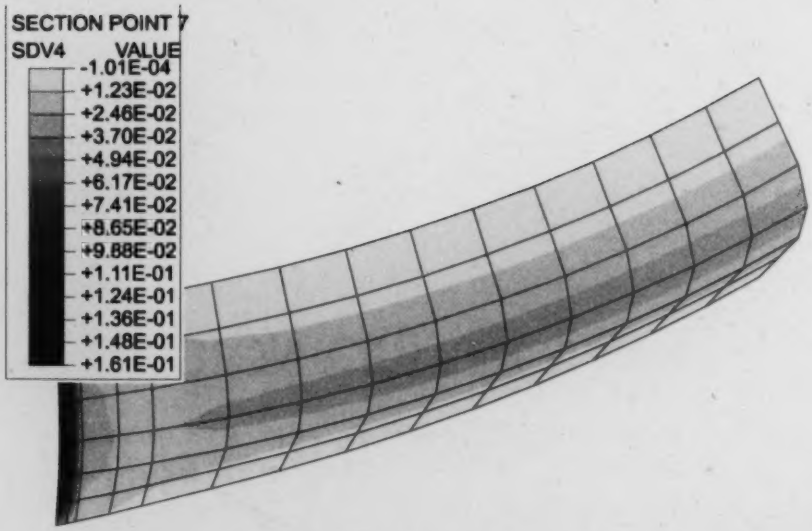

Figure 6.26 Contour plot of the outer surface damage state D at the machined corrosion for IIA corresponding to the loading stage where the critical damage limit D_c, calculated using (6.4), is first exceeded.

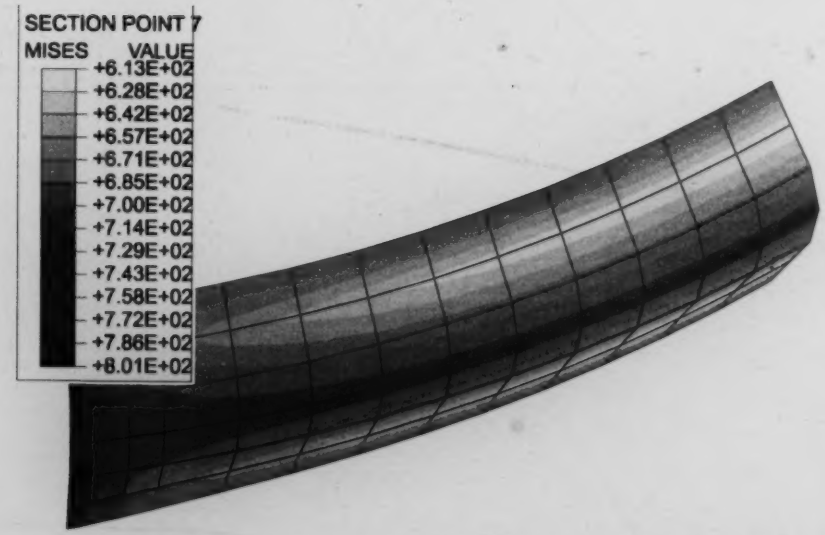

Figure 6.27 Contour plot of the outer surface von Misés stress (σ_{eq}) at the machined corrosion for IIA corresponding to the loading stage where the critical damage limit D_c, calculated using (6.4), is first exceeded.

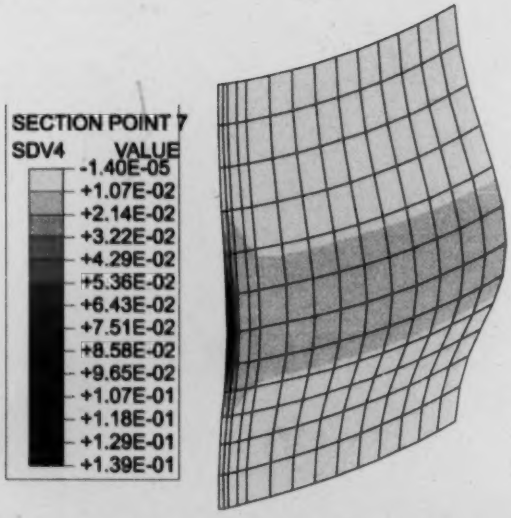

Figure 6.28 Contour plot of the outer surface damage state D at the machined corrosion for IIIA corresponding to the loading stage where the critical damage limit D_c, calculated using (6.4), is first exceeded.

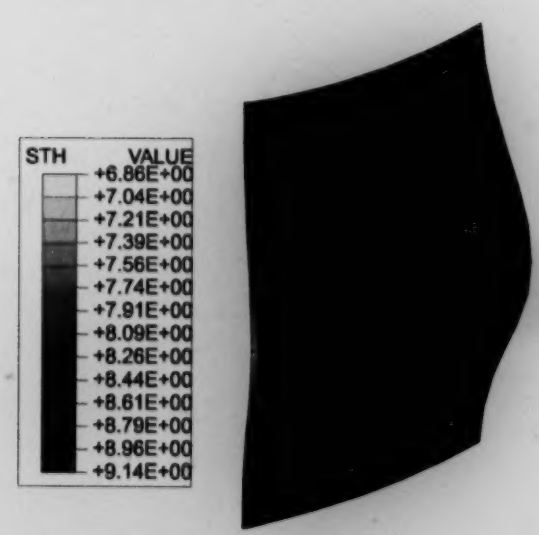

Figure 6.29 Contour plot of the shell thickness at the machined corrosion for IIIA corresponding to the loading stage where the critical damage limit D_c, calculated using (6.4), is first exceeded.

7 Summary, Conclusions and Recommendations

7.1 Summary

Recent developments in predicting brittle and ductile fracture of solids are reviewed in Chapter 2. Various approaches have been proposed to model ductile fracture based on the observed physical process. Parameters such as the critical damage state in a continuum damage mechanics model, the critical void volume fraction, the critical void growth rate, the absorbed energy till fracture or other parameters that are integrated over the plastic strain, are utilized in predicting fracture. However among those models reviewed, there is no simple constitutive model that takes into account the material dilation due to void growth. Furthermore, most of these constitutive models have not been extensively verified with test data.

A constitutive model is thus developed to predict the ductile fracture of steel for monotonic quasi-static loading. It is modified from the continuum damage model proposed by Lemaitre (1984, 1985), but unlike the model by Lemaitre, the new model incorporates material dilation due to void growth and the damage limit is assumed to vary inversely to the square of the hydrostatic tension stress. In the proposed model, damage is assumed to be isotropic and is a function of the state of stress and the plastic strain increment. Material dilation is assumed to vary with the state of damage. Fracture is assumed to occur when the damage limit is reached. In order to carry out the numerical analysis, the material model is implemented as a user-defined material subroutine in the commercial finite element program ABAQUS. Due to the considerable shape change that occurs before fracture, numerical analyses are performed using the updated Lagrangian formulation.

Round tension coupon tests were carried out to acquire experimental data for studying and validating the proposed material model. Sixteen coupons with three heat treatments, two diameters, various transition radii and gage lengths were used in order to obtain test data from specimens with different ductility and various levels of hydrostatic tension stress. All specimens were monotonically loaded with the exception of two specimens, which were unloaded and reloaded intermittently during the test. The test was carried out with regular stoppages for measuring the static readings. These test data are able to provide a good basis for studying the proposed constitutive model. The

ductility of the specimen decreases as the gage length or the transition radius or both are reduced.

After reviewing the test results, the load versus the cross-section dimension curve for a 50 mm gage length specimen is used in calibrating most of the properties and parameters because of its insensitivity to the geometric variation. Data from short gage length specimens are used in calibrating the parameter n, the exponent that governs the damage rate in (3.12), and data from all monotonically loaded specimens are used in calibrating the parameter D_o, the material constant for calculating the critical damage limit in (3.22). The damage initiation equivalent plastic strain $\varepsilon^p_{eq_c}$ is assumed to be zero in all the numerical simulations based on the results of the intermittent unloading and reloading tests, which indicate that damage has started fairly early.

Comparisons are made between analytical and measured results. A complete fracture of the coupon is assumed to occur once the damage limit is reached. An axisymmetric element is used in modeling the round coupon. Properties and parameters (except n and D_o) used in the numerical analyses for specimens in the same heat are calibrated from test results of just a single specimen. Comparisons are also made against results from models by Matic et al. (1987) and Lemaitre (1984, 1985).

To illustrate the application of the material model, numerical simulations are carried out for two practical cases: predicting the capacity and the failure of a slotted tubular steel structural connection and a corroded pipe. Existing test data for slotted tubular tension members are used in comparison. However, due to the significantly greater computing effort required in carrying out the numerical analysis using a solid element, slotted tubular tension members and machined corroded pipes are instead modeled with a shell element. However, a shell element cannot accurately represent regions where plates or shells intersect because it only considers in-plane normal stresses. Thus, a modified critical damage limit equation is used at the slotted end of the tubular tension member to account for this deficiency.

7.2 Conclusions

A constitutive material model is developed for the ductile fracture of steel based on the continuum damage model considering material dilation and hydrostatic tension stress during fracture. A number of significant conclusions have been drawn based on the experimental and numerical results:

1) Overall, the material model gives a good prediction of the load-deformation behaviour of the tension coupon specimens and the instant when fracture occurs. The predicted deformed shape also matches the actual shape at a similar stage of loading. Since the model does not attempt to capture the coalescence process, the numerical solution tends to under predict the ductility of a long gage length specimen at fracture and over predict the one for a short gage length specimen. However, the constitutive model is capable of capturing the overall trend of the ductility reduction associated with a higher hydrostatic tension stress as in the case of a shorter gage length or a smaller transition radius.

2) Test results show that the ductility and the load-deformation response of the tension coupon specimen are sensitive to variations in the geometry, especially if the gage length is short. Thus, an accurate measurement of the dimension of a short gage length specimen is required in order to predict the load-deformation response of the specimen properly.

3) Unlike the load-longitudinal deformation response, the study shows that the load versus the cross-section dimension relationship is insensitive to the geometric imperfection when the gage length is long. As a result, the load versus the cross-section dimension relationship should be measured in a tension coupon test in addition to the normal load-longitudinal deformation measurement. Properties and parameters used in the numerical analyses should be calibrated from a tension coupon with a sufficiently long gage length.

4) Properties and parameters (except n and D_o) used in the numerical analyses for specimens in the same heat can be calibrated from test results of just a single specimen. This implies that properties and parameters required for the numerical analyses can be obtained from a single standard ASTM tension material test with the exception of n and D_o. The value of n can be estimated using the graph in

Figure 5.68 using the cross-section area at fracture, and D_o may be calibrated using the measured diameter (d_f) at fracture. However, to be conservative, 105% or 110% of d_f may be considered as the fracture diameter since the material model tends to under predict the ductility of a long gage length tension coupon.

5) The difference between the direct measurement using a caliper and the value calculated from the photograph is found to be small. The result of this comparison indicates that digital photographs can serve as an adequate backup for some of the direct measurements.

6) The proposed model is able to predict the deformation and the instant fracture occurs better than models by Matic et al. (1987) and Lemaitre (1984, 1985).

7) From intermittent unloading and reloading tests, the apparent modulus of elasticity is found to start dropping at a very small strain. This finding indirectly agrees with the observation by Le Roy et al. (1981), and Cox and Low (1974) which indicated that void nucleation starts at a low strain. However, the numerical analysis is not able to accurately predict the drop in the apparent modulus of elasticity. The drop in the measured apparent elastic modulus is much faster than the predicted one. One reason may be the fact that the proposed model assumes the effective elastic modulus does not change with deformation, and any change in the apparent elastic modulus is caused by the nucleation and expansion of voids. But in actual fact, the effective elastic modulus may have decreased with deformation. The model may also under predict the damage in the specimen.

8) A specimen that has undergone a frequent unloading and reloading process has a higher peak stress and a lower ductility than a monotonically loaded specimen, although the difference is not big.

9) In the numerical simulations of slotted tubular tension members tests, the proposed model is able to give a good prediction of the load-deformation response, the location and the instant of fracture. However, with a shell element, the numerical analyses over predict the pipe wall thickness reduction rate. This is due to the fact that a shell element is unable to capture the stiffening effect in the necking process. As the pipe wall starts to neck, the increased hydrostatic tension stress that develops stiffens that part of pipe wall, therefore delaying the necking process.

7.3 Recommendations

1) The study has demonstrated that the proposed model works well for a monotonic type loading condition. However, this loading condition does not cover all applications where fracture is important. In order to predict fracture of steel structures under cyclic loading, kinematic hardening needs to be incorporated into the proposed model. In addition, more work is required to expand and study the model for other loading conditions such as fatigue loading.

2) Even though the test program provides sufficient data for studying the proposed model, more results from materials with a more diverse inherent ductility would be desirable. Additional test results would enable the proposed model to be studied over a greater range of ductility, and also furnish more data points for the graph in Figure 5.68. The graph in Figure 5.68 is used as a guide in the determination of the parameter n from a standard ASTM tension coupon test.

3) A shell element is used in the numerical simulation of slotted tubular tension members and machined corroded pipes tests due to limits on the size of the finite element problem that could be handled with the available computing facilities. Although good results are obtained using the shell element, it lacks the ability to capture the stiffening effect in the necking process. In the future, as faster computers become more affordable, analyses of this nature may be carried out with a 3D solid element to better represent the actual behaviour.

4) In the thesis, analyses were carried out without considering the propagation of cracks. The omission of crack propagation is not particularly important in a tension coupon test because the occurrence of local fracture is closely followed by the complete fracture of the specimen. But in other applications unlike a tension coupon, the occurrence of a first crack is not necessarily closely associated with an abrupt drop in the load carrying capacity or the loss of structural integrity, as in the case of the machined corroded pipe test. Thus, improving the current modeling or solution scheme to allow for the propagation of cracks would give a better prediction of the structural behaviour.

References

1. ABAQUS Version 5.7 1997. ABAQUS/Standard User's Manual: Volume 1, 2 and 3, Hibbitt, Karlsson & Sorensen Inc.
2. Anderson, T.L. (1991), "Fracture Mechanics: Foundamentals and Applications," CRC Press, pp. 793.
3. Andrianopoulos, N.P. and Theocaris, P.S. (1988), "LEFM Brittle and Ductile Fracture as Described by The T-Criterion", Engineering Fracture Mechanics, Vol. 30, pp. 5-12.
4. Bluhm, J.I. and Morrissey, R.J. (1965), "Fracture in Tensile Specimen", Proceedings of the First International Conference in Fracture, Sendai, Japan, pp. 1739-1780.
5. Bridgman, P.W. (1947), "Fracture and Hydrostatic Pressure," Fracturing of Metals, Twenty-Ninth National Metal Congress and Exposition, Chicago October 18-24, American Society for Metals, pp. 246-261.
6. Broek, D. (1986), "Elementary Engineering Fracture Mechanics," Fourth Revised Edition, Martinus Nijhoff Publishers, pp. 501.
7. Cheng, J.J.R., Kulak, G.L. and Khoo, H.A. (1998), "Strength of Slotted Tubular Tension Members", Canadian Journal of Civil Engineering, Vol. 25, No. 6, pp. 982-991.
8. Chow, C.L. and Wang, J. (1987a), "An Anisotropic Theory of Continuum Damage Mechanics for Ductile Fracture", Engineering Fracture Mechanics, Vol. 27, No. 5, pp. 547-558.
9. Chow, C.L. and Wang, J. (1987b), "An Anisotropic Theory of Elasticity for Continuum Damage Mechanics", International Journal of Fracture, Vol. 33, pp. 3-16.
10. Chow, C.L. and Wang, J. (1988), "A Finite Element Analysis of Continuum Damage Mechanics for Ductile Fracture", International Journal of Fracture, Vol. 38, pp. 83-102.
11. Cox, T.B. and Low, J.R. (1974), "An Investigation of the Plastic Fracture of AISI 4340 and 18 Nickel-200 Grade Maraging Steels", Metallurgical Transactions, Vol. 5, No. 4, pp. 237-252.

12. Czoboly, E. Havas, I. and Gillemot, F. (1980), "The Absorbed Specific Energy Till Fracture as a Measure of the Toughness of Metals", Proceedings of an International Symposium on Absorbed Specific Energy and/or Strain Energy Density Criterion, (Eds. by G.C. Sih, E. Czoboly and Gillemot, F.), Budapest, Hungary, Martinus Nijhoff Publishers, pp. 107-129.

13. DeGiorgi, V.G., Kirby III, G.C. and Jolles, M.I. (1989), "Prediction of Classical Fracture Initiation Toughness", Engineering Fracture Mechanics, Vol. 33, No. 5, pp. 773-785.

14. DelCol, P.R., Grondin, G.Y., Cheng, J.J.R. and Murray, D.W. (1998), "Behaviour of Large Diameter Line Pipe under Combined Loads", Structural Engineering Report No. 230, Dept. of Civil and Environmental Engineering, University of Alberta, April, 218 pages.

15. Gillemot, L.F. (1976), "Criterion of Crack Initiation and Spreading", Engineering Fracture Mechanics, Vol. 8, pp. 239-253.

16. Gurson, A.L. (1977a), "Continuum Theory of Ductile Rupture by Void Nucleation and Growth: Part I - Yield Criteria and Flow Rules for Porous Ductile Media", Journal of Engineering Materials and Technology, January, pp. 2-15.

17. Gurson, A.L. (1977b), "Porous Rigid-Plastic Materials Containing Rigid Inclusions - Yield Function, Plastic Potential, and Void Nucleation", Proceedings of the Fourth International Conference on Fracture, ICF4, Vol. 2A, pp. 357-364.

18. Griffith, A.A. (1921), "The Phenomena of Rupture and Flow in Solids," Philosophical Transactions of the Royal Society of London, Ser. A, vol. 221, pp. 163-197.

19. Hancock, J.W. and Mackenzie, A.C. (1976), "On the Mechanisms of Ductile Failure in High-Strength Steels Subjected to Multi-Axial Stress-States", Journal of the Mechanics and Physics of Solids, Vol. 24, pp. 147-169.

20. Hertzberg, R.W. (1989), "Deformation and Fracture Mechanics of Engineering Materials," Third Edition, John Wiley & Sons, pp. 680.

21. Hutchinson, J.W. (1968), "Singular Behaviour at the End of a Tensile Crack in a Hardening Material", Journal of the Mechanics and Physics of Solids, Vol. 16, pp. 13-31.

22. Irwin, G. (1947), "Fracture Dynamics," Fracturing of Metals, Twenty-Ninth National Metal Congress and Exposition, Chicago October 18-24, American Society for Metals, pp. 147-166.

23. Jayatilaka, A.S., Jenkins, I.J. and Prasad, S.V. (1977), "Determination of Crack Growth in Mixed Mode Loading System", Fracture, Vol. 3, ICF4, Waterloo, pp. 15-23.

24. Koo, J.M. and Choy, Y.S. (1991), "A New Mixed Mode Fracture Criterion: Maximum Tangential Strain Energy Density Criterion", Engineering Fracture Mechanics, Vol. 39, pp. 443-449.

25. Lemaitre, J. (1984), "How to Use Damage Mechanics", Nuclear Engineering and Design, Vol. 80, pp. 233-245.

26. Lemaitre, J. (1985), "A Continuous Damage Mechanics Model for Ductile Fracture", Journal of Engineering Materials and Technology, Vol. 107, pp. 83-89.

27. Lemaitre, J. (1992), "A Course on Damage Mechanics", Springer-Verlag.

28. Le Roy, G., Embury, J.D., Edward, G. and Ashby, M.F. (1981), "A Model of Ductile Fracture Based on the Nucleation and Growth of Voids", Acta Metallurgica, Vol. 29, pp. 1509-1522.

29. Marini, B., Mudry, F. and Pinuea, A. (1985), "Ductile Rupture of A508 Steel under Nonradial Loading", Engineering Fracture Mechanics, Vol. 22, No. 3, pp. 375-386.

30. Matic, P., Kirby III, G.C. and Jolles, M.I. (1987), "The relationship of the Tensile Specimen Size and Geometry Effects to Unique Constitutive Parameters for Ductile Materials", NRL Memorandum Report 5936, Mechanics of Materials Branch, Material Science and Technology Division.

31. McClintock, F.A. (1968), "A Criterion for Ductile Fracture by the Growth of Holes", Journal of Applied Mechanics, pp. 363-371.

32. Mohareb, M.E., Elwi, A.E., Kulak, G.L. and Murray, D.W. (1994), "Deformation Behaviour of Line Pipe", Structural Engineering Report No. 202, Dept. of Civil and Environmental Engineering, University of Alberta, April, 194 pages.

33. Norris, D., Reaugh, J.E., Moran, B. and Quiñones, D.F. (1978), "A Plastic-Strain, Mean-Stress Criterion for Ductile Fracture", Journal of Engineering Materials and Technology, Vol. 100, pp. 279-286.

34. Rice, J.R. (1968), "A Path Independent Integral and the Approximate Analysis and Strain Concentration by Notches and Cracks,", Journal of Applied Mechanics, pp. 379-386.

35. Rice, J.R. and Rosengren, G.F. (1968), "Plane Strain Deformation Near a Crack Tip in a Power-Law Hardening Material", Journal of the Mechanics and Physics of Solids, Vol. 16, pp. 1-12.

36. Rice, J.R. and Tracey, D.M. (1969), "On the Ductile Enlargement of Voids in Triaxial Stress Fields", Journal of the Mechanics and Physics of Solids, Vol. 17, pp. 201-217.

37. Sih, G.C. (1973a), "Introductory Chapter: A Special Theory of Crack Propagation", Mechanics of Fracture Vol. 1 - Methods of Analysis and Solutions of Crack Problems, (Ed. G.C. Sih), Noordhoff International Publishing, Leyden, The Netherlands, pp. XXI-XLV.

38. Sih, G.C. (1973b), "Some Basic Problems in Fracture Mechanics and New Concepts", Engineering Fracture Mechanics, Vol. 5, pp. 365-377.

39. Sih, G.C. and Li, C.T. (1993), "Subcritical Crack Growth in Elastic-Plastic Material with Overshoot: Part I-Analytical Modeling", Theoretical and Applied Fracture Mechanics, Vol. 18, pp. 115-129.

40. Sih, G.C. and Madenci, E. (1983), "Crack Growth Resistance Characterized by the Strain Energy Density Function", Engineering Fracture Mechanics, Vol.18, No. 6, pp. 1159-1171.

41. Shi, Y.W., Barnby, J.T. and Nadkarni, A.S. (1991), "Void Growth at Ductile Crack Initiation of a Structural Steel", Engineering Fracture Mechanics, Vol. 39, No. 1, pp. 37-44.

42. Sun, D.-Z., Siegele, D., Voss, B. and Schmitt, W. (1989), "Application of Local Damage Models to the Numerical Analysis of Ductile Rupture", Fatigue and Fracture of Engineering Materials and Structures, Vol. 12, No. 3, pp. 201-212.

43. Tai, W.H. and Yang, B.X. (1987), "A New Damage Mechanics Criterion for Ductile Fracture", Engineering Fracture Mechanics, Vol. 27, No. 4, pp. 371-378.

44. Theocaris, P.S. and Andrianopoulos, N.P. (1982b), "The T-Criterion Applied to Ductile Fracture", International Journal of Fracture, Vol. 20, pp. R125-R130.

45. Theocaris, P.S. and Philippidis, T.P. (1987), "The T-Criterion for Ductile Fractures in HRR Plastic Singularity Fields", International Journal of Fracture, Vol. 35, pp. 21-37.

46. Tvergaard, V. (1982), "Ductile Fracture by Cavity Nucleation between Larger Voids", Journal of the Mechanics and Physics of Solids, Vol. 30, No. 4, pp. 265-286.

47. Tvergaard, V. and Needlemen, A. (1984), "Analysis of the Cup-Cone Fracture in a Round Tensile Bar", Acta Metallurgica, Vol. 32, No. 1, pp. 157-169.

48. Wang, T.-J. (1992a), "Unified CDM Model and Local Criterion for Ductile Fracture-I. Unified CDM Model for Ductile Fracture", Engineering Fracture Mechanics, Vol. 42, No. 1, pp. 177-183.

49. Wang, T.-J. (1992b), "Unified CDM Model and Local Criterion for Ductile Fracture-II Ductile Fracture Local Criterion Based on CDM Model", Engineering Fracture Mechanics, Vol. 42, No. 1, pp. 185-193.

50. Yehia, N.A.B. (1991), "Distortional Strain Energy Density Criterion: the Y-Criterion", Engineering Fracture Mechanics, Vol. 39, No. 3, pp. 477-485.

Appendix A - Mesh Study

The mesh study is carried out by simulating AS1g50r5 numerically using parameters calibrated in Chapter 5. Preliminary numerical analyses show that all specimens neck and fail at the mid-length of the specimen, and fracture is initiated from the centre of the cross-section. Thus, the finite element mesh at the mid-length is refined in order to give a more accurate modeling. Figures A.1 and A.2 show the two refined finite element mesh schemes used in the mesh study. The size of the element at the refined region for scheme-2 is half that of scheme-1. Scheme-2 is the one used in Chapter 5. Stresses, strains and the state of damage at the critical location (the mid-length along the axis) of AS1g50r5 are projected from values at the integration points. Figures A.3 and A.4 show that the stress versus radial deformation and the damage versus radial deformation curves for both schemes are almost identical. Thus, no further refinement to scheme-2 is required.

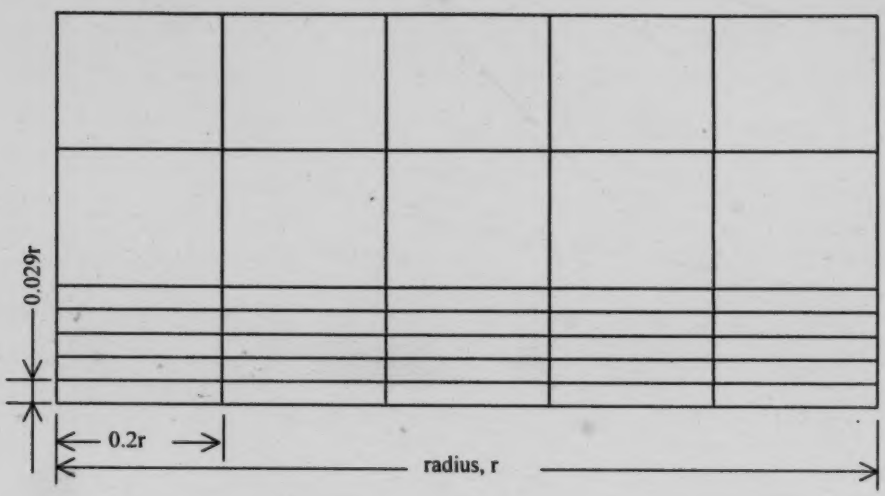

Figure A.1 Finite element mesh scheme-1 at the mid-length of AS1g50r5.

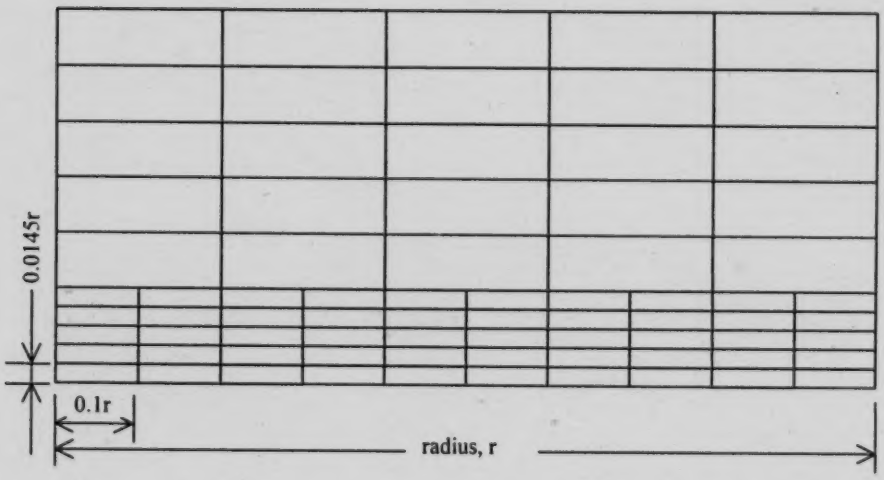

Figure A.2 Finite element mesh scheme-2 at the mid-length of AS1g50r5.

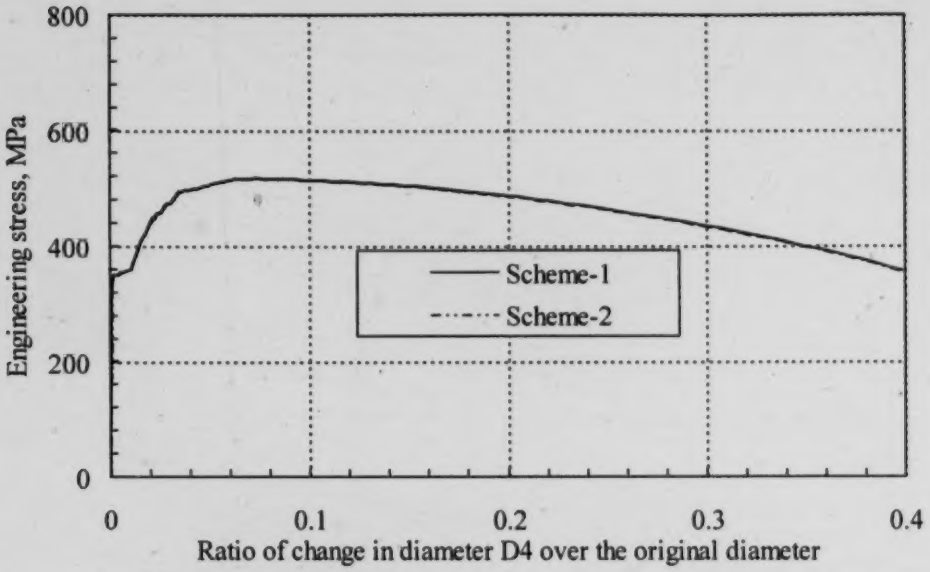

Figure A.3 Analytical stress versus change in diameter D4 for AS1g50r5 with different mesh schemes.

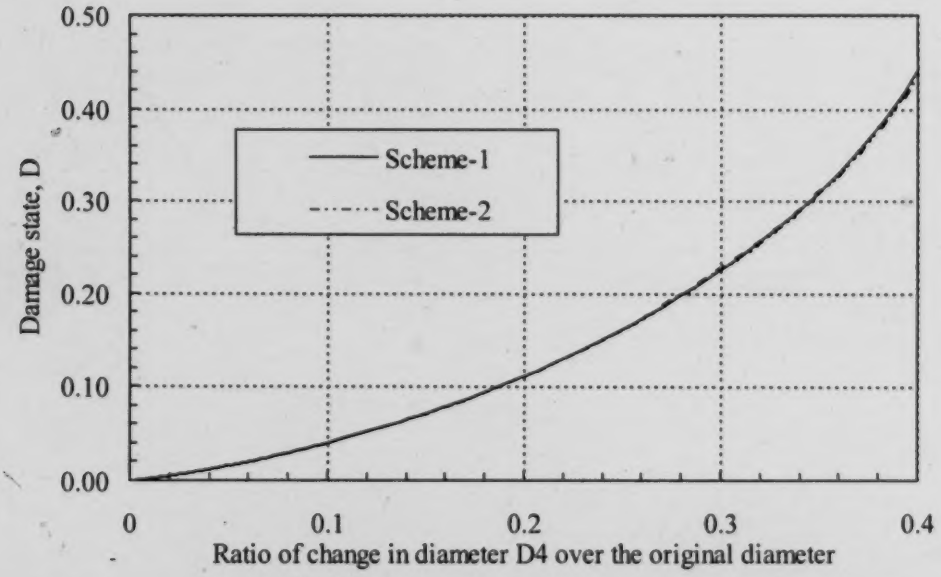

Figure A.4 Analytical damage state versus change in diameter D4 for different mesh schemes at the mid-length along the axis of AS1g50r5.

Appendix B - Measured Stress versus Extensometer Strain Curves

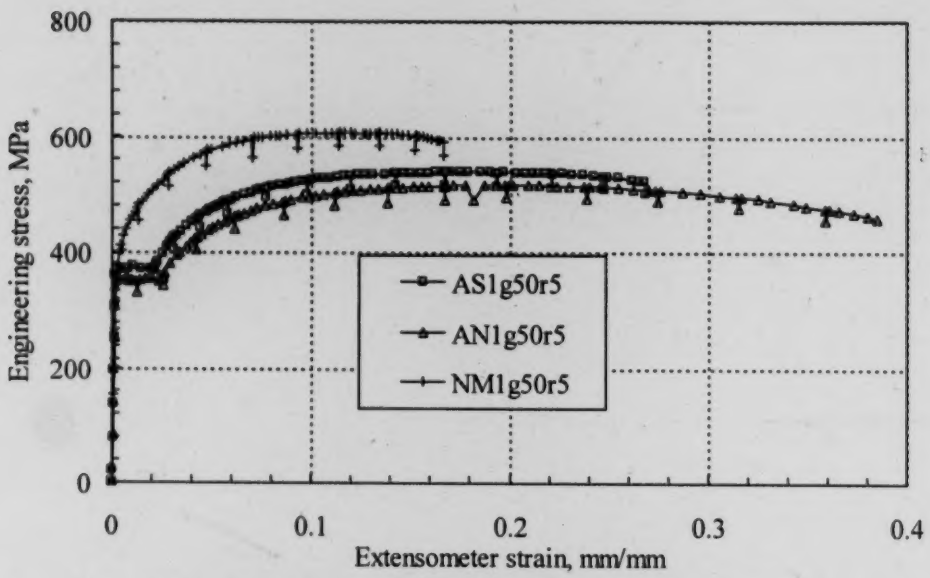

Figure B.1 Measured stress versus extensometer strain for monotonically loaded g50r5 specimens.